ABSTRACT

Title of dissertation: TIGHT-BINDING SIMULATIONS OF RANDOM ALLOY AND STRONG SPIN-ORBIT EFFECTS IN INDIUM-ARSENIDE/GALLIUM-BISIMIDE-ARSENIDE QUANTUM DOT MOLECULES

Arthur Lin
Doctor of Philosophy, 2023

Dissertation directed by: Professor Garnett W. Bryant
Department of Physics

Self-assembled InAs quantum dots (QDs), which have long hole-spin coherence times and are amenable to optical control schemes, have long been explored as building blocks for qubit architectures. One such design consists of vertically stacking two QDs to create a quantum dot molecule (QDM). The two dots can be resonantly tuned to form "molecule-like" coupled hole states with the hybridization of hole states otherwise localized in each respective dot. Furthermore, spin-mixing of the hybridized states in dots offset along their stacking direction enables qubit rotation to be driven optically, allowing for an all-optical qubit control scheme. Increasing the magnitude of this spin-mixing is important for optical quantum control protocols. We introduce the incorporation of dilute $GaBi_xAs_{1-x}$ alloys in the barrier region between the two dots, as GaBiAs is expected to provide an increase in spin-mixing of the molecular states over GaAs.

Using an atomistic tight-binding model, we compute the properties of $GaBi_xAs_{1-x}$ and the modification of hole states that arise when the alloy is used in the barrier of an InAs QDM. We show that an atomistic treatment is necessary to correctly capture non-traditional alloy effects of GaBiAs. Additionally, an atomistic model allows for the study of configurational variances and clustering effects of the alloy. We find that in InAs QDMs with a GaBiAs inter-dot barrier, hole states are well confined to the dots up to an alloy concentration of 7%. By independently studying the alloy-induced strain and electronic scattering off Bi and As orbitals, we conclude that an initial increase in QDM hole state energy at low Bi concentration is caused by the alloy-induced strain. Additionally, a comparison between the fully alloyed barrier and a partially alloyed barrier shows that fully alloying the barrier applies an asymmetric strain between the top and bottom dot.

By lowering the energetic barrier between the two dots, GaBiAs is able to promote the tunnel coupling of hole states in QDMs. We obtain a three fold increase of hole tunnel coupling strength in the presence of a 7% alloy. Additionally, we show how an asymmetric strain between the two dots caused by the alloy results in a shift in the field strength needed to bring the dots to resonance. We explore different geometries of QDMs to optimize the tunnel coupling enhancement the alloy can provide, as well as present evidence that the change in tunnel coupling may affect the heavy-hole and light-hole components of the ground state in a QDM.

The strong spin-orbit coupling strength of GaBiAs allows for the enhancement of spin-mixing in QDMs. A strong magnetic field can be applied directly in the TB Hamiltonian. In order to fit the TB results to a simple phenomenological Hamiltonian, we found it necessary to include second order magnetic field terms in the phenomenological Hamiltonian as a diamagnetic correction to the hole state energies. Fitting to the corrected phenomenological model, we obtain a three-fold enhancement for the

spin-mixing strength of offset dots at 7% Bi. Additionally, at higher alloy concentrations, a combination of enhanced spin-mixing and increase resonance change in g-factor results in intra-dot spin-mixing between Zeeman split states of the lower energy dot. A perturbative analysis of the magnetic field shows that both the spin-mixing and resonance g-factor change are effects of the Peierls contribution, or the component of the magnetic field applied to the effective spatial angular momentum of the wavefunction. When spin-orbit coupling is removed from the system, there is no longer a preferred alignment between the spin of the system and the Peierls effective angular momentum, thus removing any magnetic field effects of the Peierls contribution.

The analysis of spin-orbit effects can be extended to single dots with in-plane magnetic and electric fields. This thesis concludes with some preliminary results utilizing electric fields, in conjunction with spin-locking effects provided by spin-orbit coupling, to manipulate the spin polarization in single dots. TB calculations with a magnetic field are performed to show the preferred alignment of the effective angular momentum, given by the geometry of the dot, also spatially locks the spin-polarization of hole states. An electric field can then be applied to bias the charge density to either side of the dot, using the spatial texture of the spin to obtain a spin polarized in z while both the magnetic and electric field is in the xy-plane. The same perturbative analysis with the QDMs can be applied to show sufficient spin-orbit coupling is needed to generate such an effect. We propose the utilization of spin texture and electric fields as a novel method for rotating the spin in QDs.

TIGHT-BINDING SIMULATIONS OF RANDOM ALLOY AND STRONG SPIN-ORBIT EFFECTS IN INDIUM-ARSENIDE/GALLIUM-BISIMIDE-ARSENIDE QUANTUM DOT MOLECULES

by

Arthur Lin

Dissertation submitted to the Faculty of the Graduate School of the
University of Maryland, College Park in partial fulfillment
of the requirements for the degree of
Doctor of Philosophy
2023

Advisory Committee:
Professor Jay Deep Sau, Chair
Professor Garnett W. Bryant, Advisor
Professor Andrew M. Childs
Professor Matthew F. Doty
Professor Emeritus Theodore L. Einstein
Assistant Professor Michael Gullans

Preface

Much of the work presented in this thesis shares similarity with material that has been or is currently in the process of being published. Chapters 3 and 4 reuses content published in Physical Review B **99**, 075308 (2019). Chapter 5 includes material from a paper that is currently under review with Physical Review B, a preprint of which can be found at arXiv:2309.10115.

From February 2018 to April 2019, I mentored an undergraduate student, Jack Carlton, through the Department of Physics at the University of Maryland, College Park. We investigated the effects of Bi distribution in GaBiAs alloys. The work he performed under my supervision is compiled in Appendix A.

Acknowledgments

There is an overwhelming gratitude that I have for all who have supported me during my graduate career. To the many people I have known, from folks who have been with me since before arriving at the University of Maryland to those providing encouraging words at the closing hour, thank you.

I would like to thank my advisor, Dr. Garnett Bryant. Your support for me has been insurmountable. To think, all time and resources you were willing to spend guiding me through my studies. Through you, I feel very privileged to have worked at the National Institute of Standards and Technology for my graduate studies.

Many thanks to my labmates, Emily Townsend, Maicol Ochoa, Keyi Liu, and Yan Li. All our discussions, scheduled or spontaneous, scientific or otherwise, has always been eye-opening conversations. Particular thanks to Emily, without whose keen eye, I'm sure my writings would be even more typographically error-prone. I would also like to acknowledge Prof. Doty. Although our meetings few and brief, your insights into the project has always been instrumental.

I can not understate the resource support provided by NIST and the National Science Foundation (NSF). Having an office at NIST, and the effectively unlimited computational resources provided, is a luxury for any graduate student. This project was also was partially supported by the NSF Grant No. DMR-1505628 and partially supported by NSF through the University of Delaware Materials Research Science and Engineering Center, DMR-2011824.

In my final years of study, working outreach for Emily Mercurio at the NSF Quantum Leap Challenge Institute for Robust Quantum Simulation was a well enjoyed

opportunity. It was a wonderful experience that perfectly complemented and capped off my time in graduate school.

To the housemates from Cool Sping Road to Radcliffe Drive, Wrick, Elizabeth, Liz, Trisin, and Wonseok, may we look back at our Maryland days fondly.

Finally, most importantly, to my family, particularly to my mother and father, who have always been the most supportive in my scientific endeavors, for your unwavering faith in me will I always be grateful.

To everyone,

thanks y'all,

Arthur

Table of Contents

List of Tables

List of Figures

List of Symbols and Abbreviations

BAC	band anti-crossing.
CBE	conduction band edge.
QD	quantum dot.
QDM	quantum dot molecule.
SO	spin-orbit.
TB	tight-binding.
VBE	valence band edge.
VBO	valence band offset (for the tight-binding model).
VCA	virtual crystal approximation.
VFF	valence force field.
a	lattice constant.
Å	angstrom (unit).
$\vec{B}$	magnetic field.
e	elementary charge.
$\vec{F}$	electric field.
$\hbar$	reduced Planck's constant.
X/$X^{\pm}$	exciton state/positively or negatively charged trion state.
Γ	Brillouin zone center.
μ_B	Bohr magnaton.
χ	second order parameter for magnetic splitting, diamagnetic parameter.

Chapter 1: Introduction

Direct bandgap quantum dots (QDs) have long been studied for their potential use in quantum computing architectures [4, 34, 41]. The deeper confining potential of self-assembled QDs allows for operations at higher temperatures compared to competing architectures such as gate defined dots or silicon dopants [34]. The combination of deep confining potentials and the opportunity to tune optical emission energies with QD size make III-V self-assembled QDs a particularly strong candidate for photonic quantum technologies [9]. Indeed, epitaxially-grown self-assembled InAs QDs in GaAs have the best photonic performance of all currently available quantum emitters, with near-perfect radiative quantum efficiency, extremely high emission fraction into the zero-phonon line, and excellent coherence [3, 13, 48, 50]. Moreover, numerous experiments have already used InAs QDs to demonstrate quantum functionality such as entanglement generation or teleportation [14, 23, 51].

Qubits can be created when an InAs QD is charged with a single electron or hole whose up and down spin projections define the logical basis states of the qubit [21, 28]. Such spin qubits can be controlled through the optical formation of trions, which are three-particle complexes consisting of an optically-generated exciton coupled to the additional resident charge. Optical selection rules for the trion transitions provide the means by which photons ("flying" qubits) initialize, manipulate, and readout the projection of the resident spin in order to implement quantum information functions [21]. In this approach, the qubit lifetime is limited by the spin lifetime. Nuclear

spins limit the electron spin coherence times [30, 31, 40]. In contrast, holes, which have weaker hyperfine interaction with the nuclei, can achieve spin coherence times that are an order of magnitude longer than that of electrons [20, 52] and may approach one second under certain conditions [24]. An additional benefit of hole states is the presence of spin-orbit (SO) interactions that allow for control schemes not available with electrons [2, 12, 32, 58].

Quantum Dot Molecules (QDMs) can be created when two QDs dots are stacked along the crystal growth axis and separated by a barrier thin enough to allow tunneling to create delocalized states with molecular orbital symmetry [17, 28]. In such QDMs, an electrical bias can be used to tune the states of the two QDs in and out of resonance with one another, controlling the formation of the molecular states [8, 16–18, 33, 38, 42, 49]. For QDMs in which holes tunnel between the two QDs, important new effects can emerge in the presence of both a) spin-orbit coupling and b) symmetry breaking that arises from a lateral offset between the QDs that comprise the QDM. The interaction of spin-orbit coupling and symmetry breaking leads to delocalized molecular hole states composed of intra-dot states with opposite hole spin character in each dot [16]. This “hole spin mixing" provides a tool for addressing a significant challenge for optically-controlled quantum information processing with InAs QDs.

One potential shortcoming of self-assembled dots is the inevitable structural inhomogeneity of the array of QDs used in a qubit architecture. Tuning many QDs to a fixed laser frequency or photonic cavity mode is a practical challenge. This issue can be overcome by the use of vertically stacked QDMs, in which pairs of InAs QDs separated by a GaAs tunnel barrier are stacked along the growth axis, nearly aligned. When the QDs are closely spaced, electric fields from a diode structure can be used to tune the hole states from the pair of QDs in and out of resonance, controlling the coupling strength between the dots and forming states with molecular orbital

symmetry [8, 16–18, 33, 38, 42, 49]. In this approach, the hole spin in the larger dot (typically the top dot), provides the spin-up and spin-down hole spin states that serve as the binary qubit basis. The QDM is tuned well away from resonance so that these two states have well-defined spin and are strongly localized to the top dot. Indirect optical transitions, ones that drive the hole states (h^+) to specially engineered charged trion states (X^+), are used to provide all-optical initialization, manipulation, and readout of the hole spin qubit. The particular X^+ states are driven by indirect transitions because the electron is in the top dot but the second hole is in a molecular state spread between the two dots. The electric field provided by the first hole serves to put the optically excited hole into a molecular state in resonance between the two dots. Indirect optical transitions have much larger Stark shifts than direct transitions and thus have a much larger tuning range.

In single InAs QDs, it is not possible to optically drive a coherent rotation between the up and down spin projections (qubit basis states) without applying an in-plane magnetic field (e.g. a magnetic field in the x-direction if the spin basis are in z). However, the application of an in-plane magnetic field also introduces precession between the two qubit basis states, which prevents non-destructive readout. The existence of hole spin mixing in QDMs provides a solution to this problem. Specifically, with the spin projection of a hole in one of the QDs serving as the qubit basis, coherent rotations between these two basis states can be achieved via a Λ-transition that couples both spin basis states to a single delocalized molecular-like trion state. Importantly, such a trion state has allowed optical transitions to both qubit basis states because of hole spin mixing. Thus the presence of hole spin mixing makes it possible to initialize, manipulate, and readout hole-spin qubit states in QDMs without a in-plane magnetic field [21].

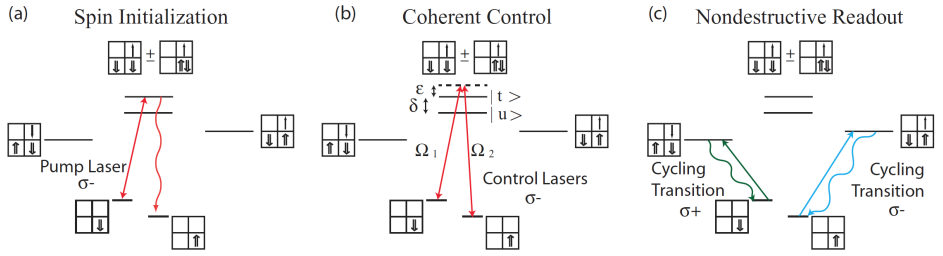

Figure 1.1: Proposed strategy for (a) spin initialization, (b) manipulation, and (c) readout using optical transitions of QDMs. Top/bottom rows indicate the spin projections of electrons/holes in the top (right column) and bottom (left column) QDs. (Excerpt from Economou *et al.*, Ref. [21])

The proposed strategies for the initialization, manipulation, and readout are shown in Fig. 1.1. Readout involves indirect resonant transitions between the hole spin and a trion state that preserve spin. The readout is nondestructive because no in-plane magnetic field, which would lead to spin-precession, is used in any of the qubit operations. Spin initialization and manipulation both depend on the molecular hole state being spin mixed by the tunnel coupling. The existence and origin of this hole state spin-mixing for molecular hole states has been established and explored [16, 44, 46]. Spin initialization occurs via optical shelving, with a resonant, indirect, optical transition taking one hole spin to a X^+ state which, because of the spin-mixing of the hole state, can then decay back to both spin states of the hole. The spin becomes initialized to the lower energy state after multiple transitions. Coherent spin manipulation is driven by two nonresonant, indirect optical Raman transitions which couple the two spin states of the qubit to the spin-mixed trion states. Increased spin mixing leads to faster spin initialization and more effective coherent control.

The magnitude of hole spin mixing is critically important for quantum device operation [21, 55]. The strength of the spin-mixing is determined by the alignment of the two dots. When the two dots are perfectly aligned, there is no spin mixing. However, the dots are typically offset in structures grown by molecular beam epitaxy. When

this is the case, rotational symmetry is broken (i.e., a lateral lever arm exists), the states acquire angular momentum, and the induced spin-orbit coupling leads to spin mixing [11, 16, 19, 39, 44, 46]. While hole spin mixing increases with the lateral offset between the two QDs, this offset is extremely difficult to control during growth. A lateral electric field, with a gradient that is asymmetric between the two dots in the QDM, can mimic the effects of a lateral offset to enhance hole spin mixing [39], but the electrodes that would create such a field are extremely difficult to incorporate into photonic devices. We are evaluating the opportunity to enhance hole spin mixing in QDMs by replacing the GaAs inter-dot barrier with a $GaBi_xAs_{1-x}$ alloy, without the need for a complicated electric field structure. The incorporation of Bi is expected to both lower the valence band edge (VBE) and increase spin-orbit interactions because Bi is heavier than As and has a strong spin-orbit coupling.

Recently, random alloy GaBiAs has generated substantial interest [1, 5–7, 15, 27, 53, 54, 59, 60]. The addition of dilute amounts of Bi to GaAs allows the valence band to be tuned, through band anticrossing (BAC) effects, to raise the valence-band edge (VBE) while minimally affecting the conduction band [54, 60]. Incorporating $GaBi_xAs_{1-x}$ into the region separating the two dots of a QDM lowers the interdot barrier for holes and enhances hole tunneling, while preserving the electron band structure. Additionally, literature suggests that GaBiAs has much stronger intrinsic spin-orbital (SO) interactions compared to GaAs because Bi is a heavier atom [7, 54, 60], which could also enhance the hole spin-mixing in QDMs.

In order to study the effects of a $GaBi_xAs_{1-x}$ alloy barrier in a QDM system, we first analyze the band structure and random alloy model for bulk GaBiAs using a the tight-binding (TB) model. Chapter 3 shows that, due to the unique BAC nature of $GaBi_xAs_{1-x}$, a virtual crystal approximation (VCA) is insufficient in describing the valence band of $GaBi_xAs_{1-x}$. A fully atomistic approach not only captures the

BAC effect, but also allows us to study variations created by different random realization of the alloy distribution. Unless otherwise noted, Bi placement in the GaBiAs alloy is determined with a pseudo-random number generator, resulting in what we deem as a random alloy distribution. Later chapters will note the use of weighted distributions of Bi resulting in a clustered distribution, and periodic placement of Bi resulting in a ordered distribution. An undergraduate student I mentored has performed additional studies on the distribution of Bi in bulk GaBiAs; these results will be included in Appendix A.

The main priority of the thesis is to discuss the effects of GaBiAs barriers in InAs QDs. Chapter 4 discusses the change in energy levels of the dot with the introduction of a GaBiAs barrier. We find that, for a fully alloyed inter-dot barrier, the hole states stay well confined to the dot up to a Bi concentration of 7%. We also show that the combined strain and orbital effects of the alloy are much greater than the individual effects applied in isolation. Additionally, a comparison between the fully alloyed barrier and a partially alloyed barrier shows that fully alloying the barrier applies an asymmetric strain between the top and bottom dot. Chapter 5 incorporates the application of a transverse electric field to show the alloy enhancement to the spin-preserving tunnel resonance between the two dots of the QDM. A three-fold enhancement is obtained at an alloy concentration of 7%. In the case of a fully alloyed barrier, the asymmetric alloy strain applied the top and bottom dots results in a shift in the field strength needed to bring the dots to resonance. Finally, in Chapter 6, we show the alloy enhancement to spin-mixing in QDMs. In order to fit the TB results to a simple phenomenological Hamiltonian, we found it necessary to include second order magnetic field terms in the phenomenological Hamiltonian as a diamagnetic correction to the hole state energies. Fitting to the corrected phenomenological model, we obtain a three-fold enhancement for the spin-mixing strength of offset dots at 7% Bi. Small

amounts of spin-mixing can also be introduced to aligned dots with the incorporation of the alloyed barrier. Furthermore, at higher alloy concentrations, a combination of enhanced spin-mixing and increase resonance change in g-factor results in intra-dot spin-mixing between Zeeman split states of the lower energy dot. A perturbative analysis of the magnetic field shows that both the spin-mixing and resonance g-factor change are effects of the Peierls contribution, or the component of the magnetic field applied to the effective spatial angular momentum of the wavefunction. When spin-orbit coupling is removed from the system, there is no longer a preferred alignment between the spin of the system and the Peierls effective angular momentum, thus removing any magnetic field effects of the Peierls contribution.

In addition to QDM systems, the analysis of SO effects can be extended to single dots with in-plane (perpendicular to the short axis of the dot) magnetic and electric fields. This thesis concludes with some preliminary results utilizing electric fields, in conjunction with spin-locking effects provided by SO coupling, to manipulate the spin polarization in single dots. TB calculations with a magnetic field are performed to show the preferred alignment of the effective angular momentum, given by the geometry of the dot, also locks the spin-polarization of hole states. The result is a spin that is not able to freely align with the magnetic field, creating a spatially textured spin distribution, with opposite out-of-plane spin-polarizations on either corner of the dot when the magnetic field is in-plane. An electric field can then be applied to bias the charge density to either side of the dot, resulting in a spin polarized in z, while both the magnetic and electric field is in the xy-plane. This also has the effect of generating points where zero Zeeman splitting is obtained with finite spin polarization and finite Zeeman splitting is obtained with zero total spin-polarization. The same perturbative analysis with the QDMs can be applied to show sufficient

spin-orbit coupling is needed to generate textured spin. We propose the utilization of spin texture and electric fields as a novel method for rotating the spin in QDs.

In summary, this thesis explores the utilization of an alloyed $GaBi_xAs_{1-x}$ inter-dot barrier for InAs QDMs in order to enhance hole state spin-mixing. We present a detailed analysis of the hole state in QDMs will alloyed barriers using an atomistic TB model. We propose additional corrections to a phenomenological Hamiltonian and fit to the TB energies to obtain empirically relevant parameters. Finally, perturbative analysis of the magnetic field allows us to gather insight of the underlying physics governing resonance behaviors of QDMs. Our conclusions support the use of GaBiAs as a viable material providing significant enhancement to hole state spin-mixing and the general utility of QDMs as a qubit architecture.

Chapter 2: Computational methods

2.1 The tight-binding Hamiltonian

2.1.1 A semi-empirical sps model*

A tight-binding (TB) model assumes a Bloch solution to a lattice structure, with hydrogen-like orbitals as a basis. For bulk materials, empirical values are given for the energies of the orbitals, the on-site TB energy, and the coupling between orbitals on different sites, the TB hopping terms. The exact form of the orbitals themselves need not be specified. The empirical values of the TB model are determined by matching known quantities of the band structure.

A semi-empirical model for various multi-material semiconductor structures can be built from the TB parameters given by bulk materials. Here, we atomisticly model III-V heterostructures of quantum dots and quantum dot molecules. An sp^3s^* TB model is used for III-V semiconductors; the s-orbitals correspond to the electron states, the p-orbitals correspond to the valence states, and the s^*-orbitals are an empirical construction to account for interactions with any other orbitals. Often times, $sp^3d^5s^*$ TB models are considered, particularly for Group IV materials with indirect bandgaps and valley states. However, d-orbitals have minimal impact at the zone center, and thus not necessary for the direct bandgap materials used in structures studied for the thesis, where the sp^3s^* model will suffice.

We chose to implement an atomistic TB model, as it is much faster than ab initio methods like density functional theory (DFT), but still includes atomistic effects as every atom in the lattice is described. Spatial detail at the atomic level is not described in effective mass theories. Atom-level spatial information is particularly useful, in our case, for studying the complex spin interactions of these highly strained structures.

Formally, our zero field TB Hamiltonian, with orbital α on site n, is written as

$$\left\langle \alpha', n'|H_0|\alpha, n\right\rangle = \delta_{\alpha\alpha'}\delta_{nn'}\epsilon^0_{\alpha n} + t^0_{\alpha\alpha'}(\vec{R}_n, \vec{R}_{n'}), \tag{2.1}$$

where $\vec{R}_n$ is the real space position of site n, $\epsilon^0_{\alpha n}$ are the onsite energies, and $t^0_{\alpha\alpha'}$ are the offsite hopping energies. Assuming a nearest neighbor tight binding model enforces that $t^0_{\alpha\alpha'}(\vec{R}_n, \vec{R}_{n'}) = 0$ unless n and n' are nearest neighbors. A spin-orbit term can be added as an onsite inter-orbital coupling, $H = H_0 + H_{SO}$, where

$$\left\langle \alpha', n'|H_{SO}|\alpha, n\right\rangle = \delta_{nn'}U_{SO,n}\left\langle \alpha'|\vec{S}\cdot\vec{L}|\alpha\right\rangle \equiv \delta_{nn'}\Delta_{\alpha\alpha'}. \tag{2.2}$$

Different atom types will have their own spin-orbit coupling strength represented by $U_{SO,n}$, which can be absorbed into the overall intra-site inter-orbital spin-orbit strength $\Delta_{\alpha\alpha'}$

2.1.2 Electric and magnetic fields

In order to study the effects of alloying on spin-mixing, we need to include electric and magnetic fields in our TB Hamiltonian. The formalism for the application of electric and magnetic fields is given in ref. [25]. In addition to the Peierls term and the spin term $(\vec{S}\cdot\vec{B})$ outlined in ref. [25], we have also included a $\vec{L}\cdot\vec{B}$ term for the local atomic orbital angular momentum $\vec{L}$.

The application of an electric field adds a potential at each atomic site corresponding to the electric potential $\Phi(\vec{R}_n)$:

$$\epsilon_{\alpha,\vec{R}_n} \equiv \epsilon^0_{\alpha,\vec{R}_n} - e\Phi(\vec{R}_n). \tag{2.3}$$

The magnetic field also introduces onsite terms. Writing out the indices for the spin and atomic orbital contributions explicitly gives us

$$\left\langle \alpha', n'|\mu_B \left(2\vec{S} + \vec{L}\right) \cdot \vec{B}|\alpha, n \right\rangle = \delta_{nn'}\mu_B \left(2\vec{S}_{\alpha\alpha',n} + \vec{L}_{\alpha\alpha',n}\right) \cdot \vec{B}(\vec{R}_n), \tag{2.4}$$

where μ_B is the Bohr magneton.

Finally, the Peierls term produces an overall phase for the hopping terms in the Hamiltonian, as

$$\begin{aligned}
&\left\langle \alpha', n'|H\left(\vec{r}, \vec{p} + e\vec{A}(\vec{r})\right)|\alpha, n\right\rangle \\
&\quad = \exp\left[-\frac{ie}{\hbar}\int^{\vec{R}_{n'\alpha'}} \vec{A}(\vec{s}) \cdot d\vec{s}\right] \\
&\qquad \times \left\langle \alpha', n'|H\left(\vec{r}, \vec{p}\right)|\alpha, n\right\rangle \exp\left[\frac{ie}{\hbar}\int^{\vec{R}_{n\alpha}} \vec{A}(\vec{s}) \cdot d\vec{s}\right] \\
&\quad = \exp\left[-\frac{ie}{\hbar}\int_{\vec{R}_{n\alpha}}^{\vec{R}_{n'\alpha'}} \vec{A}(\vec{s}) \cdot d\vec{s}\right] \left\langle \alpha', n'|H\left(\vec{r}, \vec{p}\right)|\alpha, n\right\rangle .
\end{aligned} \tag{2.5}$$

There are no on-site hopping terms, thus the integral is zero for $\vec{R}_n = \vec{R}_{n'}$. The remaining hopping terms we can define as

$$t_{\alpha\alpha'}(\vec{R}_n, \vec{R}_{n'}) \equiv \exp\left[-\frac{ie}{\hbar}\int_{\vec{R}_{n\alpha}}^{\vec{R}_{n'\alpha'}} \vec{A}(\vec{s}) \cdot d\vec{s}\right] t^0_{\alpha\alpha'}(\vec{R}_n, \vec{R}_{n'}). \tag{2.6}$$

Therefore, our final Hamiltonian is

$$\begin{aligned}\left\langle \alpha', n'|H|\alpha, n\right\rangle =&\delta_{\alpha\alpha'}\delta_{nn'}\epsilon_{\alpha n} \\ &+ \delta_{nn'}\Delta_{\alpha\alpha'} \\ &+ \delta_{nn'}\mu_B\left(2\vec{S}_{\alpha\alpha',n} + \vec{L}_{\alpha\alpha',n}\right)\cdot\vec{B}(\vec{R}_n) \\ &+ t_{\alpha\alpha'}(\vec{R}_n, \vec{R}_{n'}),\end{aligned} \tag{2.7}$$

with

$$\begin{aligned}\epsilon_{\alpha,\vec{R}_n} &\equiv \epsilon^0_{\alpha,\vec{R}_n} - e\Phi(\vec{R}_n) \\ t_{\alpha\alpha'}(\vec{R}_n, \vec{R}_{n'}) &\equiv \exp\left[-\frac{ie}{\hbar}\int_{\vec{R}_n}^{\vec{R}_{n'}}\vec{A}(\vec{s})\cdot d\vec{s}\right] t^0_{\alpha\alpha'}(\vec{R}_n, \vec{R}_{n'}).\end{aligned} \tag{2.8}$$

2.1.3 Computational implementation and gauge choice

2.1.3.1 Lattice relaxation

First, a large perfect lattice of $144a \times 144a \times 45a$ is created (a being the lattice constant). A file stores the position, material, and species of all the atoms in the lattice. Since the lattice is unrelaxed, atomic positions are stored in units of lattice constants and assumed to be on a perfect lattice.

The strain from mismatch in the lattice constants of the different materials needs to be accounted for in the TB parameters. A valence force field (VFF) model is used to calculate strain relaxed atomic positions. The VFF model treats the atoms as masses on springs. Each material type is given a relaxed spring length (the natural bond length of the material d_0), a longitudinal spring constant (short range force parameter α), and a dihedral spring constant (short range force parameter β). The

program for calculating the relaxed atomic positions was provided by Professor Michał Zieliński of the Institute of Physics, Nicolaus Copernicus University.

Starting with the unrelaxed lattice, the VFF model is used to calculate the overall potential energy caused by the strain of mismatched lattice constants. The material of every atom of the lattice is taken into consideration when calculating the strain energy. The relaxed atomic positions are obtained by minimizing the potential energy via gradient descent. A boundary condition to simulate a lattice substrate is applied, where the atomic positions at the bottom face of the computational box matches that of a perfect lattice of the substrate material. The large lattice size is necessary in order to satisfy this boundary condition. A smaller lattice, now with the relaxed atomic positions, is cut out to create the TB Hamiltonian.

2.1.3.2 Gauge choices and solving for eigenstates

A $50a \times 50a \times 34a$ cutout of the relaxed lattice is used to create the atomistic TB Hamiltonian. Each atom is represented by the sps^* on-site, spin-orbit, and hopping parameters for the corresponding material. The on-site energy parameters are chosen to set the VBE to zero. A valence band offset (VBO) is then required to shift all of the on-site energies, ensuring the correct relative VBE offset between materials. Typically the VBO is taken from experiment. Atoms at the boundary of two materials will have its on-site parameters averaged between its nearest neighbors. For a periodic boundary condition, the atoms at the edge of the computational box has hopping terms connecting with the atoms on the opposing side of the box, which a phase determined by the k-vector being studied. For a non-periodic, hard-walled, boundary condition, any dangling bonds at the edge of the computational box are removed from the calculation by increasing the dangling bond energy by an amount large enough to push any dangling bond states far above any bands in the model. The hopping

parameters at each atomic site are scaled by the strain relaxed bond calculated by the new atomic positions. Once the lattice TB Hamiltonian is constructed, electric and magnetic fields can be added by modifying the Hamiltonian.

Since only constant uniform electric fields are studied, the scalar potential is the field strength times the distance from the origin. In the case of electric fields applied in the stacking direction of the dot,

$$\Phi(\vec{R}_n) = -Ez_n. \tag{2.9}$$

The origin for z_n is arbitrarily chosen. While the choice of origin does not affect the underlying physics, it does change the final eigenenergies. Having the origin be the bottom of the lower dot is useful when comparing how the energies of the two dots scale with electric field. The calculated potential is then added to the corresponding on-site terms in the TB Hamiltonian before diagonalization.

The spin and atomic orbital contributions of the magnetic field, $\vec{S} \cdot \vec{B}$ and $\vec{L} \cdot \vec{B}$, while easy to calculate, have orbital dependency. Like the spin-orbit term, the spin and orbital contributions introduces an inter-orbital coupling for each atomic on-site term. Therefore, the spin and atomic orbital contributions are not stored on file, and need to be calculated for each iteration of the diagonalization process.

Finally, for a constant uniform magnetic field, we can simplify the calculation with the gauge choice of $\vec{A} = -\frac{1}{2}\vec{B} \times \vec{r}$. We have

$$\begin{aligned}
&\exp\left[-\frac{ie}{\hbar}\int_{\vec{R}_n}^{\vec{R}_m} \vec{A}(\vec{s},t)\cdot d\vec{s}\right] \\
&\quad\approx \exp\left[-\frac{ie}{\hbar}\left(\frac{\vec{A}(\vec{R}_{n'})+\vec{A}(\vec{r}_n)}{2}\right)\cdot\left(\vec{R}_{n'}-\vec{R}_n\right)\right] \\
&\quad= \exp\left[-\frac{ie}{2\hbar}\left(\frac{-\vec{B}\times\vec{R}_{n'}-\vec{B}\times\vec{R}_n}{2}\right)\cdot\left(\vec{R}_{n'}-\vec{R}_n\right)\right] \\
&\quad= \exp\left[-\frac{ie}{2\hbar}\left(\vec{B}\times\left(\frac{\vec{R}_n+\vec{R}_{n'}}{2}\right)\right)\cdot\left(\vec{R}_n-\vec{R}_{n'}\right)\right].
\end{aligned} \tag{2.10}$$

This allows us to write all our expressions in terms of the magnetic field rather than the vector potential. Like the electric field, the gauge choice for the magnetic field is arbitrary.

For smaller systems, the Peierls term can be calculated on demand during the diagonalization process. For the QDM systems, in order to lessen the computational load, the TB hopping terms modified by the Peierls contribution are calculated on a local machine and stored to file, before the diagonalization of the TB Hamiltonian in performed on a computational cluster with distributed memory. Diagonalization is carried out with the ARPACK implementation of the Arnoldi method, typically using four distributed nodes totaling 60 parallel threads, taking a few hours to a day to find 12 eigenstates. The addition of a magnetic field significantly increases the computational time needed. Obtaining TB wavefunctions without a magnetic field applied, and then using perturbation theory to apply the magnetic field is substantially cheaper computationally.

2.2 Perturbative analysis of magnetic fields

2.2.1 Three first order magnetic contributions

Heuristically, the magnetic field response has three contributing factors: the spin of the state ($\vec{S}$), the orbital state at each atomic site ($\vec{L}$), and the overall orbital motion of the wavefunction from the Peierls transformation. Under the tight binding model, the magnetic field dependent terms are,

$$\delta_{nn'}\mu_B \left(2\vec{S}_{\alpha\alpha',n} + \vec{L}_{\alpha\alpha',n}\right) \cdot \vec{B}(\vec{R}_n) \tag{2.11}$$

and

$$\exp\left[-\frac{ie}{\hbar}\int_{\vec{R}_n}^{\vec{R}_{n'}} \vec{A}(\vec{s},t)\cdot d\vec{s}\right] t^0_{\alpha\alpha'}(\vec{R}_n,\vec{R}_{n'}). \tag{2.12}$$

Previously, each term was incorporated into the full TB Hamiltonian, and each magnetic field strength had a separate Hamiltonian that needed to be diagonalized. A computationally cheaper method is to apply a first order perturbation to the degenerate, zero magnetic field, TB wavefunctions with the same three terms.

In reference to Equation 2.7, we find that the zero magnetic field Hamiltonian is

$$H^{B=0}_{\alpha\alpha',nn'} = \delta_{\alpha\alpha'}\delta_{nn'}\epsilon_{\alpha n} + \delta_{nn'}\Delta_{\alpha\alpha'} + t^0_{\alpha\alpha'}(\vec{R}_n,\vec{R}_{n'}). \tag{2.13}$$

From which, we can define a perturbation $H = H^{B=0} + H^1(B)$ by taking the first order expansion of the Peierls exponential:

$$\begin{aligned}
&H^1_{\alpha'\alpha,nn'}(B) \\
&\quad\approx \delta_{nn'}\mu_B\left(2\vec{S}_{\alpha\alpha',n} + \vec{L}_{\alpha\alpha',n}\right)\cdot\vec{B}(\vec{R}_n) \\
&\qquad + \left[-\frac{ie}{\hbar}\int_{\vec{R}_n}^{\vec{R}_{n'}}\vec{A}(\vec{s})\cdot d\vec{s}\right] t^0_{\alpha\alpha'}(\vec{R}_n,\vec{R}_{n'}) \\
&\quad= \delta_{nn'}\mu_B\left(2\vec{S}_{\alpha\alpha',n} + \vec{L}_{\alpha\alpha',n}\right)\cdot\vec{B}(\vec{R}_n) \\
&\qquad - \frac{ie}{2\hbar}\left[\left(\vec{B}\times\left(\frac{\vec{R}_n+\vec{R}_{n'}}{2}\right)\right)\cdot\left(\vec{R}_n-\vec{R}_{n'}\right)\right] t^0_{\alpha\alpha'}(\vec{R}_n,\vec{R}_m) \\
&\quad= \delta_{nn'}\mu_B\left(2\vec{S}_{\alpha\alpha',n} + \vec{L}_{\alpha\alpha',n}\right)\cdot\vec{B}(\vec{R}_n) \\
&\qquad + \frac{ie}{2\hbar}(\vec{B}\cdot\vec{n}_{nn'})\ t^0_{\alpha\alpha'}(\vec{R}_n,\vec{R}_{n'}),
\end{aligned} \tag{2.14}$$

where we have assumed the same gauge as previously, $\vec{A} = -\frac{1}{2}\vec{B}\times\vec{r}$, and simplified the previous expression of Eq. 2.10 to

$$\begin{aligned}
\frac{ie}{\hbar}\int_{\vec{R}_n}^{\vec{R}_{n'}}\vec{A}(\vec{s})\cdot d\vec{s} &= \frac{ie}{2\hbar}\left(\vec{B}\times\left(\frac{\vec{R}_n+\vec{R}_{n'}}{2}\right)\right)\cdot\left(\vec{R}_n-\vec{R}_{n'}\right) \\
&= -\frac{ie}{2\hbar}\vec{B}\cdot\left(\vec{R}_n\times\vec{R}_{n'}\right) \\
&= -\frac{ie}{2\hbar}\vec{B}\cdot\vec{n}_{nn'},
\end{aligned} \tag{2.15}$$

with $\vec{n}_{nn'} = \left(\vec{R}_n\times\vec{R}_{n'}\right)$.

Perturbation theory is particularly useful when calculations with multiple directions of magnetic field are needed, such as calculating the g-tensor. It also allows us to more easily consider the three separate contributing terms of the magnetic field, namely, the spin contribution $\vec{S}\cdot\vec{B}$, the atomic orbital contribution $\vec{L}\cdot\vec{B}$, and the spatial/wavefunction orbital contribution also known as the Peierls term. Under the

perturbative Hamiltonian, the contribution from the Peierls term is also linear with magnetic field strength, allowing us to represent the total spatial angular momentum of the wavefunction as $\vec{l}^{\text{eff}}$ and its corresponding magnetic contribution as $\vec{l}^{\text{eff}} \cdot \vec{B}$.

2.2.2 Splitting spin-degenerate TB wavefunctions

From diagonalization of the TB Hamiltonian without a magnetic field, we obtain TB wavefunctions as degenerate pairs of spin states in the form of Kramer doublets, $|\psi_1\rangle$ and $|\psi_2\rangle$. Using the first order perturbative Hamiltonian (Eq. 2.14) we write the four element matrix

$$H^1_{ij} = \left\langle \psi_i | H^1(B) | \psi_j \right\rangle . \tag{2.16}$$

Eigenvalues of H^1_{ij} give us the first order perturbations to the energy; eigenvectors give us the linear combination of $|\psi_1\rangle$ and $|\psi_2\rangle$ to construct the perturbed wavefunction. The first order magnetic splitting can be easily calculated from the perturbed energies.

Both the construction and diagonalization of H^1_{ij} are computationally cheap. This allows us to calculate the first order effects of a magnetic field, namely the splitting, for various directions of magnetic field within a reasonable computational time. By selectively including only the $\vec{S} \cdot \vec{B}$, $\vec{L} \cdot \vec{B}$, or the Peierls term in $H^1(B)$, we can also obtain the splitting contribution of each term independently. For the full TB calculation with an magnetic field, each different direction of magnetic field or each separate inclusion of the three different contributions would take hours to compute on a parallel architecture with distributed memory across multiple nodes. The implementation of perturbation theory allows us to run only one TB calculation, without a magnetic field. The subsequent perturbative calculations take minutes, for each setup, to complete on

local workstations. We will use the breakdown of these three contributions to the magnetic splitting to understand how the alloy affects the resonance behavior of QDMs

2.3 Modeling QDMs with the tight-binding Hamiltonian

2.3.1 System geometry

We model a QDM consisting of two vertically stacked InAs QDs. Experimentally, the QDM heterostructure would be formed by molecular-beam epitaxial deposition of two consecutive layers of self-assembled InAs QDs, separated by a thin layer of GaAs or GaBiAs acting as a barrier. First, layers of InAs are deposited on the GaAs substrate. Initially forming just the wetting layer, further deposition of the InAs, driven by the strain mismatch between the InAs of the wetting layer and the GaAs of the substrate, then forms the first layer of QDs. The InAs dots are then shaved down to obtain disk-shaped cylindrical dots of uniform height, before being capped with the barrier material. When the second layer of InAs is deposited above the GaAs/GaBiAs barrier, the strain induced by the lattice mismatch between the dot in the first InAs layer and the GaAs/GaBiAs barrier provides a nucleation point for a dot in the top layer to form directly above the dot in the bottom layer [57]. The two InAs dots are thus naturally stacked vertically (along the growth direction). The substrate under the first dot and the cap above the second dot are GaAs; the barrier is engineered to be various GaBiAs/GaAs structures. Details on the growth of these structures can be found in references [47, 57].

All calculations are carried out for cylindrical dots of radius $16.6a$, height $3a$ (not including the wetting layer), and $1a$ thick wetting layers, as shown in Figure 2.1. Dot-to dot separation (wetting layer to wetting layer) is $10a$, unless otherwise noted. The geometry for the QDMs closely resemble those previously studied in [16]. A

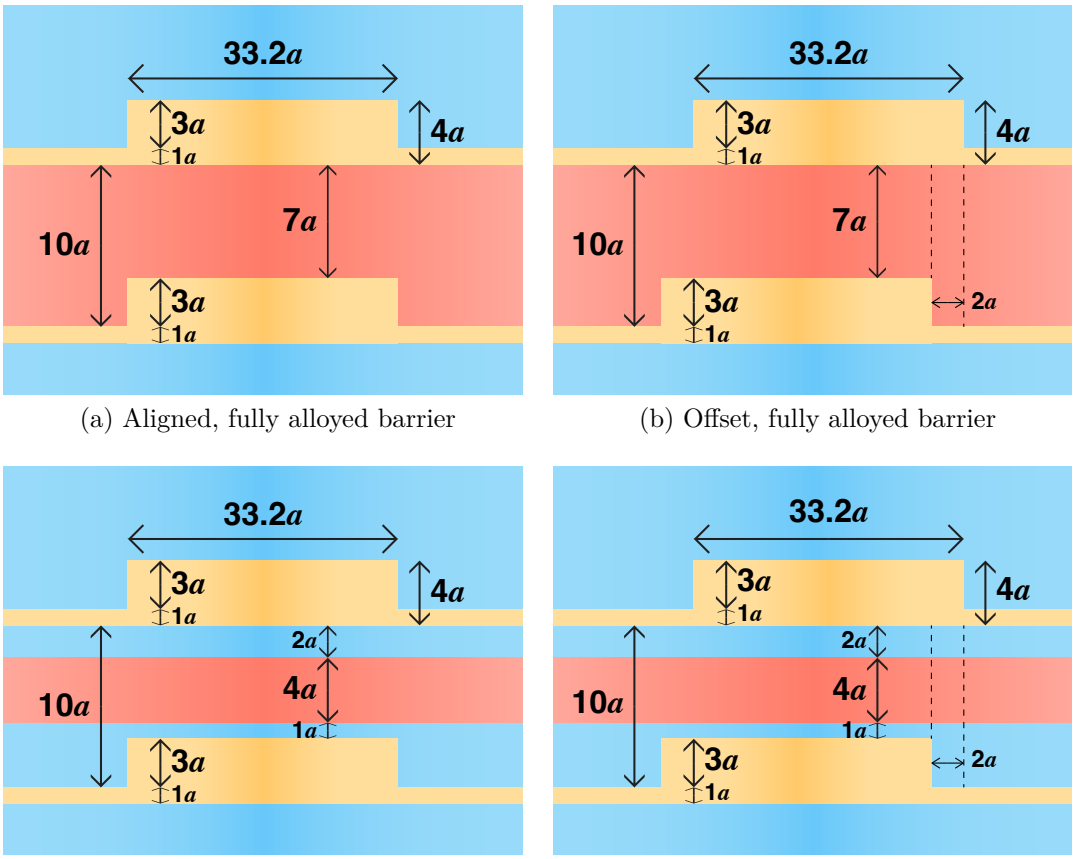

(a) Aligned, fully alloyed barrier

(b) Offset, fully alloyed barrier

(c) Aligned, partially alloyed barrier

(d) Offset, partially alloyed barrier

Figure 2.1: Schematic representation of system geometry. GaAs in blue; InAs in yellow; GaBiAs in red. (a) Aligned dots with alloy spanning the full interdot region. (b) Offset dots with alloy spanning the full interdot region. (c) Aligned dots with alloy as a partial layer inside the barrier. (d) Offset dots with alloy as a partial layer inside the barrier. a represents lattice constants. (x and z axes not to scale.)

lattice of size $144a \times 144a \times 45a$ is used for calculating the strain relaxation via VFF. After the new atomic positions are calculated, a $50a \times 50a \times 34a$ cutout of the relaxed lattice is made. We ensure that the cutout size is large enough to minimize any boundary effects on the quantum dots states. The dot states being bound and not sensitive to the boundary allows us to construct our Hamiltonian from the smaller cutout, saving significant computation time during diagonalization. Lattice strain is accounted for in construction of the TB Hamiltonian. Hopping TB parameters are scaled by the relaxed bond length d as $\left(\frac{d_0}{d}\right)^{\eta}$, where d_0 is the natural, unrelaxed, bond length of the respective material. η for all materials is taken to be 2.9, typical

for the class of materials of interest. The particular value of 2.9 was chosen as it has historically agreed well with experimental results.

2.3.2 Material parameters

The TB model we use for III-V materials include sp^3s^* atomic orbitals and nearest-neighbor hopping [25, 26, 43, 56]. The VFF parameters and bond lengths for the relevant materials are given in Table 2.1. The parameters for InAs and GaAs are taken from Zunger et al. [45], and the parameters for GaBi are taken from O'Reilly et al. [54] (with lattice constant converted to bond length using a zincblende structure). The relaxed atomic positions are used to construct the TB Hamiltonian with the parameters in Table 2.2. The values for InAs and GaAs are from Vogl et al. [56], with proper spin-orbit coupling parameters appended. The TB parameters for GaBi are converted from O'Reilly's σ and π-bond model [54] to a p_x, p_y, and p_z model. The states and wavefunctions of interest are found by iterative diagonalization of the Hamiltonian. Partial diagonalization of the Hamiltonian around a energy value in the band gap allows us to compute the few electron and hole states closest to the band edge.

Table 2.1: Unrelaxed bond length (d_0) and short range force parameters (α and β) for the VFF model.

	InAs[a]	GaAs[a]	GaBi[b]
α (N m^{-1})	35.18	41.49	34.0
β (N m^{-1})	5.49	8.94	5.0
d_0 (Å)	2.622	2.448	2.740

[a] Values from Zunger et al. [45]
[b] Values converted from O'Reilly et al. [54]

Because an atom may be surrounded by different nearest-neighbors, the orbital energies at the atomic site are taken to be the average of the orbital energies it has for each nearest-neighbor, weighted by the number of each neighbor. SO and VBO

parameters are also on-site parameters and therefore incorporated into the Hamiltonian as an average between the materials formed with the nearest-neighbors. At an interface between InAs and GaBiAs, there may be occurrences of InBi. These will be few, so we use the parameters of InAs to describe InBi, as there is no known TB parameter set for InBi. We do not expect the difference between InAs and InBi to alter our results in any significant manor.

Table 2.2: Tight-binding parameters (orbital energies, inter-atomic interaction, spin-orbit coupling and valence band offset) for an sps^* Hamiltonian. A subscript x indicates a p-orbital parallel to an crystal axis. A subscript xx indicates two parallel p-orbitals; a subscript xy indicates two perpendicular p-orbitals. The subscript a and c indicate anion and cation, respectively. All units in eV.

	InAs[a]	GaAs[a]	GaBi[b]
$E_{s,a}$	−9.5381	−8.3431	−8.3774
$E_{s,c}$	−2.7219	−2.6569	−5.6126
$E_{x,a}$	0.9099	1.0414	0.1256
$E_{x,c}$	3.7201	3.6686	1.694
$E_{s^*,a}$	7.4099	8.5914	6.1262
$E_{s^*,a}$	6.7401	6.7386	5.8164
$V_{ss,ac}$	−5.6052	−6.4513	−5.3700
$V_{sx,ac}$	3.0354	4.4800	5.4426
$V_{sx,ca}$	5.4389	5.7839	2.7771
$V_{xx,ac}$	1.8398	1.9546	0.9727
$V_{xy,ac}$	4.4693	5.0779	3.5143
$V_{s^*x,ac}$	3.3744	4.8422	4.1687
$V_{s^*x,ca}$	3.9097	4.8077	1.1778
$U_{so,a}$	0.140	0.140	0.672
$U_{so,c}$	0.000	0.000	0.038 43
VBO	0.0	−0.2	0.9

[a] Values from Vogl et al. [56]
[b] Values converted from O'Reilly et al. [54]

2.3.3 Generating an alloy

For the study of the material itself, smaller GaBiAs lattices of 8 to 1000 atoms are created. These lattices are not strain relaxed and serve as "unit cells," where deliberate placement of the Bi atoms at the center of the cell gives a definitive pre-determined alloy concentration. The TB Hamiltonian is built from these unit cells, with periodic boundary conditions, to represent a larger periodic lattice of the bulk material.

The larger $144a \times 144a \times 45a$ lattice is used in the random alloy model, for both bulk GaBiAs calculations and the QDM systems. We start with a rectangular box of pure GaAs. A pseudo-random number generator is used to select and replace As atoms with Bi in the interdot barrier. A random number between 0 and 1 is generated for each As site in the region meant for alloying, and sites where the number generated is less then or equal to the desired concentration is turned into a Bi atom. For bulk GaBiAs, the entire lattice is transformed into GaBiAs and then strain relaxed. A smaller lattice of $50a \times 50a \times 34a$ is cutout from the relaxed lattice to create a TB Hamiltonian with parameters from Table 2.2. The Hamiltonian no longer has periodic boundary conditions, but a hard-wall with energies of dangling bonds removed. For the QDMs, the Bi atoms are only seeded in the region between where the wetting layers of the two dots would be located. After which, the two quantum dots and their wetting layers are created by replacing the appropriate Ga atoms with In. This lattice is then relaxed, and the smaller cutout is used to generate a tight-binding Hamiltonian.

In addition to the pseudo-random placement of Bi in the alloy, we also compute clustered and ordered alloy distributions. For a clustered alloy, the placement of Bi is performed in two steps. An initial placement of half the desired concentration is placed randomly with a pseudo-random number generator. A second sweep of the lattice is then performed, where each As atom that is a next nearest neighbor to a Bi

placed in the fist sweep has a 10% increase in chance to be replaced with a Bi atom for each neighboring Bi introduced in the first sweep. The overall probability of the second round is normalized such that half the desired concentration of Bi is placed, resulting in the overall concentration after the two rounds to equal the initially desired concentration. In an ordered lattice, if a Bi atom is placed every 2 lattice constants, then with one Bi atom per 8 unit cells, we obtain a periodic lattice of $GaBi_{0.03}As_{0.97}$. If another set of Bi atoms is placed offset by $1a$ in all three lattice directions, resulting in two Bi atoms per 8 unit cells, we have a pseudo-periodic lattice of 6% alloy.

The various eigenenergies and eigenstates obtained from partial diagonalization of the TB Hamiltonians are used to analyze QDMs. Initially, in Chapters 3 and Chapter 4, we will explore the energy levels of bulk GaBiAs and QDMs with a GaBiAs barrier. Starting from Chapter 4, we use the construction of the TB Hamiltonian from the relaxed lattice to selectively apply the strain or orbital effects of the alloy independently. The addition of an electric field to the TB Hamiltonian in Chapter 5 allows us to study the tunnel coupling between the two dots of a QDM. Finally, adding a magnetic field in Chapter 6 and Chapter 7 allows us to explore spin-mixing for QDMs and spin texture for in-plane fields, respectively. Additionally, the TB wavefunctions obtained as eigenstates of the Hamiltonian can be used for various post-analysis, such as applying a perturbative magnetic field on TB wavefunctions obtained without a magnetic field.

Chapter 3: Tight-binding calculations of GaBiAs

*Chapters 3 and 4 reuses content published in Phys. Rev. B **99**, 075308 (2019).*

While GaAs is a typical III–V direct gap semiconductor, GaBi is a negative-gap semiconductor (semimetal). Moreover, Bi has substantially larger spin-orbit coupling than As. GaBiAs alloys are expected to be significantly different from typical III–V alloys and to have significant local spin-orbit interaction that may provide new tools for modifying the hole spin physics of InAs QDMs. The purpose of this chapter is to investigate how GaBiAs alloys should be treated to correctly model their properties in InAs QDMs and to determine which effects of the alloy barriers influence the QDM states.

For this chapter, we start by analyzing the band structure of GaAs and GaBi calculated using an atomistic TB model with a single unit cell and periodic boundary conditions, showing the band inversion present in GaBi. When a single As atom is replaced with Bi to form a $GaBi_{0.25}As_{0.75}$ alloy, the band structure shows the introduction of an additional state under the GaAs valence states, as opposed to the hybridization of the valence band for both materials. This highlights the need for atomistic calculations for random alloy distributions, and the inadequacies of approaches such as virtual crystal approximations (VCAs). We confirm the need for an atomistic approach with large lattices of bulk $GaBi_xAs_{1-x}$ with non-periodic hard-walled boundaries. Finally we have a brief discussion on the spread of the VBE as a result of the random distribution of the alloy at any given concentration.

3.1 Band structure of a periodic lattice

To understand the band structure of GaBiAs random alloys, we begin with periodic models of the alloy. First, we start with simple periodic 8 atom unit cells of GaAs, GaBi, and $GaBi_{0.25}As_{0.75}$. We calculate the folded band structure by diagonalizing the 8 atom TB Hamiltonian. Then, we expand our model to larger unit cells to explore Bi clustering effects.

3.1.1 Periodic calculation of a single unit cell

For pure GaAs and GaBi, the folded bandstructures along k from Γ to $X/2$ are shown in Figure 3.1. GaAs shows the typical behavior of a III-V semiconductor, with a calculated bandgap of 1.44 eV and an SO split-off 0.33 eV below the VBE. GaBi, on the other hand, has an inverted band structure. The consequence, seen in Figure 3.1b, is that the CBE is at -1.45 eV, *below* the VBE (set to 0). Also, the heavy-hole bands increase in energy away from the zone center while the electron and light-hole bands decrease in energy away from the zone center. Finally, the SO band for GaBi lies slightly below the conduction band, at -1.75 eV.

Next, we take an 8 atom unit cell of pure GaAs and replace the center As atom with a Bi atom, simulating a 25% Bi $GaBi_{0.25}As_{0.75}$ alloy where the Bi atoms are periodically spaced in the lattice. All the TB parameters associated with the center As atom and its bonds are replaced with Bi and GaBi, respectively. However, all bond lengths are still taken to be that of GaAs, as the structure is not strain relaxed. Additionally, since the lattice is unrelaxed, the TB parameters are not scaled with changes from natural bond length, despite the GaBi bonds being compressed to match GaAs. Again, we diagonalize this Hamiltonian for a set of k values between the zone

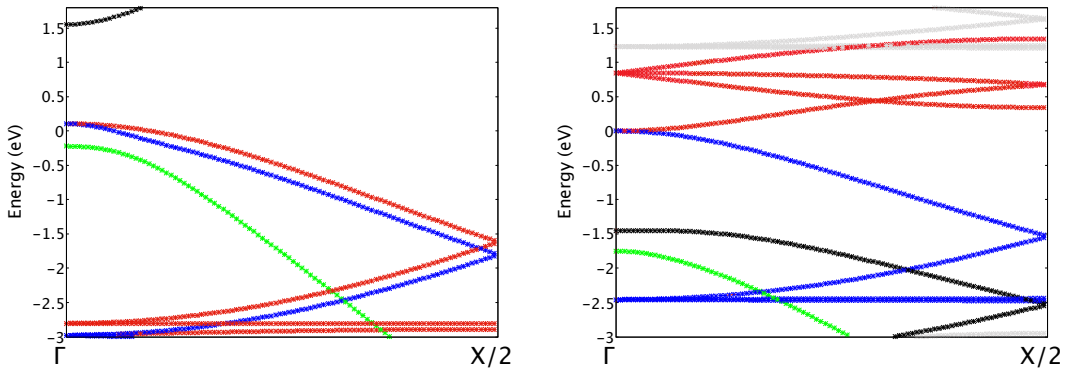

(a) GaAs (b) GaBi

Figure 3.1: Folded band structure of (a) GaAs and (b) GaBi, from Γ to X. For an 8 atom unit cell, the bandstructure is twice folded. Both graphs have the VBE set to 0 (eV) for the respective material. (Black: conduction band edge; Red: heavy holes; Blue: light hole; Green: spin-orbit split off; Grey: other bands)

center (Γ) and the zone boundary X. The resulting band structure, overlaid with the previous results for pure GaAs, are shown in Figure 3.2.

There are two primary features of alloying. First, the alloying reduces the bandgap energy and increases the SO split-off energy. Second, a Bi band exists beneath the VBE at $-2\,\text{eV}$, a feature unique to only a handful of alloy materials. The alloy behaves as a non-traditional alloy as it is a mixture of a semiconductor and a semi-metal with drastically different band structures. The reduction in bandgap energy can be explained under the band anti-crossing (BAC) model, wherein the introduction of a Bi band below the GaAs VBE pushes the alloy VBE up in energy more than traditional alloying [1, 37, 54]. For low alloy concentrations, the Bi energies lay slightly below the VBE of GaAs, resulting in a BAC effect [15, 54]. The BAC effect disappears at higher concentrations, because band broadening occurs and the Bi band starts to overlap with the VBE [15]. In Figure 3.2, there is a single “Bi defect state" at roughly 2 eV below the VBE. There is limited Bi band broadening due to the presence of only a single Bi atom in the unit cell, therefore, we have a clearly visible defect state. The existence of this state supports the BAC model [54].

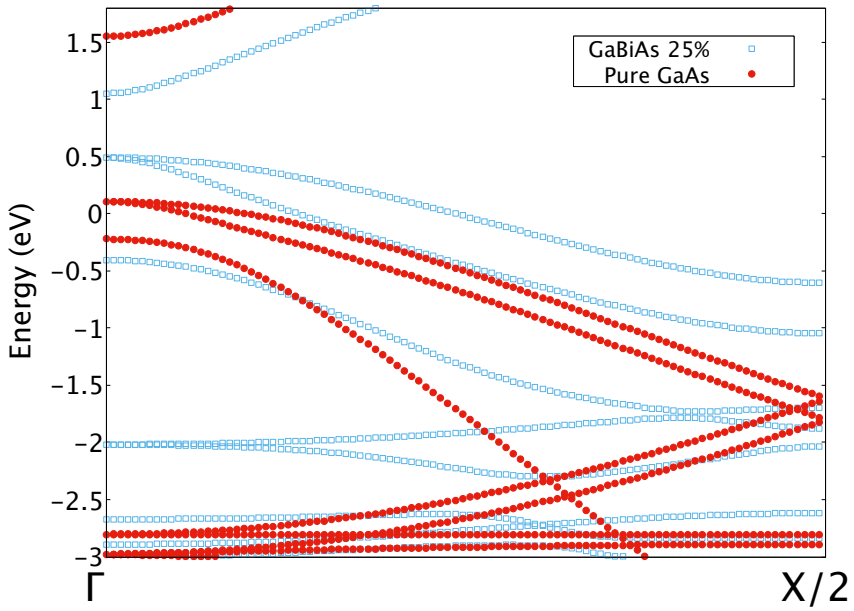

Figure 3.2: Band structure of $GaBi_{0.25}As_{0.75}$ (blue), overlaid on top of pure GaAs (red). One can clearly see the Bi defect state at $-2\,\text{eV}$. Placement of Bi atom at the center of the cell breaks the symmetry, thus, the $GaBi_{0.25}As_{0.75}$ band structure is not folded.

3.1.2 Bi clusters in few unit cell lattices

Studies have suggested that Bi atoms in $GaBi_xAs_{1-x}$ tend to form clusters [5, 6, 35, 54]. We explore clustering by selectively replacing additional As atoms in the original unit cell with Bi. To simulate change in concentration, the size of the unit cell is expanded by adding GaAs equally to all sides. Since all the Bi atoms are located in the original 8 atom cell, the periodic repetition of the structure simulates equally spaced "Bi clusters."

For Bi cluster calculations, we create square structures that are m unit cells in length, where $m = 1, 2, 3, 4, 5$. The total number of atoms in our structure is $8 \times m^3$, or 8, 64, 216, 512, and 1000 atoms. Periodic conditions are identical to the case of the unit cell, but scaled to the size of the structure. For example, the structure with length $m = 2a$ wraps around on itself every 2 lattice constants in each crystal direction. The Bi replacement begins with the anion at the center of the

structure, regardless of structure size. Up to three additional next nearest neighbor anions are replaced with Bi, in the order of $\left[\frac{1}{2}\frac{1}{2}0\right]$, $\left[\frac{1}{2}0\frac{1}{2}\right]$, and $\left[0\frac{1}{2}\frac{1}{2}\right]$. The lattices are unrelaxed, and all the bond lengths of GaAs are kept. TB parameters are not scaled with bond length. Only the energy at the zone center is shown. With this method, there are two variables affecting Bi concentration. One is the number of Bi atoms; the other is the size of the structure. Increasing the structure size lowers the Bi concentration directly, without increasing cluster size. Adding Bi to the system increases the concentration, but results in a greater VBE shift than reducing the structure size by the corresponding amount.

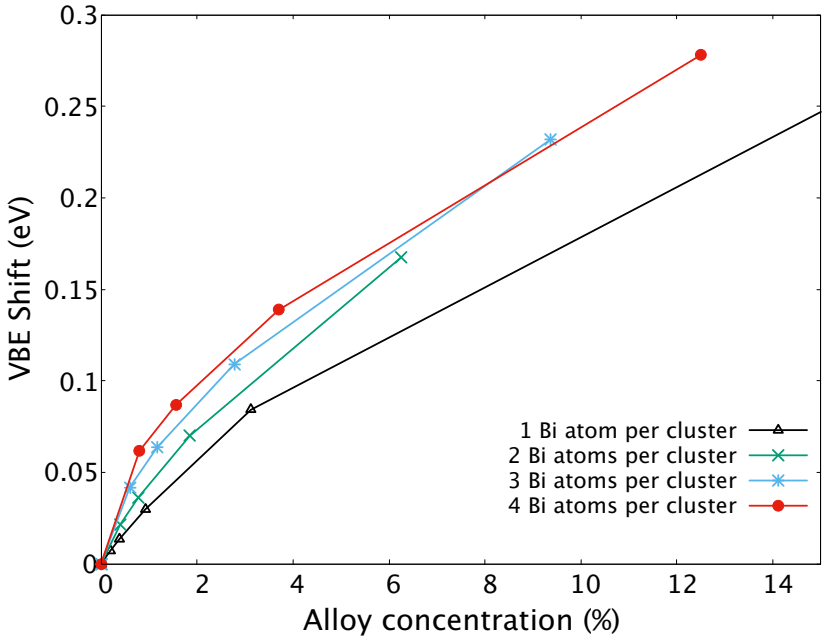

Figure 3.3: VBE shift above GaAs for $GaBi_xAs_{1-x}$ of different concentrations of Bi. Different curves represent a different number of Bi atoms in a cluster (located in the center of the periodic cell). Change in Bi concentration along a curve is created by varying the cell size (the distance between clusters).

The resulting VBE shifts at Γ for the different cell sizes and Bi concentrations are shown in Figure 3.3. Each connected curve represents a given number of Bi atoms per cluster; each data point along a given curve corresponds to a different unit cell size, with larger Bi concentrations for smaller cell sizes. Following each curve, we

find the smaller the cell size, the higher the concentration, and the more the VBE is shifted. Comparing curves, we see that higher Bi atom count per cluster leads to greater rise in energy for the VBE, despite identical Bi concentration. This implies that alloying effects are increased by clustering, consistent with literature [53, 54] For Bi concentrations in the 4% to 10% range, clustering leads to shifts ($\sim$50 meV) that are a sizable fraction of the actual VBE shifts.

3.2 The random alloy approach

To better model actual QDMs, we must consider random alloys of GaBiAs. We take a $144a \times 144a \times 45a$ box of pure GaAs, and use a pseudo-random number generator to select As atoms to replace with Bi. The large lattice is then relaxed using a valence force field (VFF) method to account for strain due to Bi in the alloyed system. A TB Hamiltonian is generated from a $50a \times 50a \times 34a$ cutout of the relaxed lattice. The Hamiltonian is diagonalized to find the states closest to the VBE and CBE. The boundary condition for the VFF is set such that the bond length of the atoms at bottom of the computational box matches that of a pure GaAs lattice. The TB Hamiltonian is setup without a periodic boundary condition between opposing sides of the box. Any dangling bonds caused by the hard boundary at the end of the computational box are removed by raising the orbital energies by 200 eV. The results are shown as the black curves in Figure 3.4.

Also shown in Figure 3.4 are results from using a virtual crystal approximation (VCA) to model alloying. In the VCA model, the alloy is treated as a regular lattice of GaX, where the VFF and TB parameters for X are the concentration-dependent averages between parameters for As and Bi. The VCA energies have a linear dependence on alloy concentration. Although both the VCA model and the random alloy approach show a bandgap reduction of roughly 30 meV/%, only the random alloy

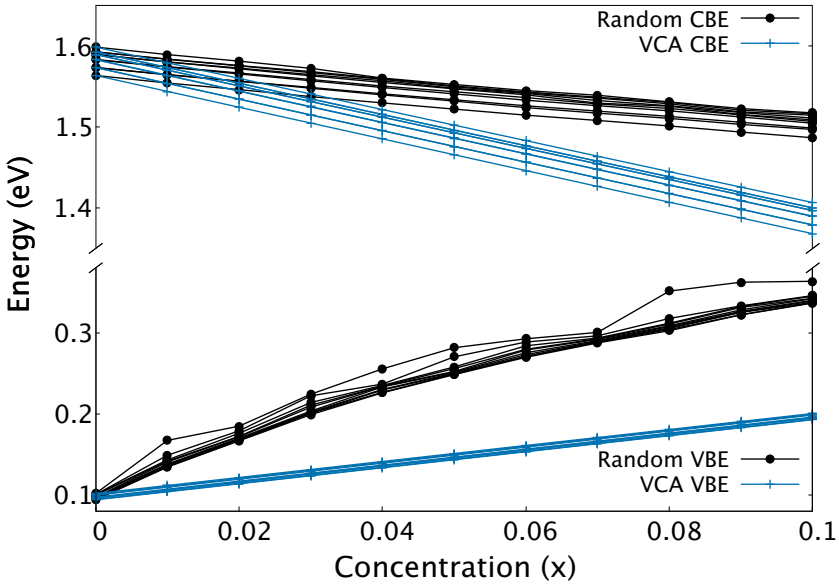

Figure 3.4: Energy levels of $GaBi_xAs_{1-x}$ plotted against Bi concentration (x), for a random alloy approach (black) and a VCA model (blue). The zero on the energy scale here is set to the VBE for GaAs. The initial (0% Bi) deviation from a perfect 0 eV GaAs VBE is caused by spin-orbit effects, offsetting the actual VBE from the VBO provided by Vogl [56].

case correctly captures bowing of the VBE. In addition, as indicated in Table 3.1, the VBE shift obtained with a VCA model is smaller than the prediction of O'Reilly's [54] and experimental results [1, 22, 35, 59]. The failures of the VCA model shows the necessity of including the individual Bi atoms, and reaffirms the importance of the BAC model. The results for our random alloy model do differ slightly from O'Reilly's but can be explained by a difference in strain models. Our results show that an atomistic treatment of Bi is needed to correctly predict the properties of $GaBi_xAs_{1-x}$, which would be a random alloy in real materials.

With the random alloy model, we also study the spread of energies stemming from variations in alloy configuration. These variations are not accounted for by the VCA nor in a periodic model. For the case of 7% Bi, 40 different alloy configurations (placement of Bi atoms) are generated by the pseudo-random number generator. Each configuration is relaxed and diagonalized independently. The resulting energies

Table 3.1: Band edge shift per alloy percentage (slope in Figure 3.4) for $GaBi_xAs_{1-x}$. Two values taken, one between 0 and 1%, the other between 9 and 10%. Values from O'Reilly et al., where the system was a smaller random alloy with periodic boundaries, are shown for comparison [54]. The gap energy, E_g, decreases by the combined amount of the VBE and CBE shifts.

Change per percent alloy (meV/%)	CBE	VBE	E_g
VCA (1%)	−19	9.8	−28.8
VCA (10%)	−19	9.8	−28.8
Alloy (1%)	−9.2	66	−75.2
Alloy (10%)	−5.4	11	−16.4
Periodic [54] (2%)	−28	53	−81
Periodic [54] (12%)	−28	30	−58

closest to the band edges for each configuration are shown in Figure 3.5. We see a 50 meV spread for the VBE and a 10 meV spread for the CBE. In conjunction with Figure 3.4 and Table 3.1, we see that the configurational variances accounts for a large portion of the difference between our predicted energies and O'Reilly's. The remaining discrepancies between the random alloy results and O'Reilly's paper can be attributed to the difference between non-periodic and periodic boundary conditions, as well as the fact that we have a different model for strain relaxation. A later paper by O'Reilly et al. [53], where $GaBi_xAs_{1-x}$ was placed on top of a GaAs substrate (consistent with our strain model), shows band edge shifts in agreement with our random alloy results.

In conclusion, for a periodic system, we have reaffirmed the existence of a Bi state below the band edge which pushes the VBE up through band anti-crossing. Stronger alloy effects emerge from more densely clustered Bi. For large non-periodic lattices, the VBE shift of the random alloy model is consistent with literature, while the VCA model is not consistent with random alloy results. Furthermore, the VBE of the random alloy model shows signs of bowing, an effect of band anti-crossing [1, 54], where the VCA model failed to show signs of BAC. Additionally, the spread in energies at the VBE for the random alloy case is a combined effect of configurational dependence

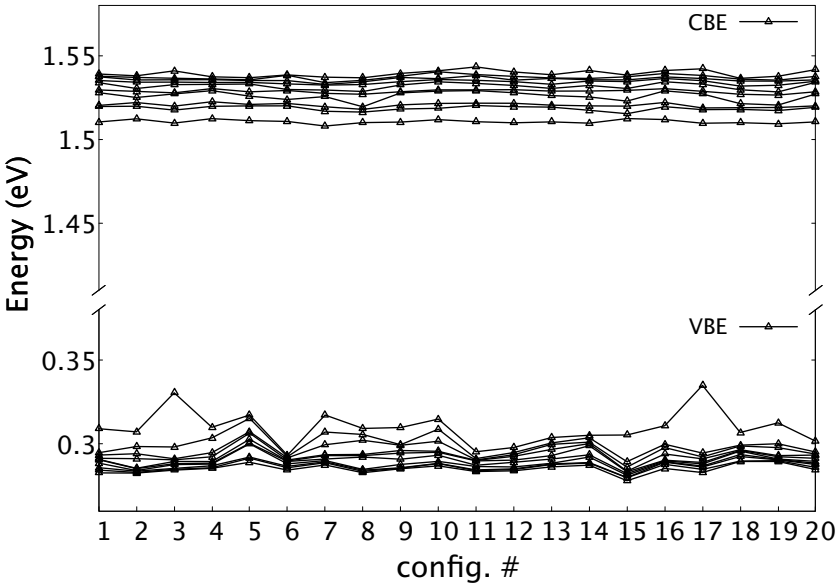

Figure 3.5: Band edge energies for various random alloy configurations with a $GaBi_{0.07}As_{0.93}$ cell of nearly 700,000 atoms. The zero on the energy scale here is set to the VBE for GaAs. Data points are connected via curves solely for better visualization.

and strain [53]. While the valence band is sensitive to both strain and configuration due the band-anticrossing, the lack of band-anticrossing in the CB removes most of the configurational dependence from the CBE. These results show that an atomistic treatment is necessary to correctly model the properties of $GaBi_xAs_{1-x}$. Most importantly, an atomistic treatment is needed to capture the VBE shift, which significantly determines effects from changes in the barrier in a QDM.

Chapter 4: Hole state energies in InAs/GaBiAs double dots

In this chapter, we assess the sensitivity of the QDM states to random fluctuations in the alloy configuration as well as Bi clustering in the alloy barrier. Our results show that an atomistic treatment is necessary to properly account for the alloy effects. We separately investigate the effects of (1) the strain induced when the larger Bi replaces the smaller As and (2) the effects when the As energy levels are replaced by Bi orbitals and energy levels, i.e., the scattering induced when Bi replaces As. We find that the induced strain is a global effect, affecting the system beyond just the alloy region. The strain on the dots caused by the alloy raises the energy of the dot hole states, resulting in a competition with the lowering of energy that one would expect from reducing a confinement barrier. Additionally, any asymmetry in strain between the two dots causes a change in the energy difference between the corresponding hole states of each dot. In the case where the entire inter-dot region is alloyed, the bottom dot receives less strain, and the energy difference between the corresponding top and bottom dot states increases.

4.1 Alloy concentration

We first consider a QDM with GaBiAs everywhere between the InAs QDs and wetting layers (as shown in Figure 2.1a). Energies obtained from the VCA model are shown in Figure 4.1 (blue), in comparison with results obtained for a random alloy configuration (black). From here on, we shall make the distinction between QD hole/electron states and the valence/conduction band states. The nomenclature

"holes" and "electrons" shall be reserved for the states confined within the QDs, whereas valence band and conduction band shall refer generally to electron states below or above the bulk bandgaps. All energy plots will show conduction electron and valence electron energies. Due to convention, an increase in hole state energy is a decrease in valence electron energy, and vice versa.

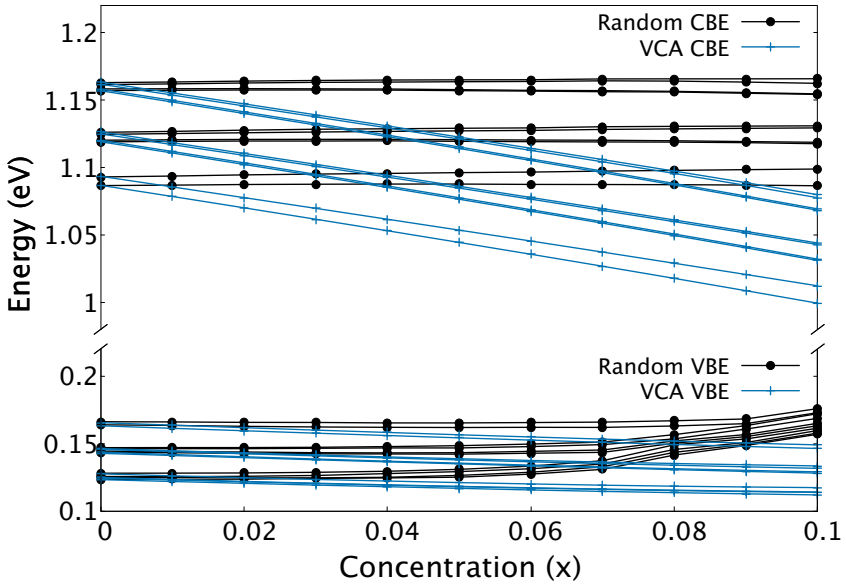

Figure 4.1: Energy levels of an InAs QDM with full $GaBi_xAs_{1-x}$ barrier, calculated with a random alloy approach (black) and the VCA (blue). Zero on the energy scale here and in remaining figures is set to the VBE for InAs, which is 0.2 eV above the GaAs VBE.

As shown in Figure 4.1, electron states confined to the dots are weakly affected by the presence of Bi, due to the relatively small $GaBi_xAs_{1-x}$ CBE energy shift. The larger energy difference between the dot electron states and the barrier $GaBi_xAs_{1-x}$ CBE also weakens the barrier alloy effects as compared to the holes. From Figure 3.4, we see that the CBE for bulk $GaBi_xAs_{1-x}$ is about 0.3 eV above that of the InAs QD electron states (after accounting for the VBO between GaAs and InAs). The atomistic treatment of Bi accounts for local Bi effects, without distorting the electron structure globally, as would happen in the VCA.

The hole state energies in Figure 4.1 are initially flat, weakly dependent on Bi concentration, because the lowest energy hole states are well confined to the InAs dots. In the random alloy model, this breaks down at higher concentrations of Bi, when the GaBiAs barrier VBE is pushed up into the same energy region as the confined QD hole states. This results in a breakdown of confinement at 9% to 10% Bi.

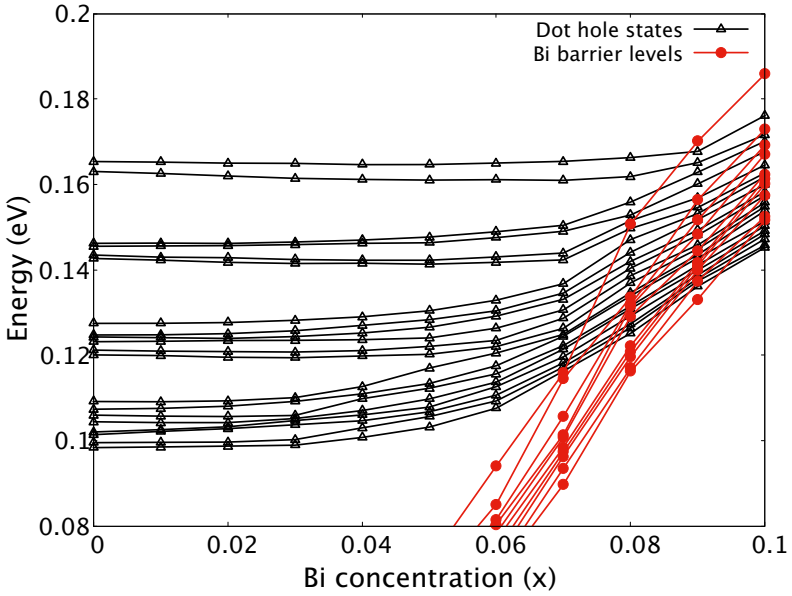

Figure 4.2: Comparison of GaBiAs barrier valence band energy levels (red) with random alloy InAs QD hole state energy levels (black). Bi barrier energy levels were calculated as a layer of $GaBi_xAs_{1-x}$ in a larger lattice of GaAs.

The interaction between the dot hole states and the barrier VBE is supported by the fact that the hole states are close in energy to the valence band of bulk $GaBi_xAs_{1-x}$ at $x \approx 7\%$. We see the distortion of the dot hole state energy levels as the concentration of Bi in the barrier surpasses this percentage. To further illustrate this, we calculate the energies with the two InAs dots and wetting layers replaced with GaAs, leaving just the $GaBi_xAs_{1-x}$ sandwiched between GaAs. The energies for this $GaBi_xAs_{1-x}$ layer are compared with the energies for the InAs dots in Figure 4.2. This better illustrates the distortion of the dot energy levels with respect to the encroaching Bi band energy levels. This also indicates that, past 8% Bi, the valence states need not be

confined solely to the QDs. Wavefunction plots confirm that, for 10% Bi, significant hole probability is found in the Bi barrier region rather than in the InAs dots.

4.2 Alloy configuration

To test the effect of alloy configuration, we consider InAs QDMs with 7% Bi in the GaBiAs barrier. At this percentage, the GaBiAs VBE overlaps with the hole states in the QDM. For the bulk $GaBi_xAs_{1-x}$ (Figure 3.5), there is a 10 meV spread in CBE energies and a 50 meV spread in VBE energies caused by different configurations. The spread of CBE and VBE energy levels for 20 configurations of a $10a$ layer of $GaBi_{0.07}As_{0.93}$ in GaAs are shown in Figure 4.3 (red). The alloy configurations in Figure 4.3 have no relation to those in Figure 3.5.

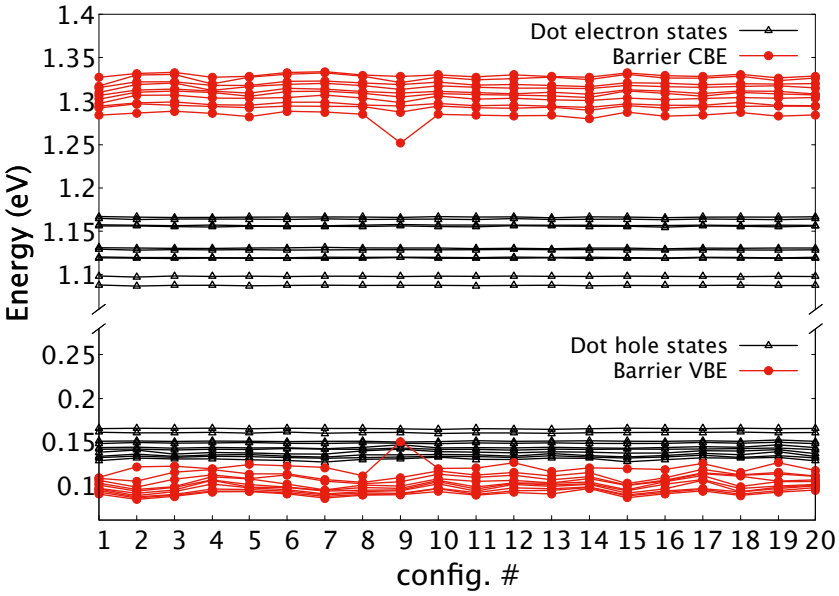

Figure 4.3: Band edge states for various random alloy configurations of a $10a$ layer of $GaBi_{0.07}As_{0.93}$ in GaAs (red), and QDM states from using the respective alloy configuration as the interdot barrier (black). The plot shows the variation caused by the random distribution of Bi and the much larger separation between the barrier CBE and the dot electron states in contrast to the VBE and hole states. Zero on the energy scale is set to the VBE for InAs.

The alloy band edges of Figure 3.5 and Figure 4.3 are similar, with the exception of one case for the CBE. This is an artifact of a particular alloy configuration and is a very rare occurrence. Of the 41 alloy configurations we tested, configuration # 9 was the only case to have a significant deviation in the CBE. Looking at the VBE, it might seem that there is more of a spread for a $10a$ layer of GaBiAs in GaAs, compared to bulk GaBiAs. However, the states are less dense because fewer Bi atoms are included in the computational box. This is not a configurational effect. Disregarding case # 9, the spread in VBE of the GaBiAs barrer is still roughly 50 meV.

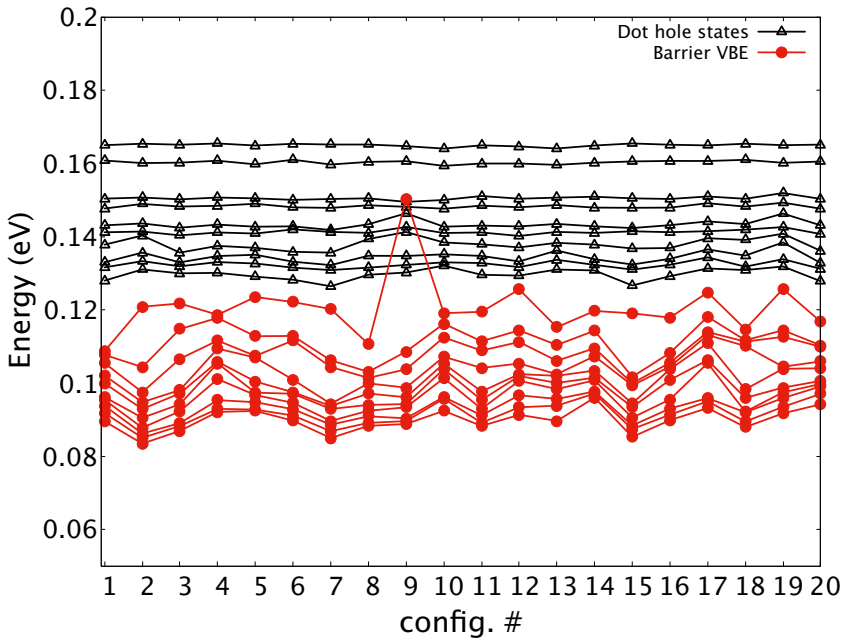

Figure 4.4: Zoomed in cut of Figure 4.3. Valence edge states for various random alloy configurations of a $10a$ layer of $GaBi_{0.07}As_{0.93}$ in GaAs (red), and QDM states from using the respective alloy configuration in the interdot barrier (black). Zero on the energy scale is set to the VBE for InAs.

The effect of alloy configuration on the QDM electron and hole states is also shown in Figure 4.3. We take the GaAs lattice with a GaBiAs barrier shown in red in Figure 4.3 and add the InAs dots. The alloy configuration with and without the dots remains the same for the same configuration numbers. The resulting dot states are shown in Figure 4.3 (black). The electron states remain largely unaffected by alloy

configuration, as expected. The configurational change of the $GaBi_xAs_{1-x}$ CBE is too small and too far away to significantly affect the behavior of the dot electron states. However, the hole states do see the $GaBi_xAs_{1-x}$ VBE, because, for $x = 0.07$, the alloy VBE energetically overlaps with the hole states. Figure 4.4 shows a zoomed in view of the GaBiAs VBE and the QDM hole states. At 7% alloy, the ground and first excited QDM hole states retain their structure regardless of alloy configuration; the remaining states are shifted to varying degree, roughly correlated to how close the $GaBi_{0.07}As_{0.93}$ VBE is to the dot states.

4.3 Alloy induced strain effects and system geometry

4.3.1 Layered GaBiAs barrier

We also consider the case where only a $4a$ layer within the interdot region is alloyed (see Figure 2.1b). The overall barrier thickness remains the same, but is now a sandwiched structure of GaAs/GaBiAs/GaAs. This shows how the thickness of the alloy barrier region can influence the QDM states. The resulting hole energies, overlaid with the dot hole energies with the full GaBiAs barrier are shown in Figure 4.5.

There are two key things to note. First, for the layered GaBiAs barrier, the upward shift in valence energy doesn't occurs until a higher concentration of Bi, indicating that the QD hole states are less perturbed by the alloy region, despite having the same concentration of Bi within the alloy layer. Second, for the full GaBiAs barrier there is a larger energy difference between equivalent top and bottom dot states (i.e., $E_{v1} - E_{v2}$, $E_{v3,v4} - E_{v5,v6}$, etc.), than for the layered barrier. This is because, in the former case, there is Bi present above and around the sides of the bottom dot, whereas Bi is only present below the top dot. This geometry of the GaBiAs layer breaks the symmetry between the top and bottom dots. On the other hand, the $4a$

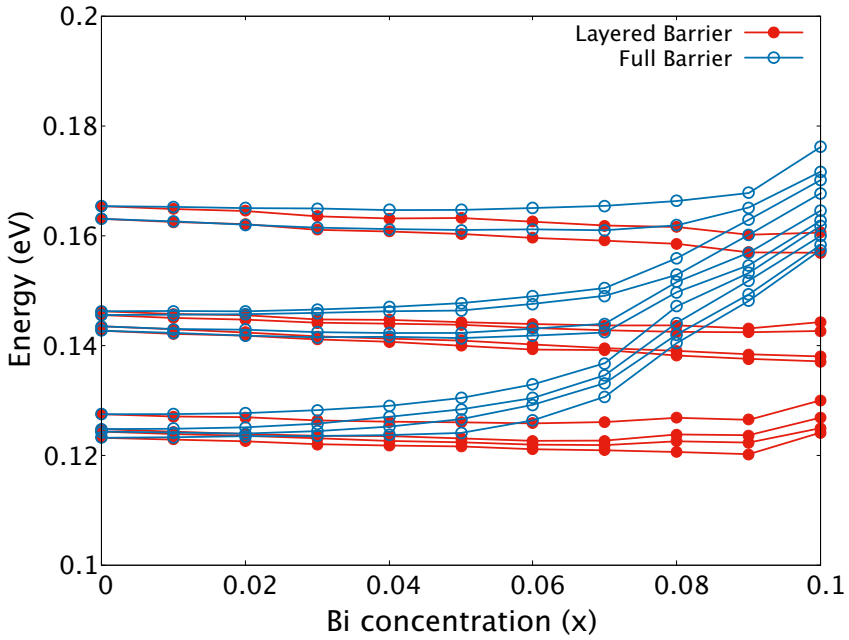

Figure 4.5: Energy levels of an InAs QDM with the interdot region containing a $4a$ layer of $GaBi_xAs_{1-x}$ (red), compared to a QDM where the entire interdot region is $GaBi_xAs_{1-x}$ (blue).

layer of GaBiAs sandwiched between GaAs appies an equal strain to the two dots. We will see shortly that the increased energy difference is a strain induced effect.

4.3.2 Comparison of alloy induced strain and orbital effects

4.3.2.1 Strain effects

To better understand how the Bi in the barrier perturbs the QDM states, we look at strain and orbital effects of Bi alloying independently. First, we consider the strain effects caused by the presence of Bi atoms, as there is an 11% difference in bond length between GaAs and GaBi. By using the strain relaxed positions of the alloyed barrier but using the GaAs TB parameters for GaBi, the effects of strain from Bi are isolated from the effects due to the differences in orbital and hopping energies of GaBi versus GaAs. For a QDM where the full $10a$ inter-dot barrier is alloyed,

calculations are done with and without the InAs dots to show the dot hole states and the underlying GaBiAs valence band (Figure 4.6).

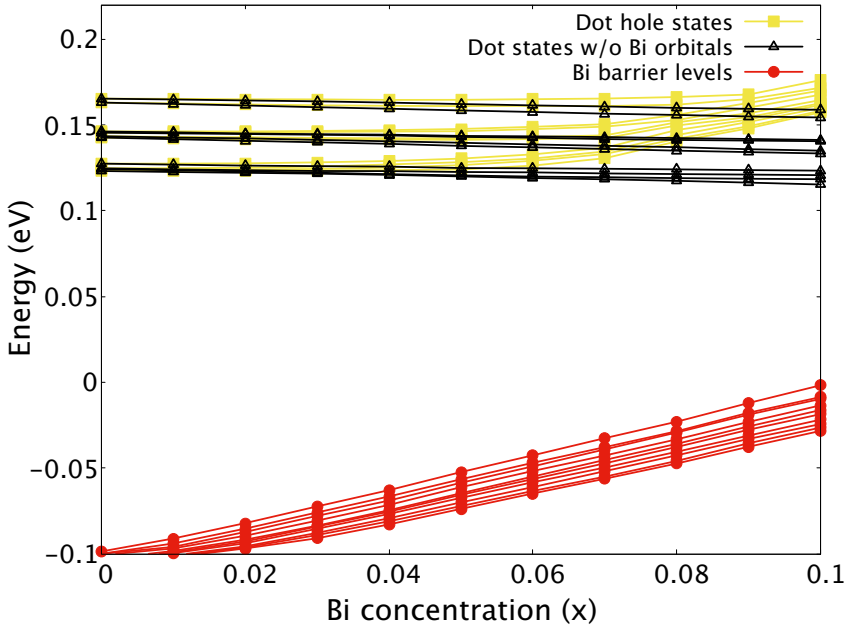

Figure 4.6: Comparison of GaBiAs barrier valence energy levels (red) and InAs dot hole state energy levels (black) with all GaBi tight-binding parameters replaced with those of GaAs, keeping the strain profile for the GaBiAs barrier. Energy levels found with both strain and orbital effects included are shown for comparison (yellow).

In Figure 4.6, we see a near-linear increase in dot hole state energy (i.e., a decrease in valence electron energy) with respect to Bi concentration due to strain. We also see a steady energy shift of the underlying Bi band due to strain alone. One would expect the lowered barrier to lower confinement and decrease the hole state energies. Yet, the significant amount of strain imparted by the alloy onto the dots provides more confinement on the dot hole states, raising their energies. The larger the dot-to-dot separation, the less the barrier height effects the dot energies, and the more the alloy strain is able to raise the hole state energies.

Secondly, there is an increase in energy difference between corresponding top and bottom states as alloy concentration is increases. The effect is present when both alloy

strain and orbital effects are considered, and when only strain effects are applied. We attribute this phenomenon to the difference in strain applied to the top and bottom dots by the alloy. As the alloy fully extends from wetting layer to wetting layer, the alloy surrounding the sides of the bottom dot applies a lateral compressive strain that competes with the vertical compressive strain experienced by both dots. The competition between the lateral and vertical compressive strain results in a overall smaller change in atomic positions for the bottom dot. The top dot, without Bi surrounding its sides, have a larger change in atomic positions from just experiencing the vertical compressive strain. In Figure 4.2 and Figure 4.6, we see that states associated with the top dot (the higher hole state energy of the pair) increase in energy with respect to alloy concentration faster than the states associated with the bottom dot. The result is the alloy increasing the energy separation of the bottom and top dot states. Without an asymmetric strain between the two dots, such as in a layered barrier, this effect is removed and the hole states increase in energy at the same rate.

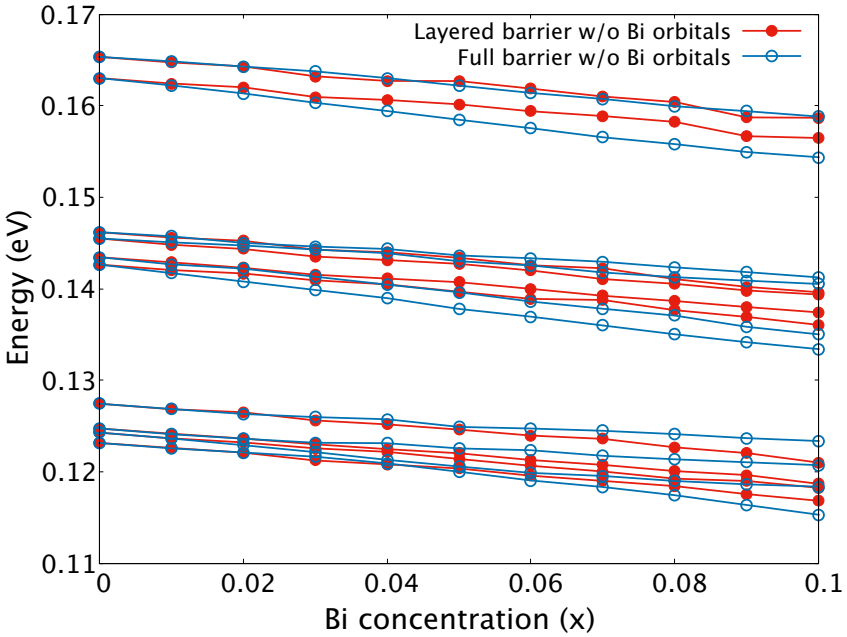

Figure 4.7: Strain dependence of valence energy levels of an InAs QDM, with the interdot region containing a $4a$ layer of $GaBi_xAs_{1-x}$ (red) or the entire interdot region as $GaBi_xAs_{1-x}$ (blue).

Figure 4.7 compares the effect of induced strain for a QDM with a full barrier and a layered barrier. The fully alloyed barrier provides larger energy splitting between top/bottom dot hole state within a given pair. This arises from symmetry breaking between the two dots when the sides of the bottom dot are surrounded by Bi. The similar strain profile in the top and bottom dot for the layered barrier causes energy levels to increase at a similar rate. Both the fully alloyed barrier and the layered barrier show a monotonic increase in dot hole energy due to strain. Neither shows a level repulsion from a Bi band. Slight deviations from a linear dependence show that the strain profile of the system is still sensitive to configurational differences in the alloy, further illustrating the global nature of strain effects on the system.

While it is interesting that strain alone is able to lower the barrier height, the amount of change is not comparable to the change when both strain and orbital effects are considered. Yet, although the underlying Bi band does not overlap with the dot hole states in energy and the Bi is not present where the dot states are spatially, we clearly see that alloy strain has an effect on the QDM hole states. The strain induced by alloying the barrier has a global effect, not confined to just the alloy region but able to affect the energies of the states in the QDMs.

4.3.2.2 Orbital effects

We now look at the effect of the difference between As and Bi orbitals, independent of the strain. To remove the strain induced by the Bi, we relax the structure with the interdot region as GaAs, and use these atomic positions for the GaBiAs barrier. This new lattice contains the GaBiAs interdot barrier, with the corresponding TB on-site and hopping parameters, but uses the "unrelaxed" Bi positions. It is important to note that the system is partially relaxed. The strain caused by the lattice mismatch between InAs and GaAs is preserved, a crucial aspect of InAs QDMs, regardless of

the presence of the alloy. The comparison of the QDM hole states and the Bi band when strain is ignored is shown in Figure 4.8.

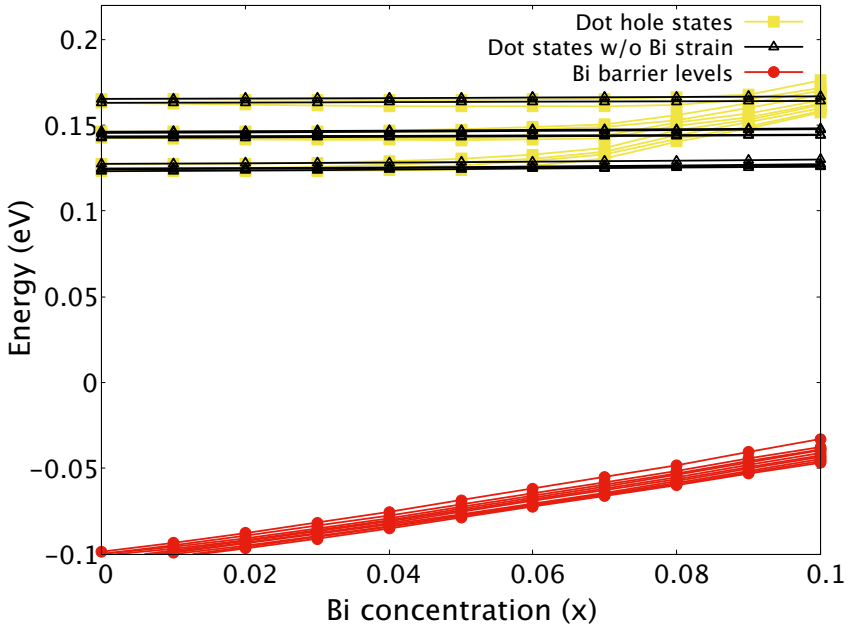

Figure 4.8: Comparison of GaBiAs barrier valence energy levels (red) with InAs dot hole state energy levels (black), using the strain profile of a GaAs barrier, effectively leaving only orbital effects of the Bi alloy. Energy levels found with both strain and orbital effects included are shown for comparison (yellow).

Interestingly, when considering only the orbital effects of Bi, there is no change to the dot hole state energies with respect to Bi concentration. This is the case for both a full GaBiAs barrier and the layered barrier with $4a$ of GaBiAs. These electronic changes brought about by the Bi orbitals are confined to the alloyed region. In contrast, changes brought about by strain are global, affecting the QDs as well as the Bi states.

When both induced strain and orbital effects are included (see Figure 4.2), the barrier GaBiAs VBE is pushed much closer to the dot states than when either the induced strain alone or orbital effect alone is considered. Both the induced strain and orbital effects push the barrier VBE towards the dot states, but it is only when the

combined effect of both is considered that the barrier VBE comes close enough to the QD states for level repulsion to be significant. For small Bi concentrations, x, the effect of induced strain dominates and explains the initial increase of QDM hole state energies. For larger x, the combination of alloy induced strain and Bi orbital effects are needed to explain the reversal of the QDM hole energy shifts under level repulsion.

4.3.3 Spatial geometry of alloy induced strain

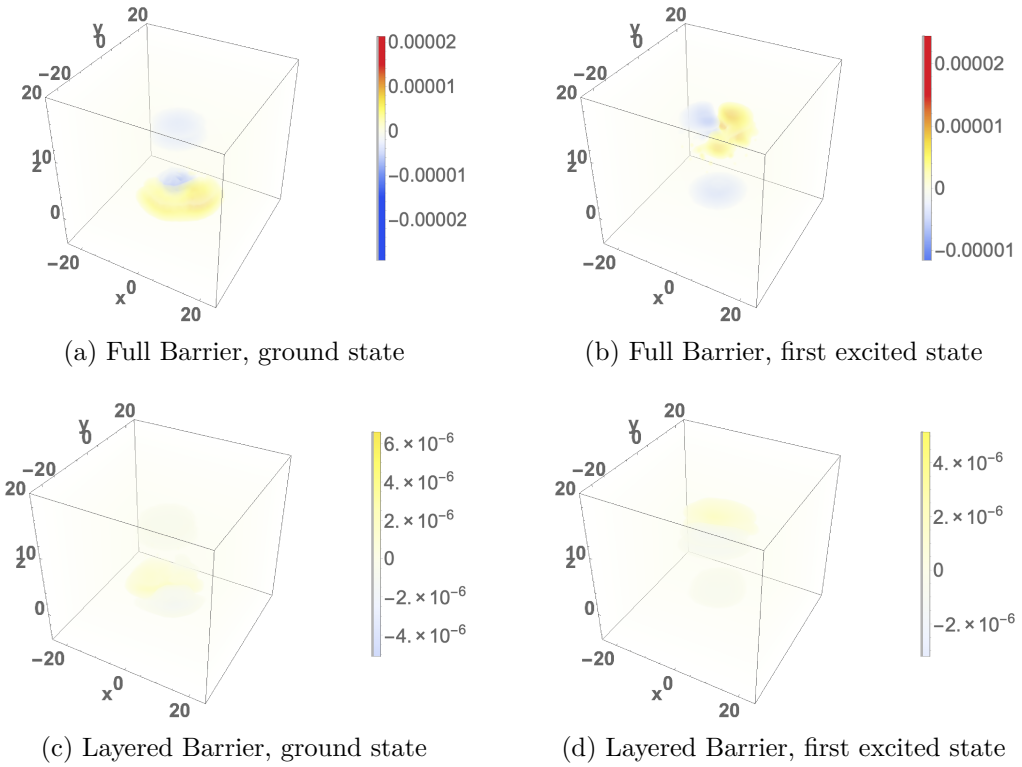

(a) Full Barrier, ground state

(b) Full Barrier, first excited state

(c) Layered Barrier, ground state

(d) Layered Barrier, first excited state

Figure 4.9: Change in QDM hole state charge density when the alloy strain of a 6% $GaBi_xAs_{1-x}$ alloy is applied, for (a) the ground/bottom-dot state and (b) first-excited/top-dot state of a QDM with the entire interdot region as GaBiAs; and for (c) the ground/bottom-dot state and (d) first-excited/top-dot state of a QDM with a $4a$ layer of GaBiAs in the interdot region. Axes labels indicate position in lattice constants; scale bar indicates difference in wavefunction probability before and after strain is included.

Figure 4.9 shows the change in InAs QDM hole state probability (charge density) after alloy strain is introduced (but with orbital differences between Bi and As ignored). The change is calculated as the difference between the 6% alloy case and the 0% alloy case in Figure 4.6. The strain from the alloy further confines the wavefunction to a single dot, and is the reason we see an increase in QDM hole state energy at low concentrations of Bi, for both the full and layered barrier.

Figure 4.10a shows the strain from the alloy region clearly propagating away from the alloy. When the entire interdot region is alloyed, the Bi surrounds the bottom dot, and the strain is concentrated outside of the bottom dot near the sidewalls. The top dot, on the other hand, has the strain accumulating uniformly beneath the wetting layer and propagating through the dot. Therefore, the top dot receives much more of the alloy induced strain, whereas the bottom dot has strain surrounding it but not penetrating the dot itself. The result is increased difference between the bottom (ground) and top (first excited) state energies seen in Figure 4.7.

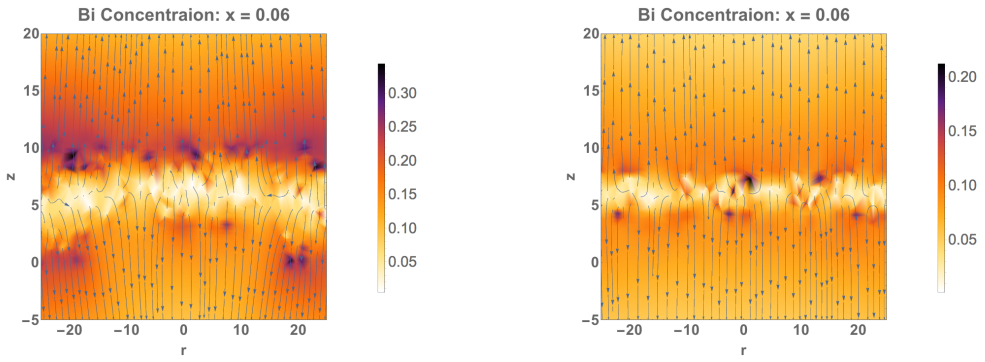

(a) Full GaBiAs Barrier (b) Partial GaBiAs Barrier

Figure 4.10: Shift in atomic position resulting from alloy strain for an InAs/GaBiAs QDM with (a) the entire interdot region as $GaBi_{0.06}As_{0.94}$ or (b) the interdot region containing a $4a$ layer of $GaBi_{0.06}As_{0.94}$. Arrows represent the direction of position shift. Backdrop represents magnitude of shift; scale bar in units of Å. 2D slice taken along 110-plane (distance in lattice constants a).

For a symmetrically layered interdot barrier, with a $4a$ layer of GaBiAs sandwiched between GaAs, the strain is able to propagate above and below the alloy region equally (see Figure 4.10b). The alloy induced strain is able to affect both dots in a fashion similar to how the top dot was affected in the full barrier case. However, due to the distance between the alloy layer and the dots, the strain is diminished by the time it reaches the dot, resulting in less of an energy shift in comparison with the top dot in the full barrier case in Figure 4.7.

4.3.4 Dot-to-dot separation

In addition to varying the thickness of the alloy layer in the barrier, we can also vary the distance between the dots. We have previously shown that the raising of the dot hole state energies caused by alloy strain is a much stronger effect than the decrease in energy induced by lowering the barrier, until higher alloy concentrations where band repulsion dominates.

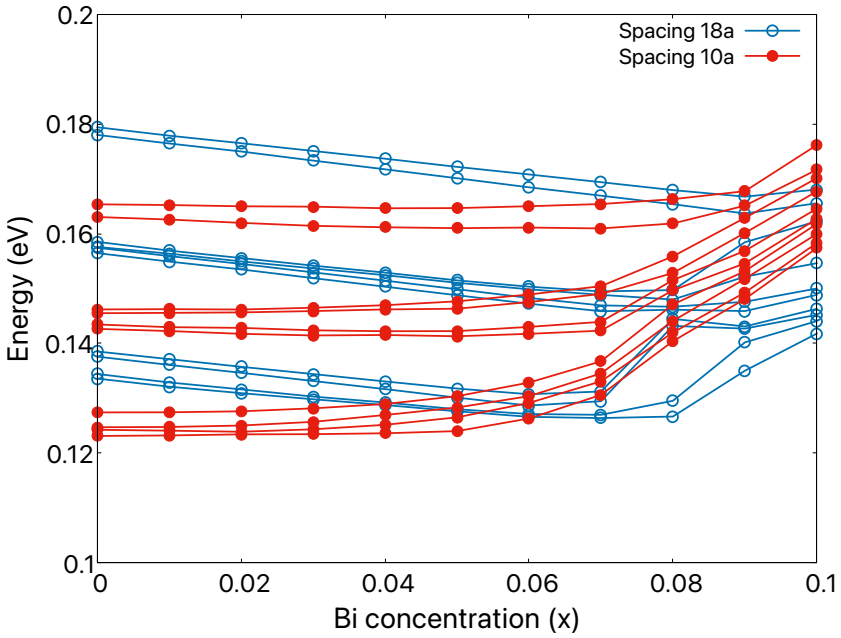

Figure 4.11: QDM valence energies with the a $10a$ layer of $GaBi_xAs_{1-x}$, for a dot-to-dot separation, defined as wetting layer to wetting layer distance, of $10a$ (red) and $18a$ (blue).

In an extreme example (Figure 4.11), we keep the $10a$ layer of $GaBi_xAs_{1-x}$ we had previously for the fully alloyed barrier, but increase the dot-to-dot (wetting layer to wetting layer) distance to $18a$. The barrier material for the new space between the dots is filled in with GaAs, creating a layered barrier consisting of a $4a$ layer for GaAs (not including the space occupied by the bottom dot), a $10a$ layer of GaBiAs, and a $4a$ layer of GaAs. In comparison to the previous dot separation of $10a$, the $18a$ separation results in the dot states being less sensitive to the change in barrier height cause by the alloy. The alloy strain, however, is able to affect the structure globally, and thus we see a drastic increase in hole states energy as the alloy concentration is increased.

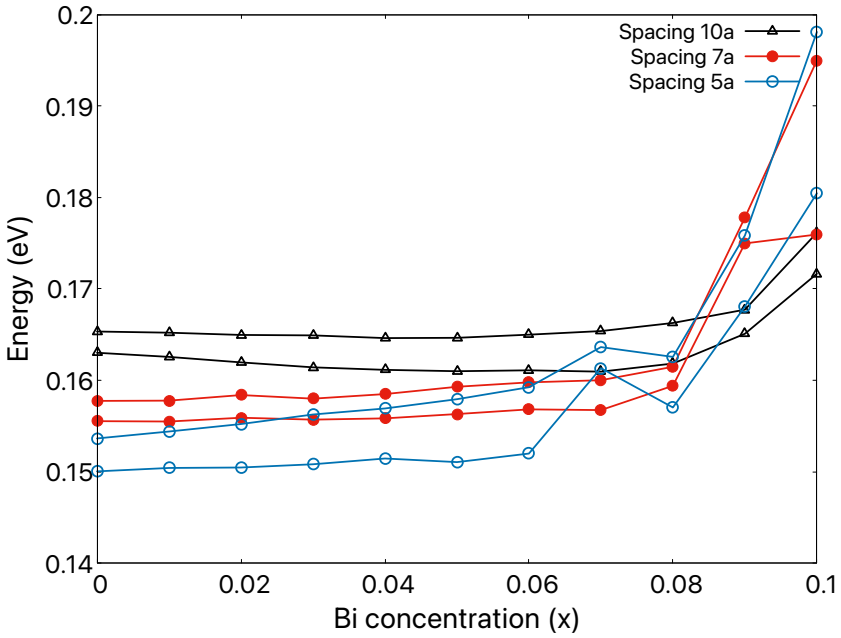

Figure 4.12: QDM valence energies, all with fully alloyed barrier regions, with varying dot separations.

If we were to decrease the dot-to-dot separation instead, the dot hole states become more sensitive to the barrier height. Figure 4.12 shows the dot hole states for QDMs with progressively closer dots. For all separations, the entire barrier region is GaBiAs. For dots separations greater than $7a$, including previously shown QDMs with layered barriers, the alloy strain raises the hole state energies. A dot separation of $7a$ shows a

transition point, below which the hole state energies decease with alloy concentration. The smaller dot separation not only results in the dot state being more sensitive to the barrier height, the state are also closer in energy to the barrier VBE, resulting in an earlier and stronger onset of band repulsion with respect to alloy concentration.

Chapter 5: Coherent tunneling of hole states QDMs

This chapter includes material from a paper that is currently under review with Physical Review B, a preprint of which can be found at arXiv:2309.10115

In the previous chapter, we studied the energies of hole states in QDMs with $GaBi_xAs_{1-x}$ barriers at zero applied electric field (i.e. away from resonant coupling). In this chapter, we study the hole states as a function of applied constant transverse electric field (along the growth axis), which tunes the hole states of the two QDs through energetic resonance. We show that a maximum three-fold increase of tunnel coupling is achieved via alloying. Additionally, we have a discussion on local potentials created in the barrier region by the random nature of the alloy distribution, resulting in the creation of states localized in the barrier region. We analyze the separate contributions of the additional strain and the orbital fluctuations introduced by the alloying. We show that the strain introduced by alloying can shift the field strength required to achieve resonance by applying additional asymmetry to the system. However, when applied in isolation without the orbital effects of the alloy, the alloy strain does not affect the intrinsic tunneling behavior of the hole states. Orbital changes introduced by the alloying, on the other hand, do not affect the location of the resonance and better show the increased tunnel coupling from lowering the barrier energy. Importantly, the combination of alloy strain and orbital effects lower the barrier height significantly more than either effect individually, which results in the significant increase in tunnel coupling strength. Finally, we have a brief

discussion on the optimization of alloy effects by varying the dot-to-dot separation. We find a $10a$ dot-to-dot separation to be optimal for alloy enhancement of tunnel coupling, and present evidence that the alloy induced change in tunnel coupling may affect the heavy-hole and light-hole components governing the formation of a symmetric or anti-symmetric ground state.

5.1 Electrical tuning of hole states

Away from resonance (Figure 5.1b and Figure 5.1c), the hole states are well confined to their respective dots. The zero-field energy of the dot states are different for the two dots due to the slight difference in strain caused by the placement of the wetting layer, breaking mirror symmetry. The tunnel coupling strength between the states of opposing dots can be characterized by the hybridization of the states when the dots are brought into energetic resonance (Figure 5.1a). We investigate the coupling strength by looking at the behavior of the hole state energies as the holes are brought into resonance by a uniform electric field applied along the stacking axis of the two QDs [10, 17]. The interaction between the states hybridizes the states to form symmetric and anti-symmetric pairs, i.e., molecular states. The anti-crossing energy between the symmetric and anti-symmetric pair at resonance is representative of the strength of the tunnel coupling between the dots.

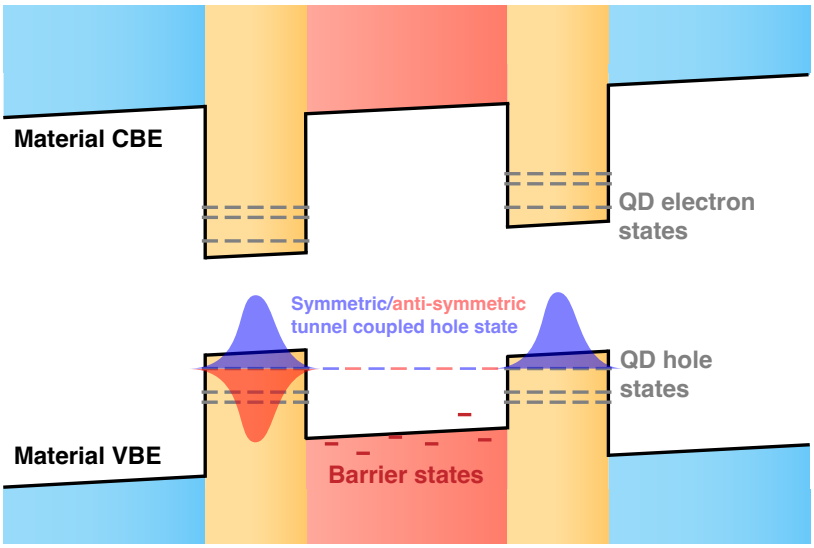

(a) Dots electrically tuned to resonance

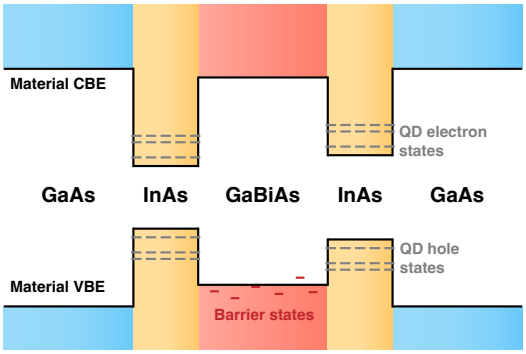

(b) Zero electrical bias

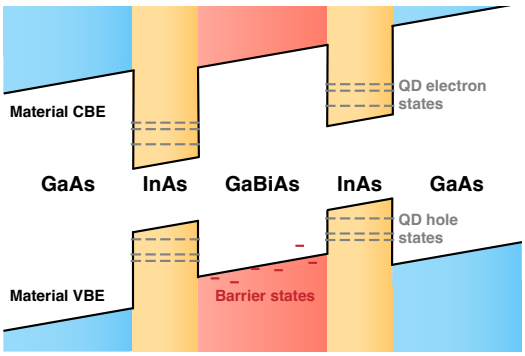

(c) Electrical bias applied past resonance

Figure 5.1: A cartoon representation of the band diagram of InAs/GaBiAs QDMs being electrically tuned with a field in the stacking direction of the dots. (a) At resonance, hole states tunnel couple across the two dots to from symmetric and anti-symmetric molecular states. (b) At zero electrical bias, the hole states are well separated, energetically, by the difference in strain experienced by each dot. (c) Tuned past resonance, higher energy hole states and states localized to the alloyed barrier region, can be brought to the same energy region as the ground state of the lower dot.

The introduction of GaBiAs in place of GaAs enhances the tunnel coupling in two distinct ways. First, raising the valence band energy (lowering the energy barrier) of the barrier material weakens the tunnel barrier and promotes dot-to-dot tunnel coupling [36]. Second, Bi atoms are larger than As. Introducing Bi to the GaAs barrier introduces additional strain into the system. If the amount of strain applied to the two dots by the alloy is not equivalent, the hole state energies of the two dot are shifted by different amounts, changing the potential bias at which resonance occurs. Yet, when the alloy strain is applied without the orbital effects of the alloy, the strength of the tunnel coupling between the dots at resonance remains unaffected.

The random distribution of Bi atoms also creates pockets of local potential in the barrier, resulting in the presence of hole states with charge densities localized around a few atoms in the barrier. At lower alloy concentrations, these states remain energetically separated from the well behaved dot states. However, at higher alloy concentrations, the barrier VBE and these localized states in the barrier are brought into, or even above, the valence energy region of the dot states. At a threshold concentration, these barrier states can be tuned in and out energetic resonance with the dot states with an electric field (Figure 5.1c). Generally, the barrier states only very weakly couple to the dot states, but the strength of coupling is very dependent on the strength of the local potential and how close, spatially, the barrier state is localized with respect to the dot.

5.2 Alloy concentration

Figure 5.2 shows the energy levels of the hole states in response to an electric field applied along the growth axis. The hole state energies are shown as the energy of the corresponding valence states, such that the lowest energy hole state is at the top of the band of valence states. We have set the potential to be zero at the bottom of lower

dot, so that the energies of the bottom dot states remain unchanged when the field is applied, while the energies of states mostly localized to the top dot increase linearly with the field strength and dot separation. The state with the lowest hole energy for each of the two dots, including the hybrid states they form, are colored black; higher energy states are colored blue; states that have a significant wavefunction density in the barrier region between the dots are colored red.

The states of most interest are the ground state and the first excited state, or the lowest energy hole state for each of the dots (black in Figure 5.2). Looking at the energy difference between the ground and excited states at each electric field strength, the minimum energy difference defines the location and strength of the anticrossing. The larger the anticrossing energy, the stronger the coupling between the two states, making it easier to tunnel from one dot to the other. Up to 6 % Bi, we see a steady increase of anticrossing energy between the two lowest energy hole state of the respective top and bottom dots. We also see that the resonance occurs at progressively larger field strengths. The change in resonance location is not due to the tunneling behavior. Rather, the shift results from the increasing initial (zero-field) difference between the ground and first excited states that is due to the increased strain on the top dot introduced by the alloy [36]. The presence of Bi surrounding the bottom dot adds to the asymmetry of the QDM, causing the larger energy difference between the top and bottom dot states. The larger initial difference between the states in the top and bottom dots does not result in a larger anticrossing energy, just an increase in the field strength needed to bring the states into resonance. The increase in anticrossing energy results from the stronger tunnel coupling between the two dots, regardless of where the zero-field energies lie relative to each other.

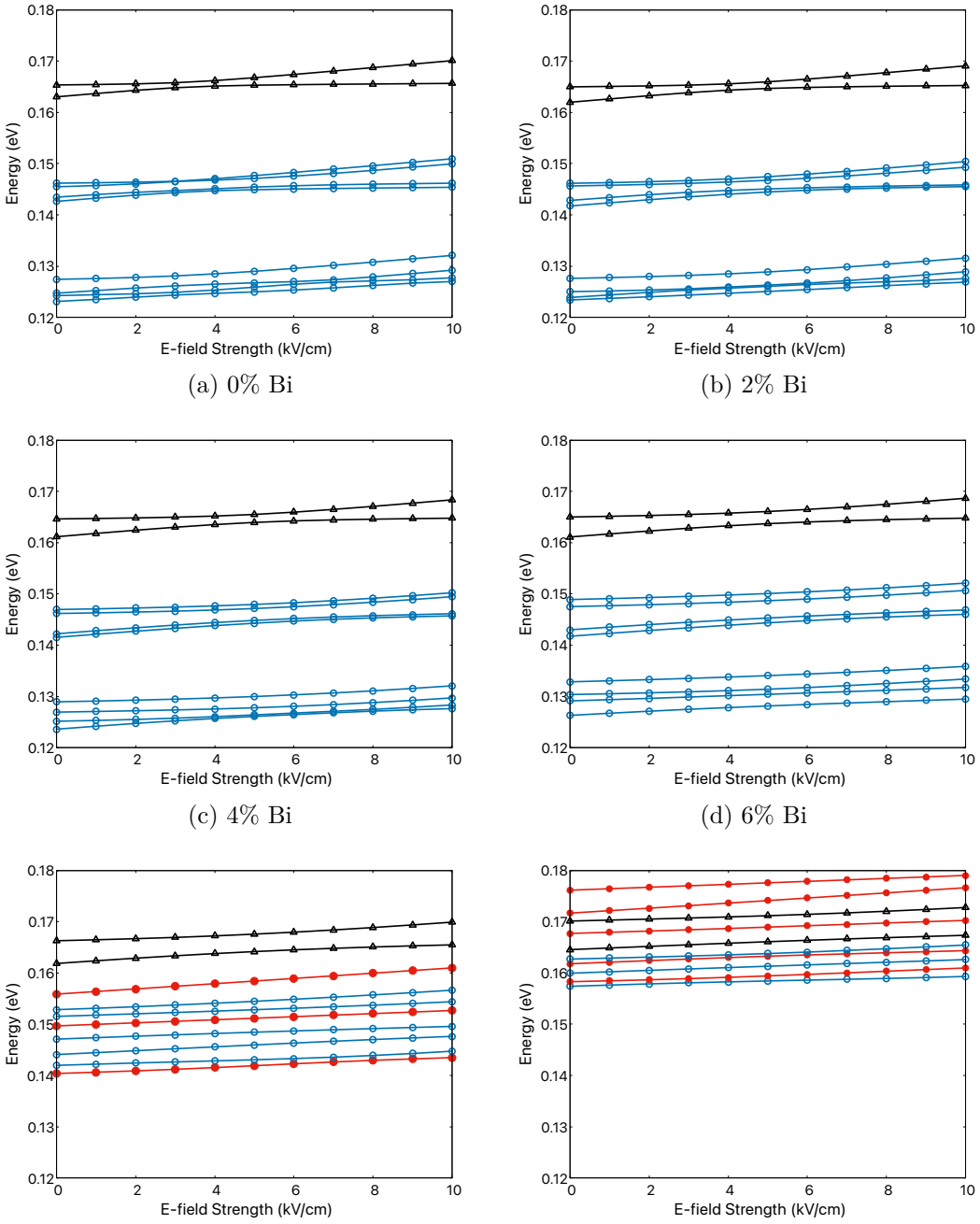

(a) 0% Bi (b) 2% Bi

(c) 4% Bi (d) 6% Bi

(e) 8 % (f) 10 %

Figure 5.2: Energy levels of an InAs QDM with a $GaBi_xAs_{1-x}$ full barrier, where (a) $x = 0.00$, (b) $x = 0.02$, (c) $x = 0.04$, (d) $x = 0.06$, (e)$x = 0.08$, and (f) $x = 0.10$. An electric field of up to $10\,\mathrm{kV\,cm^{-1}}$ is applied along the lattice growth axis. Black: the lowest energy hole state confined to either dot, and the molecular states they form. Blue: higher energy hole states that are still well confined to the dots. Red: states with charge densities highly localized to the barrier region.

As the barrier $GaBi_xAs_{1-x}$ band edge approaches the energy range of the dot levels, the dot states lose confinement and leak into the barrier. As a consequence, starting at around 8% Bi, where the GaBiAs barrier has similar valence band energies to the InAs dots, we see a loss in well-defined resonance behavior for the dot states (Figures 5.2e and 5.2f). This is confirmed by spatial plots of the wavefunctions (not shown), where an increasing proportion of the charge density of the states is in the GaBiAs barrier, peaking at local clusters of Bi atoms. At 8% Bi, not only is a large part of the wavefunction in the barrier, but the wavefunctions also start losing the modal structure of dot confinement. At 10% Bi, the wavefunctions are almost entirely in the barrier, localized around few-atom Bi clusters, resulting in states strongly dependent on the alloy configuration. In addition to what the wavefunction plots display, the leakage of charge into the barrier and the configurational variances of the alloy can also be seen by applying higher electrical biases, as we shall discuss in the next section.

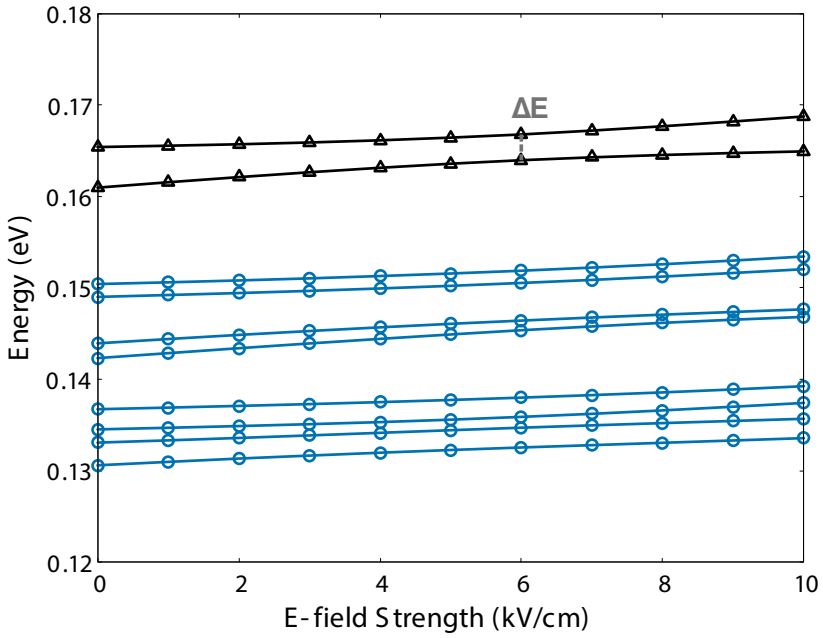

Figure 5.3: Energy levels of an InAs QDM with a $GaBi_{0.07}As_{0.93}$, under an electric field up to $10\,\mathrm{kV\,cm^{-1}}$ along the lattice growth axis.

For the geometry of the dots given, we have found 7% alloy to be the optimal concentration for tunnel coupling enhancement. Figure 5.3 shows the results for a QMD with a $GaBi_{0.07}As_{0.93}$ inter-dot barrier. A threefold increase in anticrossing energy from the non-alloyed case occurs. A 7% Bi alloy was the highest concentration we found where all the states were well confined in the dot. While higher alloy concentrations can have larger anti-crossing energies, the states tend to lose their dot like characteristics. Controlled amount of leakage into the barrier can be beneficial in increasing the anticrossing energy and creating a more strongly coupled molecular state. However, the large amount of confinement loss at 8% and higher alloy concentrations leads to poorly behaved states that are more sensitive to the alloy disorder.

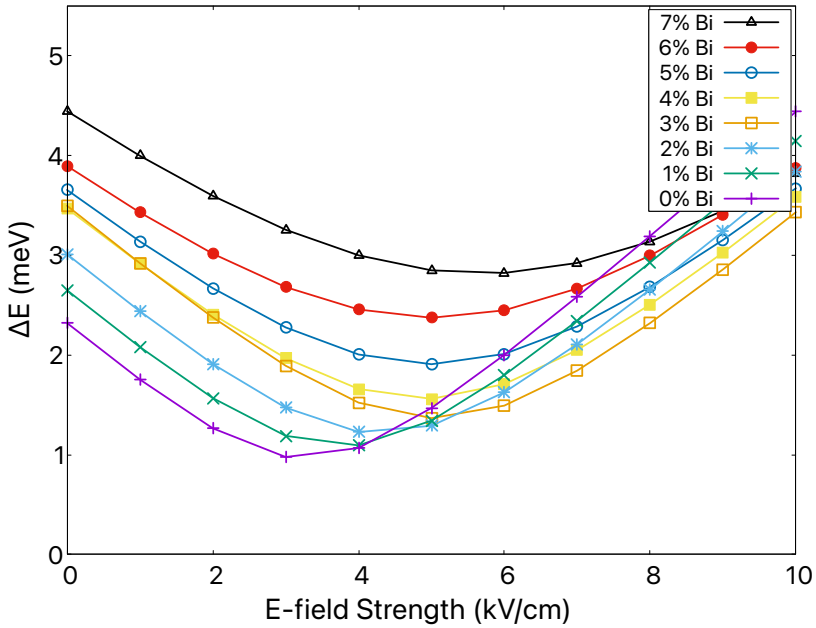

Figure 5.4: Energy difference between the top two valence states of a InAs QDM with a full $GaBi_xAs_{1-x}$ inter-dot barrier, obtained from a random alloy model.

Figure 5.4 shows the energy splitting between two lowest energy hole states as a function of the applied field for concentrations up to 7%. These two states represent the lowest energy state for the bottom dot and the top dot, or, in the case

of resonance, the symmetric and anti-symmetric between the two dots. The minimum energy difference occurs at tunnel resonance. The magnitude of the difference at resonance is the anti-crossing energy and indicates the strength of the tunnel coupling. From Figure 5.4, the resonance shift to higher electrical bias as alloy concentration increases is clear. Moreover, as the alloy concentration increases, we see the increase in anticrossing energy, increasing three-fold between a non-alloyed barrier and a 7% alloy composition.

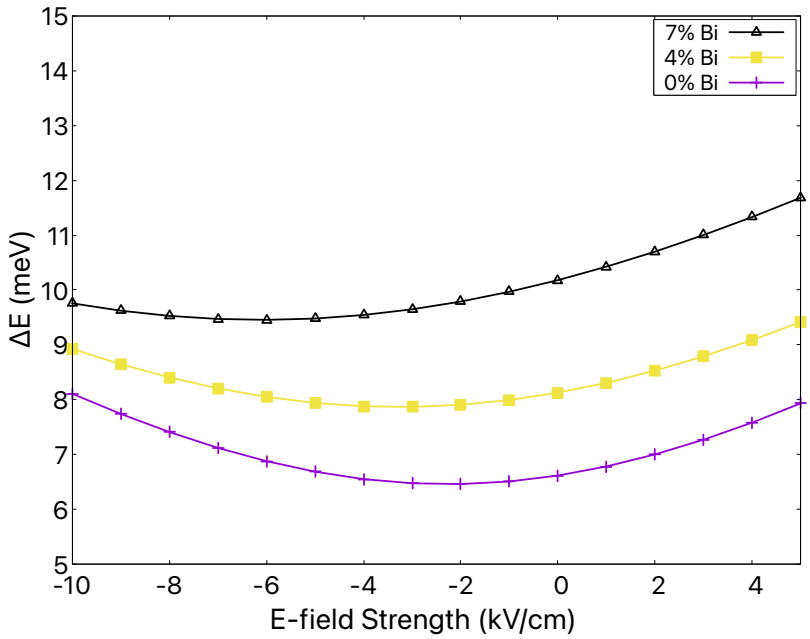

Figure 5.5: Energy difference between the bottom two electron states of a InAs QDM with a full $GaBi_xAs_{1-x}$ inter-dot barrier, obtained from a random alloy model.

In addition to the hole states, we shall briefly discuss the effects of the GaBiAs barrier on the electron states of the QDM. In Section 4.1, we saw that the alloy had a very weak to little effect on the energy of the dot electron states. However, we have also shown in Section 3.2 that the CBE for the GaBiAs does decease with alloy concentration. This does promote the coherent tunneling of electrons between the two dots of the QDM. As seen in Figure 5.5, we have about a 50% increase in electron anti-crossing energy from 6.5 meV without alloying to 9.5 meV at 7% alloy. The electrons are also

biased in the opposite direction of holes, requiring a negative electric field, or a field going from the top dot to the bottom dot, in order to bring the states to resonance.

More importantly to note for electrons is the much wider resonance and the overall higher anti-crossing energy of electrons in comparison to holes. In our QDMs, the electron charge densities are already well spread out between the two dots. This is due to the lower effective mass of the electron in comparison to holes, and is consistent with how these systems ought to behave. The delocalized nature of the electrons allows for exciton transitions with hole states of either dot, and is crucial in the utilization of the spin-mixed trion states for qubit rotation.

5.3 Alloy configuration

5.3.1 Random distribution of alloy and localized barrier states

Previously, we found that different Bi alloy configurations in the $GaBi_{0.07}As_{0.93}$ barrier can have valence band edges that differ by approximately 50 meV [36]. We also saw in the previous section that we lose well-defined dot energy levels and resonance behavior when the VBE of these Bi states overlap the energy levels of the InAs QDM hole states. Here, we discuss what happens to resonant behavior if a few Bi states are pushed into the dot energy levels by the alloy configuration.

Figure 5.6 shows the hole states of a QDM without an alloyed barrier, with an external electric field up to $100\,\mathrm{kV\,cm^{-1}}$ applied in the lattice growth direction. In Figure 5.6, states localized in the bottom dot can be easily identified by the lack of electric field dependence, as we have set the potential to be zero at the wetting layer of the bottom dot; states localized to the top dot can also be clearly identified by the constant slope of their energies versus field strength. The electric potential at

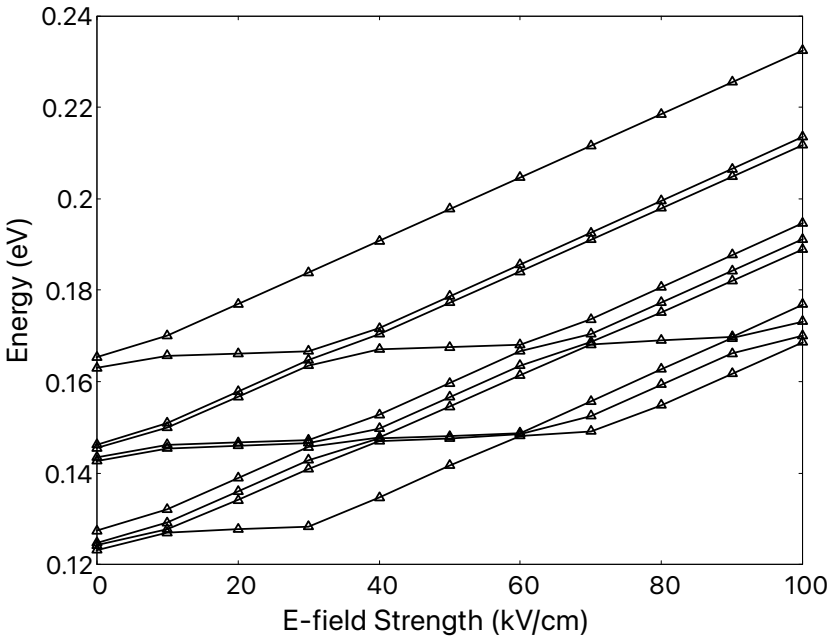

Figure 5.6: Energy levels of an InAs QDM without alloy. An electric field of up to $100\,\mathrm{kV\,cm^{-1}}$ is applied, showing one slope for hole states in the top dot and a close to flat slope for states in the bottom dot.

the top dot has a linear increase with field strength, resulting in a linear increase in valance energy for states of the top dot.

Figure 5.7 shows two realizations of a QDM with 7% Bi in the barrier region. Figure 5.7a shows the same states and alloy distribution as Figure 5.3, but up to a higher electric field strength. The alloy distribution for Figure 5.7b was selected based on our previous finding that the specific barrier levels of this alloy distribution has a large gap between the highest hole state and the next highest hole state (see Chapter 4). This gives us a barrier state close in energy to the dot states and allows us to present a picture without too many barrier states to monitor.

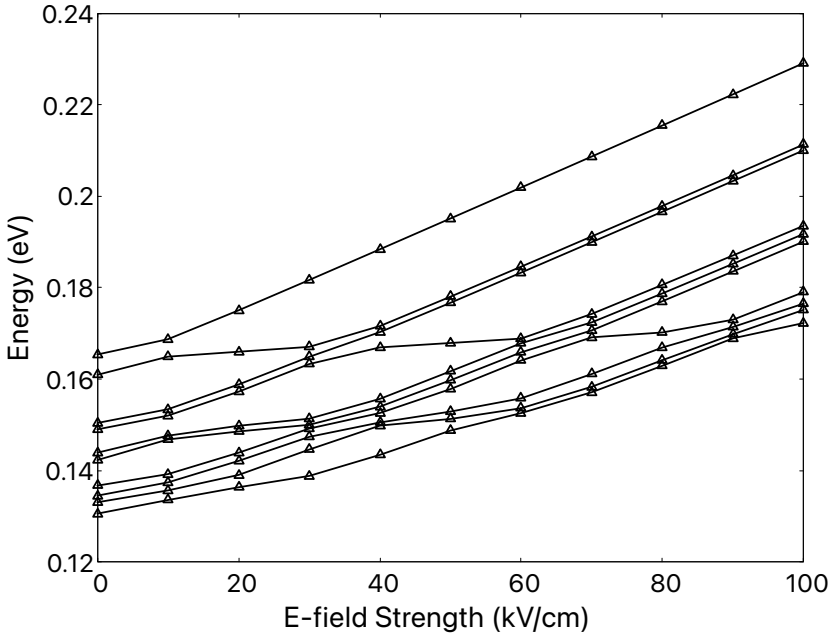

(a) Alloy distribution #1

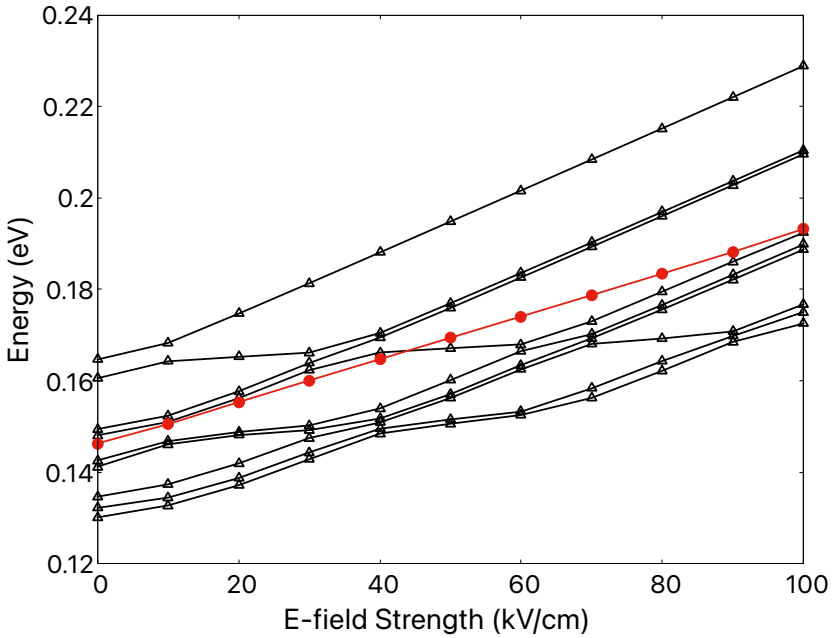

(b) Alloy distribution #9

Figure 5.7: Energy levels of an InAs QDM with $GaBi_{0.07}As_{0.93}$ full barrier. (a) Distribution #1 shows an alloy distribution where the lowest 20 holes states are all confined in the InAs dots. (b) In contrast, distribution #9 shows a state with its slope in between the dot states that does not anti-cross with the dot states (red), indicating a hole state that is well localized within the barrier region.

For Figure 5.7, different random seeds were chosen to create different random distributions of the alloy, and only the 20 lowest energy hole states are plotted (each two-fold degenerate for 10 unique energies). In both cases, we can still clearly identify states of the bottom and top dot by their slopes. Aside from larger anti-crossing energies, Figure 5.7a is qualitatively similar to the case without alloy (Figure 5.6), showing the same energy structure expected of hole states confined to quantum dots. However, in Figure 5.7b, there is an additional state present (colored red). The rate of change for the energy of this state with respect to the electric field is in between that of the bottom and top dot states, indicating a charge distribution located between the dots, i.e. the barrier. This is confirmed with charge density plots showing a hole state highly localized to a pocket of Bi atoms in the barrier.

Due to the highly localized nature of this state in the barrier, there is very little wavefunction overlap between this state and the dot states, resulting in no detectable anti-crossing between the barrier state and the dots states at the scale we have plotted. Other realizations of the alloy distribution with identifiable states localized in the barrier also show very weak coupling to the dot states. The higher in energy the barrier state, or if the state is spatially localized closer to the dots, the more wavefunction overlap we see between the barrier and dot states. In total, of the 41 alloy configurations of 7% Bi studied, we found 4 cases where we could identify a state localized to the barrier within the first 20 hole states.

Having additional barrier states mixing with dot states complicates interaction between the two dots. However, the presence of these barrier states does not alter the energy structure of the dots, for the 7% concentration we have shown. We still see clear top-bottom dot pairs and a ladder of excited states, unlike for higher concentrations of Bi where there is a breakdown of well-defined dot states. Furthermore, for the states of interest (the two lowest energy states, one for each dot), the field strength

at which resonance occurs can differ, but the anticrossing energy is not sensitive to configurational differences in the alloy. For low concentrations, alloy concentration and barrier layer thickness are the dominant effects, while configurational variations have little effect on the strongly confined ground and first excited states.

5.3.2 Ordered and clustered distributions of alloy

In addition to the random distribution of Bi in the alloy, we also studied the case of alloys with an ordered placement of the Bi atoms and a weighted placement of Bi atoms. In the ordered case, a Bi atom is placed every 2 lattice constants, such that one Bi atom per 8 unit cells gives us an alloy concentration of 3%. If another set of Bi atoms is placed offset by $1a$ in all three lattice directions, resulting in two Bi atoms per 8 unit cells, we have a pseudo-periodic lattice of 6% alloy. For a clustered alloy, the placement of Bi is performed in two steps. An initial placement of half the desired concentration is placed randomly with a pseudo-random number generator. A second sweep of the lattice is then performed, where each As atom would have a 10% increase in chance to be replaced with a Bi atom for each next nearest neighbor replaced with Bi in the first round. The overall probability of the second round is normalized such that half the desired concentration of Bi is placed, resulting in the overall concentration after the two round to equal the initially desired concentration.

Figure 5.8 shows the anti-crossing of the two lowest energy hole states of a QDM with either an ordered or clustered GaBiAs alloy as the inter-dot barrier; both are compared with the results of the random alloy distribution seen in Figure 5.4. At lower alloy concentrations, both the ordered and clustered cases are similar to the randomly distributed case. At higher concentrations, the ordered alloy has a much smaller enhancement to the tunneling compared to the random alloy. Starting at 4% (not shown), the clustered alloy shows a greater shift in the field strength needed to

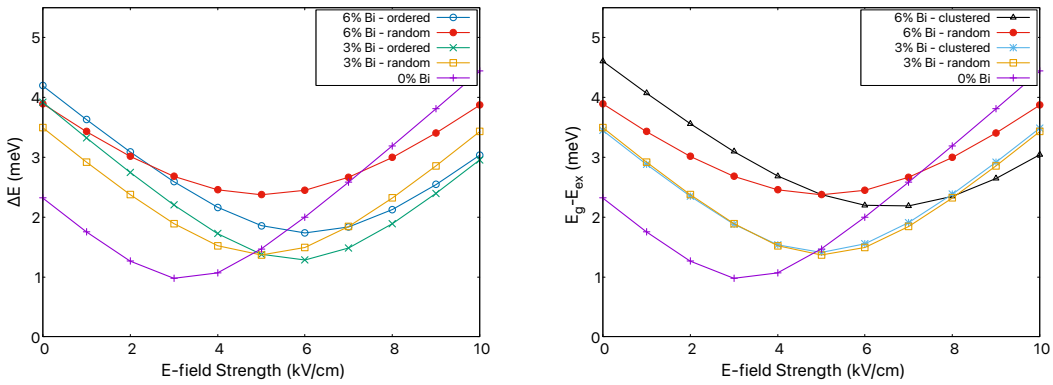

(a) Ordered alloy.

(b) Clustered alloy

Figure 5.8: Energy difference between the top two valence states of a InAs QDM with a full $GaBi_xAs_{1-x}$ inter-dot barrier consisting of (a) a semi-periodic placement of Bi or (b) a weighted distribution of Bi, both compared to the pseudo-random distribution of Bi.

bring the two dots to resonance when compared to the random alloy. However, the enhancement to the tunnel coupling strength remains similar and within what would be expected provided the randomness in the placement of Bi atoms.

The lack of enhanced tunneling for the ordered alloy does not present much of a concern, as naturally grown GaBiAs will not be in an ordered structure. On the other hand, Bi atoms do have a tendency to cluster together when grown in GaBiAs. However, we do not find the tunnel coupling enhancement of the alloy to be significantly impacted by such an effect.

5.4 Alloy strain and effects of system geometry

5.4.1 Comparison of strain and orbital effects on resonant behavior

Previously, we determined that strain effects from the $GaBi_xAs_{1-x}$ layer shift the zero-field energy levels proportional to the concentration of Bi, and, more importantly, strain effects cause an increase in the energy difference between top and bottom dot states [36]. To isolate the effects of strain, we did three calculations: a calculation

including the modified strain due to alloying but ignoring the orbital changes at each site, a calculation accounting for the Bi orbitals but ignoring the additional strain from alloying, and the full calculation with both the orbital and strain effect of the alloy.

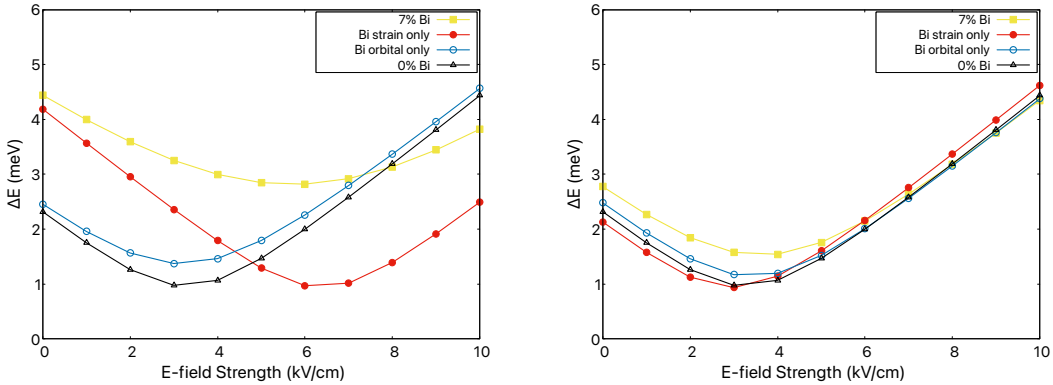

(a) Full GaBiAs layer.

(b) $4a$ GaBiAs layer.

Figure 5.9: Energy difference of the top two valence states under an electric field, resulting from pure GaAs barrier (black), unstrained $GaBi_{0.07}As_{0.93}$ barrier (blue), GaAs barrier with GaBiAs strain profile (red), and strained $GaBi_{0.07}As_{0.93}$ barrier (yellow).

We isolate the effects due to the modified strain and the orbital differences between Bi and As for an alloyed barrier with 7% Bi. The energy difference with respect to electric field for the top two states for both the full $10a$ GaBiAs barrier (Figure 2.1a) and the $4a$ GaBiAs layer within the larger inter-dot region (Figure 2.1b) are shown in Figure 5.9. For the QDM with a layered barrier, the anti-crossing splitting between the ground and first excited states is more than for the QDM with the pure GaAs barrier, albeit still less than for a QDM with a full GaBiAs barrier (roughly a 1.5 increase instead of the three-fold increase for the full barrier). This is due to an overall lower alloy content if one were to average the alloy concentration across the alloy and non-alloy layers of the barrier. However, since the GaBiAs region is symmetric in regards to the layer geometry and does not wrap around the bottom dot, no additional asymmetry in strain is imposed on the system. The preserved symmetry between the top/bottom dot geometry results in a smaller zero-field energy difference between the

ground and first excited state, leading to less of a shift in the field strength needed to bring the states into resonance compared to the full barrier case.

As we have shown previously, the orbital effect of the alloy does not greatly impact the hole states energies inside the dot. The alloy does lower the barrier energy, thus enhancing the tunnel coupling. As the orbital effects are primarily in the barrier and not the dots, we do not see a differing effect between the top and bottom dots. This also implies that orbital effects are not geometry dependent, as shown by the similar results between the full and layered barrier (after accounting for average concentration differences).

In contrast, the strain introduced by the alloy can have a weaker effect exclusively on the bottom dot hole state if the alloy extends to surround the bottom dot. In both the full and layered barrier, the bottom dot hole state energy is increased (valence energy is decreased) by roughly 5 meV at zero electric field, despite the layered barrier having a lower average alloy concentration across the full barrier. The top dot energy, on the other hand, is increased by 7 meV in the full barrier and 5 meV in the layered barrier, consistent with the higher overall alloy concentration of the fully alloyed barrier. Since GaBi has a longer bond-length than GaAs, the expansion of the inter-dot barrier translates to an additional compressive strain applied to the dots. For the QDM with a layered barrier, this strain modification is applied similarly to the top and bottom dots. However, when the full barrier is alloyed, the modified barrier wraps around the bottom dot, covering both its top and side faces. The competition of the alloy compressing the bottom dot vertically and laterally results in the strain concentrated around the corner of the dot, not penetrating the interior of the dot. This reduces the effect of the strain added to the bottom dot, resulting in a larger zero-field energy difference between the top and bottom dot, moving the resonance to a higher electrical bias.

The strain increases the hole states energies in the dots, while the orbital effects of Bi do not directly affect the dot energies. Therefore, strain alone is able to shift the amount of electrical bias required to achieve resonance. However, alloy strain alone does not lower the barrier enough to affect the tunneling strength between the two dots. The effect of the lower tunnel barrier is more strongly observed in the case where only orbital effects are considered. Moreover, the combination of the two effects results in a much stronger change in barrier energy and a drastically stronger increase in tunneling coupling strength.

5.4.2 Dot-to-dot separation

Finally, in addition to varying the thickness of the alloy layer between the dots, we can also change the thickness of the barrier between the two dots. Figure 5.10 shows the tunnel coupling strength represented by the anti-crossing energy for different dot-to-dot separation with respect to alloy concentration. The geometry of each individual dot and their wetting layer remains the same, but the distance between the two dot is changed, resulting in a varied barrier thickness. The barrier thickness, denoted in the plot legend, is defined as the distance between the top of the bottom wetting layer and the bottom of the top wetting layer.

Separations of $5a$ have similar relative enhancement to the tunnel coupling by inclusion of Bi when compared to separations of $10a$. However, due to the dots being in such close proximity, tunneling between the dots is much stronger than any other dot separation we tested. The utility of dots with spacing so close remains an open question. On the other hand, dot separations of $13a$ and $18a$ can achieve higher relative enhancement to the tunnel coupling, but still have a weaker overall tunnel coupling strength compared to the $10a$ separation. Smaller dot separations also result in faster delocalization for the dot states with respect to alloy concentration, hence

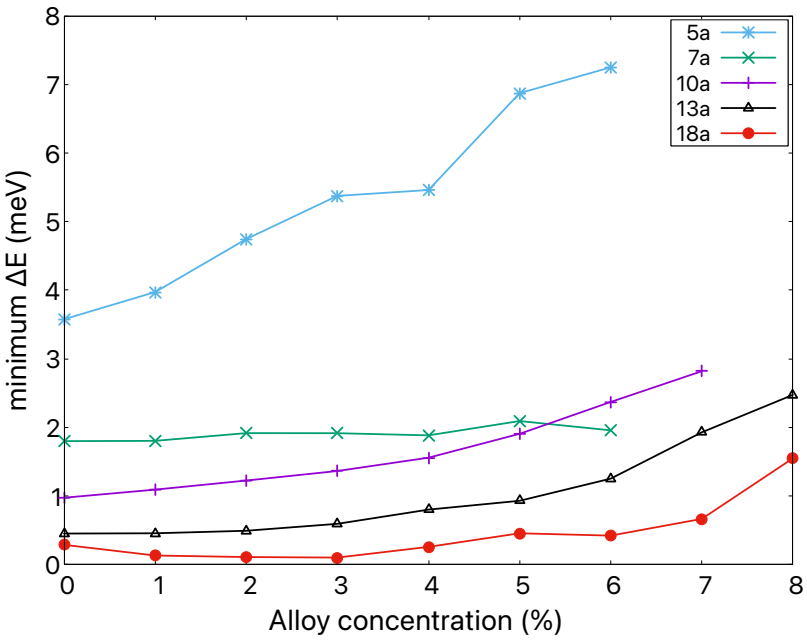

Figure 5.10: The anti-crossing energy (taken as the minimum energy difference between the top two valence states) of QDMs with different dot-to-dot separations increases as more alloy is introduced into the barrier. The plot is for QDMs with alloy present within the full barrier region, where hole state confinement is lost at 7%, 7%, 8%, 9%, and 9% alloy for separations of 5, 7, 10, 13, and 18 lattice constants, a, respectively.

the missing data points for higher alloy concentrations in Figure 5.10; larger dot separations result in slower delocalization for the dot states with respect to alloy concentration, hence the inclusion of data points for higher alloy concentration. The separation of $7a$ is an odd case for which barely any tunnel enhancement is achieved by alloying. We believe this to be a transition point related to the crossing over of anti-bonding to bonding ground state geometries [17].

In summary, we have found an optimal QDM geometry for tunnel coupling enhancement at a top-of-bottom wetting layer to bottom-of-top wetting layer separation of $10a$. Additionally, by introducing alloy to the full 10 lattice constant barrier region between the dots allows us to achieve the maximal amount of tunnel coupling enhancement. There is a shift in electrical bias at which resonance occurs, due to the

additional asymmetry in strain caused by the alloy. However, this effect can easily be compensated for by increasing the electrical bias applied across the dots.

Chapter 6: Spin-orbit induced spin-mixing in QDMs

Hole states in QDs are more strongly confined than electron states. This gives us the ability to isolate states in either dot unless the hole states are intentionally brought into resonance with an electric field along the stacking axis of the dots (z-direction). The lowest-energy hole state spin pair for each dot gives us a four state system that can be tuned, on demand, in and out of resonance. In addition to the tunnel resonance discussed in the previous chapter, we can generate a spin-mixing resonance by introducing cylindrical symmetry breaking, either by an alloy barrier or by offset dots. Cylindrical symmetry breaking presents a lateral lever-arm, in which a “torque" is applied to the angular momentum of the system and the induced spin-orbit coupling leads to spin mixing. The result is that, in addition to the spin-preserving tunneling seen previously, the hybrid states formed across the two dots at resonance contains spin-mixed components. The spin-mixed states are what is required for driving qubit rotation through a Λ transition. The larger the spin-mixing strength, the faster qubit rotation.

Another aspect of resonance spin behavior for QDMs is the electrical tunability of the hole state g-factor through resonance. Because the spin-up states (defined relative to the z axis) have different tunnel coupling rates across the dots compared to the spin-down states, the relative energy difference of the four hole states do not remain constant as the dots are brought into resonance. Thus, the effective splitting between spin-up and spin-down states either increase or decrease as the dots

are brought into resonance, depending on whether a symmetric or anti-symmetric tunnel coupled state was formed.

We now add an applied magnetic field to the TB Hamiltonian in order to calculate magnetic field dependent resonance effects, such as spin-mixing and the change in g-factor at resonance. The anti-crossing energies of the TB wavefunctions show a substantial increase in spin-mixing strength with the addition of a GaBiAs barrier. In contrast, the decrease in g-factor at higher alloy concentration also increases the magnetic field strength required to bring the states to energetically overlap and form an anti-crossing. By fitting the TB hole state energies to a simple 4×4 phenomenological Hamiltonian describing the four-state-mixing at resonance, we are able to obtain quantifiable values for spin-mixing, tunnel coupling, g-factor, etc. without the need for high magnetic field strengths. Due to the decrease in g-factor caused by the alloy, we were required to add a shift in the hole state energy proportional to the second order of the magnetic field strength. After this addition of a diamagnetic term, we were able to reaffirm the three-fold enhancement to tunnel coupling previously estimated by the anti-crossing energy, and we were able to show a three-fold increase in spin-mixing strength for offset dots.

The addition of Bi to the inter-dot barrier greatly enhances the change in g-factor at resonance. In conjunction with the enhanced spin-mixing, we are able to form intra-dot spin-mixing, wherein the spin conjugate states of the same dot hybridizes. We believe that this new form of intra-dot spin-mixing might be used as a novel form of spin manipulation. In order to do so, we need to understand the underlying relation between the spin-orbit effect and the resonance behaviors of QDM hole states. A perturbative analysis of the magnetic field shows that both the spin-mixing and resonance g-factor change are effects of the Peierls contribution, or the component

of the magnetic field applied to the effective spatial angular momentum of the wavefunction. When spin-orbit coupling is removed from the system, there is no longer a preferred alignment between the spin of the system and the Peierls effective angular momentum, thus removing any magnetic field effects of the Peierls contribution.

6.1 Resonance effects with a magnetic field – with a pure GaAs barrier

6.1.1 Dot offset and spin mixing

Initially, without a electric or magnetic field applied, the two spin-states of each dot are degenerate and, between the two dots, the pairs are energetically separated by the different strain experienced in their respective dots. The hole state in the bottom dot experiences less compressive strain than the top dot, resulting in a lower hole state energy (higher valence electron energy), see Figure 5.1. Previously, we have found that the typical energy difference between the pair of bottom and top dot states in our structures at zero electrical bias range from 2.3 meV without an alloyed barrier to 4.4 meV with a 7% alloy barrier. When the top and bottom dot hole states are brought into energetic resonance with an applied electric field, they form an anti-crossing tunnel resonance, as discussed in the previous chapter. If a magnetic field is also applied along the stacking axis of the dot, the spin degeneracy is lifted, allowing us to observe four hole states and spin-dependent behavior for resonant dots. Lifting the spin degeneracy allows us to observe spin-mixing and a spin-dependent tunneling strength.

Figure 6.1 shows the four hole state energies of two different QDM systems, both with a pure GaAs barrier. Figure 6.1a shows the hole state energies of two perfectly aligned dots; Figure 6.1b shows the hole state energies when the two dots are laterally offset by $2a$ in the x-direction ([100]). The four valence states at zero electrical bias

are, from highest to lowest energy (lowest energy hole state to highest energy hole state), the bottom dot spin down $|\Downarrow_B\rangle$, bottom dot spin up $|\Uparrow_B\rangle$, top dot spin down $|\Downarrow_T\rangle$, and top dot spin up $|\Uparrow_T\rangle$. An electric field is applied to bring the dots in and out of resonance; a magnetic field of 18 T is applied to remove the spin degeneracy of the states. A high magnetic field is chosen to impose an energetic overlap between the spin states of opposing dots, in order to clearly observe a crossing or anti-crossing in energy. High magnetic field strengths are not required for spin-mixing, and the operational field strength for qubit manipulation is typically less than 2 T.

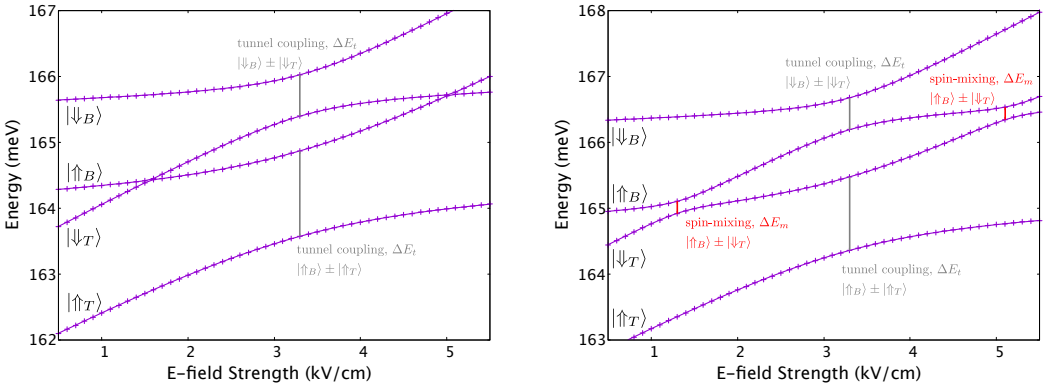

(a) Aligned dots (b) Offset dots

Figure 6.1: Hole states of a InAs/GaAs QDM split by a 18 T magnetic field in the z-direction, brought into and out of resonance with an electrical bias in the z-direction. From highest to lowest valence energy (lowest to highest hole energy), the levels at far from resonance are $|\Downarrow_B\rangle$, $|\Uparrow_B\rangle$, $|\Downarrow_T\rangle$, and $|\Uparrow_T\rangle$. For offset dots, an anti-crossing for spin-mixing is seen at 1.3 kV cm^{-1} and 5.1 kV cm^{-1}

When the two dots of the QDM are perfectly aligned along the stacking axis (Figure 6.1a), the two states of $|\Uparrow_B\rangle$ and $|\Downarrow_T\rangle$ do not form a energetic anti-crossing, implying an absence of mixing between the states. For the offset dots (Figure 6.1b), the presence of spin-mixing is indicated by the anti-crossing between the states of opposite spin before and after the main spin-preserving tunnel resonance. The offset nature of the dots provides the driving force for the creation of spin-mixing. The cylindrical asymmetry of the system provides a lever arm for inducing torque. Dot

offsets along [110] and [1$\bar{1}$0] were also modeled and calculated, and they provide similar spin-mixing results to the offset of [100] shown here. The presence of these spin-mixed states is what allows optical coherent control of rotations between qubit states defined by orthogonal heavy hole spin projections.

6.1.2 Four state projections

Another method of showing the hybridization of the states as they are brought into resonance is to plot their projections onto the far-from-resonance states. We pick the states at an electrical bias of $-5\,\mathrm{kV\,cm^{-1}}$ to represent the basis states of $|\Downarrow_B\rangle$, $|\Uparrow_B\rangle$, $|\Downarrow_T\rangle$, and $|\Uparrow_T\rangle$. The hole states, as they go through resonance, are then projected onto each of the four basis states to show the component breakdown of the hybridized states at each electric field strength. The states far from resonance do not perfectly represent the four spin-up/spin-down and top/bottom dot states, and thus the projection onto the far-from-resonance states is not perfectly symmetric about resonance. Yet, they serve as a qualitative tool in understanding the spin-mixing process in QDMs.

Figure 6.2 shows the four states of the aligned QDM in Figure 6.1a, in order of hole state energy, and the norm of their projections onto the four basis states. Each of the sub-figures shows the basis state breakdown of one of the energy levels in Figure 6.1a. Each data point in Figure 6.1a has a corresponding TB wavefunction. This wavefunction is projected against the four basis states of $|\Downarrow_B\rangle$, $|\Uparrow_B\rangle$, $|\Downarrow_T\rangle$, and $|\Uparrow_T\rangle$ – which we have defined as the TB states at $-5\,\mathrm{kV\,cm^{-1}}$. The four projected values of the TB wavefunctions are the equivalent of an eigenvector if we were to just consider a four state Hamiltonian. The four projected values at different electric fields are then collected, for each energy level comprising a sub-figure, to show how each energy level evolves and mixes the spin states as the two dots are brought into resonance.

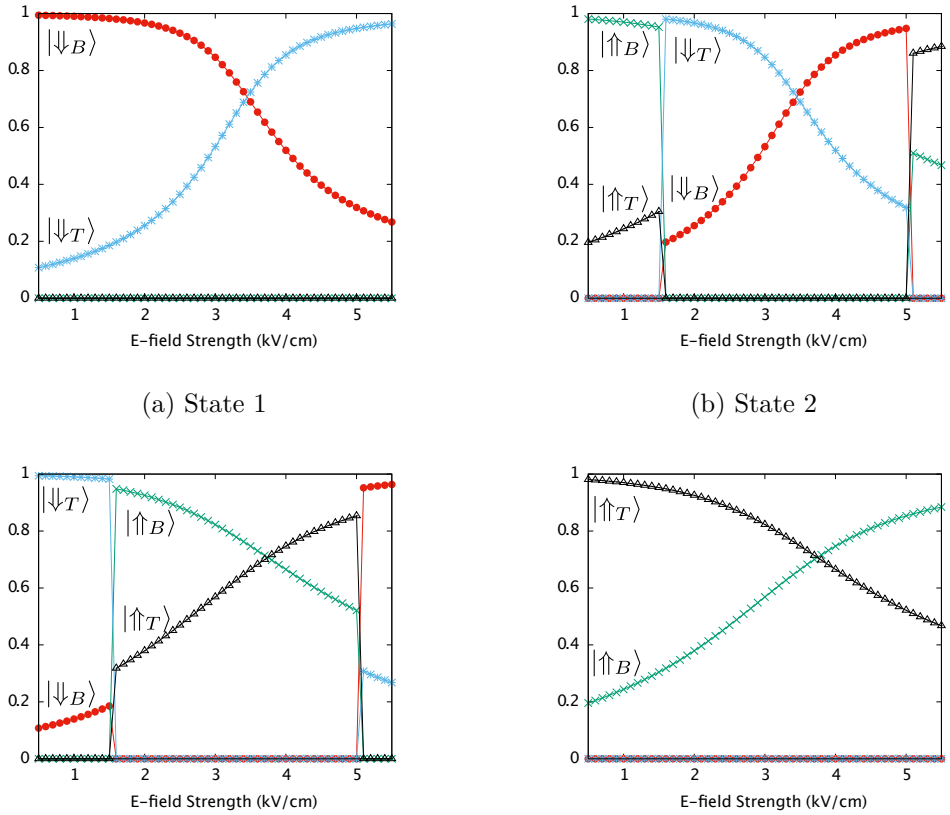

(a) State 1

(b) State 2

(c) State 3

(d) State 4

Figure 6.2: Norm of the projections of the four states of an aligned QDM, projected onto the far-from-resonance basis states. Red, green, blue, and black are projections onto the $|\Downarrow_B\rangle$, $|\Uparrow_B\rangle$, $|\Downarrow_T\rangle$, and $|\Uparrow_T\rangle$ states, respectively. Note that the plot does not start at zero electric field.

At $3.5\,\mathrm{kV\,cm^{-1}}$, we see the tunnel coupling resonance of the two spin-down states in Figure 6.2a and Figure 6.2b. The tunnel coupling between the spin-up states of the two dots is seen in Figure 6.2c and Figure 6.2d. More importantly to note is the absence of any hybridization between states of opposing spin. At the electrical field strength where the states energetically cross in Figure 6.1, we see an immediate switchover of the spin-up basis states to the spin-down basis states, and

vice versa. This is due to the change in level ordering, as each sub-figure represents a state corresponding to an energy level and not a specific spin characteristic. For Figures 6.2b and 6.2c, the section between $1.5\,\mathrm{kV\,cm^{-1}}$ and $5\,\mathrm{kV\,cm^{-1}}$ comprise of the opposite spin-state compared to the other electric field strengths, for each respective plot. We see that this switchover happens solely due to level ordering, without the hybridization of the basis states, indicating that no spin-mixing is present in QDMs with aligned dots.

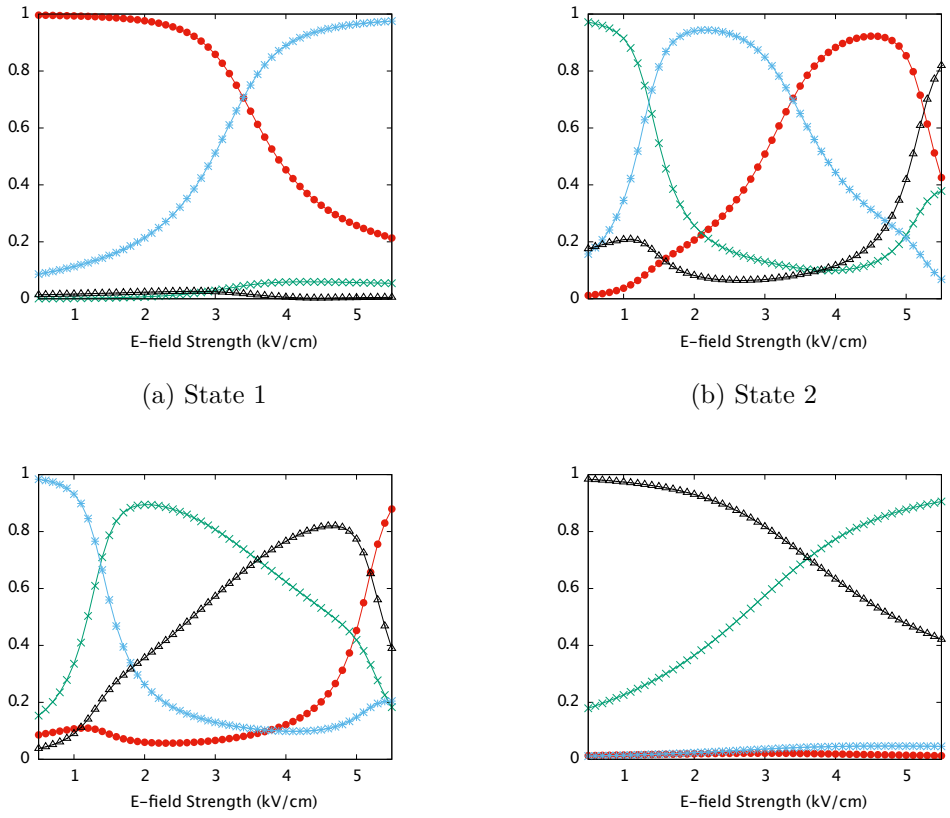

(a) State 1

(b) State 2

(c) State 3

(d) State 4

Figure 6.3: Norm of the projections of the four states of an offset QDM, projected onto the far-from-resonance basis states. Red, green, blue, and black are projections onto the $|\Downarrow_B\rangle$, $|\Uparrow_B\rangle$, $|\Downarrow_T\rangle$, and $|\Uparrow_T\rangle$ states, respectively. Note that the plot does not start at zero electric field.

In contrast, Figure 6.3, which shows the basis breakdown of the states in an offset QDM, indicates a clear spin-mixing of the states as they undergo resonance. At the field strengths for spin-mixed anti-crossings, we see that states 2 and 3 consist of a hybridization of the basis states corresponding to opposite spins from different dots, with the two remaining bases providing a smaller contribution. States 1 and 4 also contain small amounts of contribution from basis states opposite their dominant spin. The spin-mixing between $|\Downarrow_B\rangle$ and $|\Uparrow_T\rangle$ is not weaker than that between $|\Uparrow_B\rangle$ and $|\Downarrow_T\rangle$, but states 1 and 4 in Figure 6.3 are not as strongly spin-mixed due to their energetic separation from their spin-counterparts. Additionally,we notice that the projections are not perfectly symmetric about resonance. This is partly due to the states at $-5\,\mathrm{kV\,cm^{-1}}$ not being a perfect representation of the $|\Downarrow_B\rangle$, $|\Uparrow_B\rangle$, $|\Downarrow_T\rangle$, and $|\Uparrow_T\rangle$ basis states, but also due to the wetting layer causing the system to not be perfectly symmetric in the z-direction (the direction in which the electric field is applied).

6.1.3 Electrical tuning of hole state g-factor

In both the aligned and offset QDM, we see an anti-crossing present between states with the same spin from opposing dots. This is evidence of the spin preserving tunnel coupling, which we have discussed at length in the previous chapter. However, with the addition of a magnetic field, there is an asymmetry between the spin-preserving tunneling strength based on whether the state is spin-up or spin-down. This difference in tunneling strength causes an apparent change in hole state g-factor as the states approach resonance. The resonance g-factor change, and its tunability via alloyed barriers, is also an important aspect in understanding spin behavior in QDMs.

Unlike spin-mixing, the spin-dependent tunnel coupling is always present and does not require cylindrical symmetry breaking. While the tunnel coupling between the dots is spin preserving, the coupling strength between the two up-states is not the

same as the coupling between the two down-states. This can be seen in Figure 6.1, as the anti-crossing energy between the mixed states of $|\Downarrow_B\rangle$ and $|\Downarrow_T\rangle$ (states 1 and 2 at $3.5\,\mathrm{kV\,cm^{-1}}$) is noticeably less than the mixed states of $|\Uparrow_B\rangle$ and $|\Uparrow_T\rangle$ (states 3 and 4 at $3.5\,\mathrm{kV\,cm^{-1}}$). The observable difference in tunneling strength induces an equal but opposite change in the spin-splitting energy, or the effective g-factor, between the symmetric or anti-symmetric molecular state as the hybridization occurs at resonance.

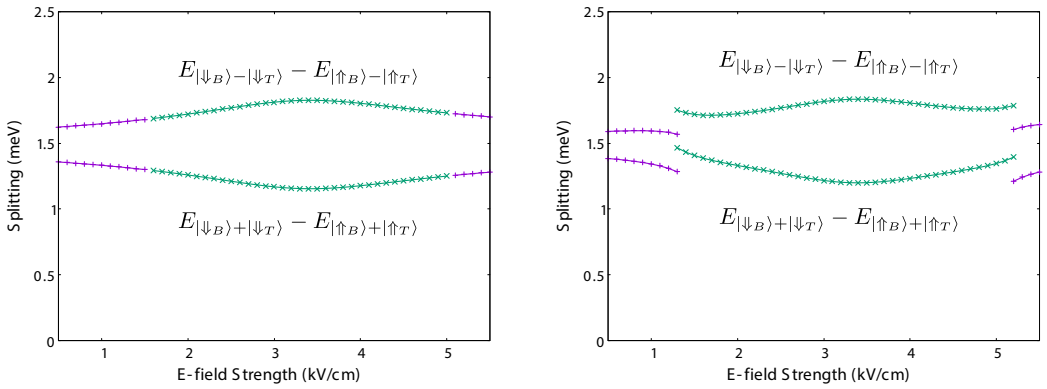

(a) Aligned (b) Offset dots

Figure 6.4: Effective splitting energy of the hole states $E_{\Downarrow_B} - E_{\Uparrow_B}$ and $E_{\Downarrow_T} - E_{\Uparrow_T}$ as the pairs are brought into resonance under a 18 T magnetic field. The resonance forms hybridized symmetric and anti-symmetric states across the two dots with splittings $E_{\Downarrow_s} - E_{\Uparrow_s}$ and $E_{\Downarrow_a} - E_{\Uparrow_a}$ increasing or decreasing due to the difference in spin-preserving tunnel coupling. A jump is present in the offset case as the anti-crossing from spin-mixing opens a gap in splitting energy. Green indicates a splitting defined as the energy difference between states 1 and 3, or 2 and 4; purple indicates a splitting defined as the energy difference between states 1 and 2, or 3 and 4.

If we were to plot the effective splitting of the otherwise spin degenerate states (Figure 6.4), we see an increase in splitting at resonance for one pair of states, and a decrease in splitting for the other pair. The energy difference far from resonance, $E_{\Downarrow_B} - E_{\Uparrow_B}$ and $E_{\Downarrow_T} - E_{\Uparrow_T}$, can be approximated to be the average of the two splittings, giving us roughly $83\,\mu\mathrm{eV\,T^{-1}}$. We can than characterize the resonance shift in g-factor by comparing the off resonance splitting with the minimum or maximum splitting, roughly $66\,\mu\mathrm{eV\,T^{-1}}$ ($100\,\mu\mathrm{eV\,T^{-1}}$) for the bottom (top) dot states.

While the peak in effective splitting occurs at the same electrical bias as the tunnel resonance between the two dots, coinciding with the formation of symmetric and anti-symmetric states, charge density plots show that the splitting and resonance peaks do not align with the proportion of the wavefunction in each material. Previous understanding of the resonance behavior depended on the different charge density in the barrier material for symmetric and anti-symmetric states. It was proposed that the symmetric state, with the higher charge density in the barrier material, would have more of the material properties of the barrier, and thus have a lower the g-factor. However, we have not found evidence to support this argument.

By calculating the projections similar to the ones in the previous section, but onto basis states hybridized by tunnel coupling ($|\Downarrow_B\rangle \pm |\Downarrow_T\rangle$, $|\Uparrow_B\rangle \pm |\Uparrow_T\rangle$), we find that the lower energy state has a higher symmetric component at resonance ($|\Downarrow_B\rangle + |\Downarrow_T\rangle$ for state 1; $|\Uparrow_B\rangle + |\Uparrow_T\rangle$ for state 3). By summing over the square of the probability amplitude of the TB wavefunctions at each site, we can obtain the charge density for each material or region. We do not find a significant difference in the probability of the wavefunction to be in the barrier material for the symmetric and anti-symmetric states. Figure 6.5 shows that very little of the wavefunction probability, or hole state charge density, is present outside the InAs dot. Moreover, the maximum difference in charge density does not occur at resonance, where the maximum difference in g-factor is obtained. Therefore, we conclude that the change in hole state g-factor through resonance is driven by a spin-dependent tunneling between the dots, and has little dependence on the difference in material g-factors. From analysis on the QDMs with a GaBiAs alloyed barrier (Section 6.5) we find that the spin-dependence of the tunnel coupling greatly increases from the increase in SO coupling, resulting in a greater resonance change in effective g-factor. Just as for

spin-mixing, the electrical tunability of the hole state g-factor is also a property that can be enhanced by introducing an alloyed material.

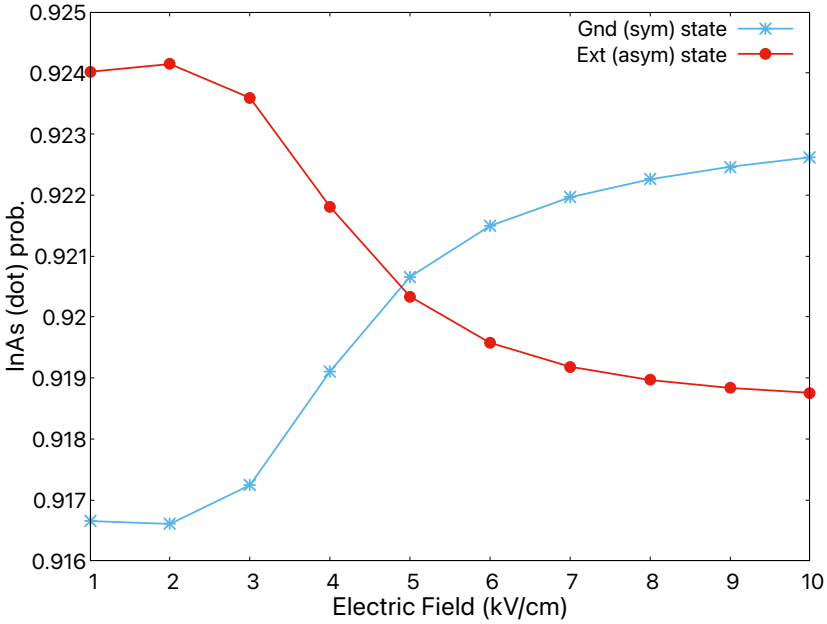

Figure 6.5: Portion of the TB wavefunction to be in the InAs dot region, for a InAs/GaAS QDM without Bi. The remainder of the wavefunction will be in GaAs, either in the inter-dot barrier or surrounding substrate.

6.2 Alloy concentration

6.2.1 Low alloy concentrations and splitting reduction

By introducing a GaBiAs alloy in the barrier, we expect both an enhancement of spin-mixing from the stronger spin-orbit effect of barrier material and a stronger resonance from a lowered barrier height. Figure 6.6 shows the four holes states of a QDM passing through resonance, under an 18 T magnetic field applied in the z-direction, with a 4% Bi random alloy replacing the GaAs inter-dot barrier. With the $GaBi_{0.04}As_{0.96}$ barrier, there is a reduction of the resonance g-factor for both pairs of spin-split states from the non-alloyed case (97 μeV T^{-1} and 37 μeV T^{-1} compared

to $100\,\mu\text{eV}\,\text{T}^{-1}$ and $66\,\mu\text{eV}\,\text{T}^{-1}$ without an alloy). Additionally, the off resonance g-factor calculated by the average of the two splittings has also decreased significantly from the non-alloyed case ($67\,\mu\text{eV}\,\text{T}^{-1}$ compared to $88\,\mu\text{eV}\,\text{T}^{-1}$). The combined effect shows a decrease in off-resonance g-factor and an increase in the resonance g-factor shift as a result of introducing the alloyed barrier.

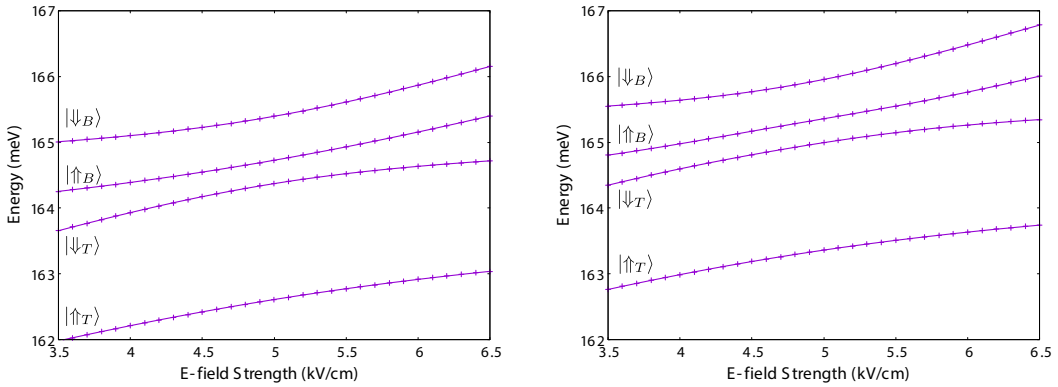

(a) Aligned dots, 4% alloy

(b) Offset dots, 4% alloy

Figure 6.6: Hole states split by a 18 T magnetic field for a 4% alloy barrier. The two dots of the QDM are either (a) aligned or (b) offset by $2a$ in the x-direction.

The reduction in g-factor causes the two opposing spin states from the two dots ($|\Uparrow_B\rangle$ and $|\Downarrow_T\rangle$) to not energetically overlap. However, this does not indicate an absence of spin-mixing, similar to how the low operational field strength (1 T to 2 T) will not introduce enough splitting energy to energetically overlap the states, but does not preclude the formation of a spin-mixed state that can drive a Λ-transition. However, the reduced splitting caused by the alloy does present a challenge for analysis using the energies of the hole states. Without a clear anti-crossing, the hole state energies do not provide any qualitative insight on how the alloyed barrier affects the spin-mixing.

Increasing the magnetic field strength further in order to induce an overlap of spin states from which a hole spin mixing anti-crossing energy can be measured is feasible with the TB model, but this has the potential to introduce unwanted higher

order magnetic field effects. The decrease in g-factor from the introduction of the alloyed barrier indicates a relative decrease in the linear terms associated with the magnetic field. Considering the practical magnetic field strengths such a device will experience and the desired precision of fitted parameters, we instead modify the four-state Hamiltonian presented in Ref [16] to account for the splitting reduction cause by the alloy barrier. We found that the addition of diamagnetic corrections was necessary to achieve satisfactory fit parameters, but magnetic field terms beyond second order are insignificant for the range of field strengths in our calculations. Further discussion of the fitted model and parameters, especially in regards to spin-mixing, will be in Section 6.4.

6.2.2 High alloy concentration and intra-dot spin mixing

The 4% alloyed barrier showed a decrease in g-factor of the dots sates caused by the alloy, and while we have yet to quantify the change in spin-mixing or g-factor tunability, the alloy concentration was low enough to not fundamentally change the behavior of the hole states as they approach resonance. However, increasing the alloy concentration to 7% results in a reordering of the energy levels during resonance, introducing a new intra-dot level crossing between the two lowest energy hole states (highest energy valence state). With 7% alloy, we also see a significant widening of resonance, a phenomena that was also present but not immediately evident with the 4% alloy.

Figure 6.7 shows the hole state energies of a QDM with a 7% random alloy barrier. As is with the 4% barrier, we still see a lack of any energetic overlap of states from opposing dots due to a significant alloy reduction in g-factor inhibiting energetic overlap of the states, even at high magnetic field strengths. Yet, because of the alloy enhancement of the resonance g-factor change, the change in splitting energy for the bottom dot states between on and off resonance is now greater the intrinsic

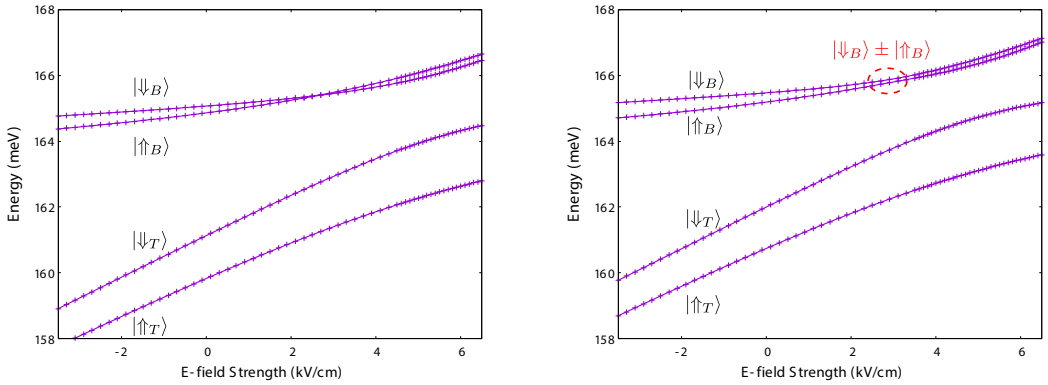

(a) Aligned dots, 7% alloy

(b) Offset dots, 7% alloy

Figure 6.7: Hole states split by a 18 T magnetic field for a 4% alloy barrier. The two dots of the QDM are either (a) aligned or (b) offset by $2a$ in the x-direction. The two states of the bottom dot (state 1 and state 2) show a small anti-crossing for the offset case.

g-factor of the states far from resonance. For the electrical field strengths around peak resonance, a negative splitting energy is achieved when the resonance behavior decreases the g-factor of the bottom dot states more than their intrinsic g-factor. This reversal of sign for the splitting results in a reordering of the energy levels, creating a level crossing (or anti-crossing) at the two electric field strengths where the combined resonance g-factor shift and the intrinsic off-resonance g-factor is zero.

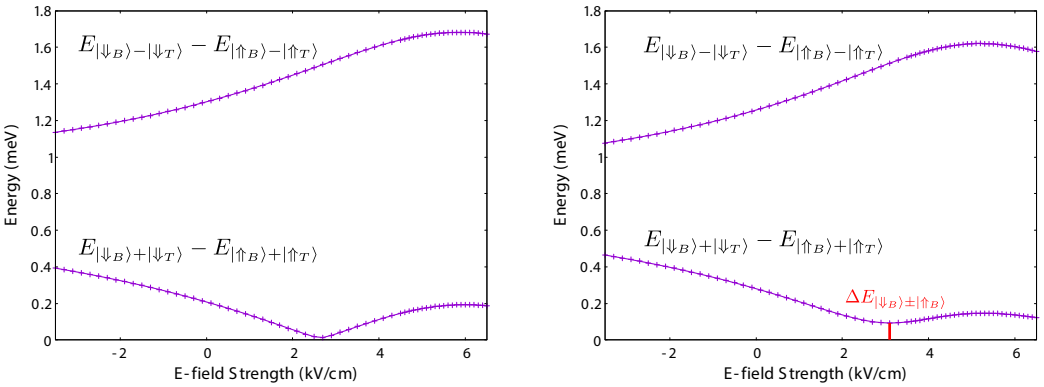

(a) Aligned dots

(b) Offset dots

Figure 6.8: Effective splitting energy of the hole states $E_{\Downarrow_B} - E_{\Uparrow_B}$ and $E_{\Downarrow_T} - E_{\Uparrow_T}$ as the pairs are brought into resonance under a 18 T magnetic field. The change in g-factor as a result in resonant behavior overpowers the intrinsic g-factor of the bottom dot states, thus creating a negative splitting, or a level reordering. The splitting here is plotted as the energy difference, and is always positive.

The crossover point where the resonance behavior overpowers the off-resonance g-factor is much more evident when plotting the effective splitting of the spin pairs through resonance (Figure 6.8). Just as the system without alloy (Figure 6.4), the two holes state originating from the bottom (top) dot have a spin splitting that gradually decreases (increases) as the dots are brought into resonance. However, the alloyed barrier causes the shift in g-factor between on and off resonance to be much greater than the non-alloyed system. The alloy also decreases the off resonance g-factor for the states to roughly $44\,\mu\mathrm{eV\,T^{-1}}$. Therefore, the QDM with the 7% alloyed barrier has an on resonance splitting of $-11\,\mu\mathrm{eV\,T^{-1}}$ ($99\,\mu\mathrm{eV\,T^{-1}}$) for the pair of states that originated in the bottom (top) dot off-resonance. While the strength of the effective splitting energy scales roughly linear with the magnetic field strength, the point at which the splitting changes sign remains at the same electrical bias regardless of magnetic field strength (Figure 6.9). The anti-crossing that occurs at the switchover for offset dots also scales linearly with magnetic field.

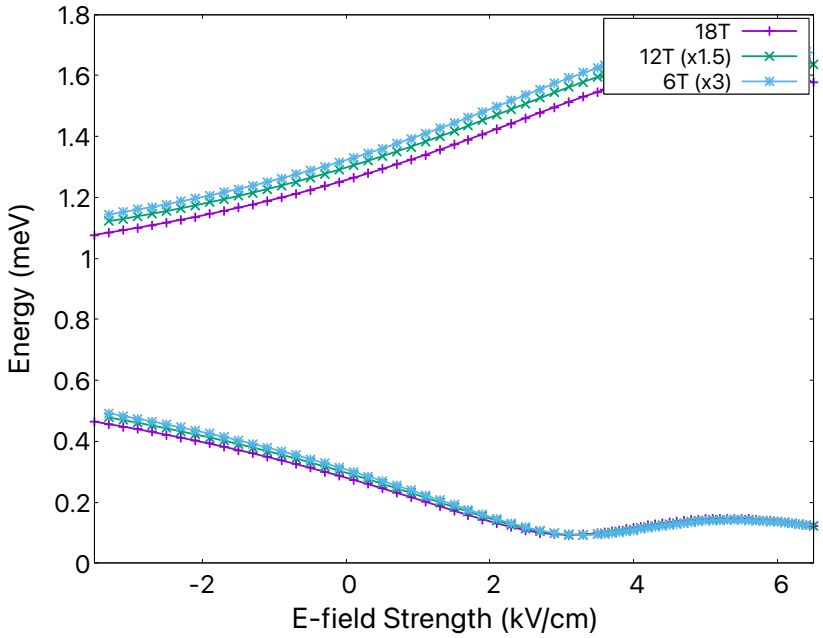

Figure 6.9: Effective splitting energy of the hole states in a offset QDMs with a $GaBi_{0.07}As_{0.93}$ barrier, scaled relative to the strength of the magnetic field. The TB wave-function energies and splittings are calculated independently at each magnetic field strength, and then multiplied by a factor relative to 18 T

Additionally, if a cylindrical symmetry breaking offset is present, the same mechanism that introduces spin-mixing between the two dots now generates a mixing of the two spin states within the bottom dot. This intra-dot spin-mixing can be reproduced with the same parameter-fitting four-state Hamiltonian for the systems without explicit intra-dot mixing (Section 6.4). No additional terms of direct coupling between the two same-dot hole states need to be added, indicating intra-dot spin-mixing to be an indirect coupling of hole states through inter-dot spin-mixing and tunnel coupling.

6.3 Alloy configuration

6.3.1 Layered GaBiAs barrier

As opposed to a barrier entirely comprised of GaBiAs, an alternative barrier we propose is comprised of layers of different materials. In this configuration, bismuth is only present in a smaller 4a slice within the larger 7a barrier, resulting in a layer of GaBiAs sandwiched between layers of pure GaAs (Figure 2.1d). This does lower the overall alloy concentration, and the alloy effects are mostly proportionally weaker (Figure 6.10). Unlike previous effects, such as the energy levels and the tunnel coupling, we do not see direct effects of alloy strain on the spin-mixing properties of the QDM. The previously discussed effects, such as a shift in where the resonance occurs, are still present with a magnetic field applied.

6.3.2 Ordered and clustered distribution of alloy

In addition to the partially alloyed setup, we also ran calculations for different fully alloyed barriers. Running multiple initial seeds for the random alloy generated little difference to the four-state resonance behavior, indicating that, for the alloy concentrations we tested, the four lowest energy dot states are energetically isolated enough from the more noisy alloy barrier states. Ordered alloys where the Bi was

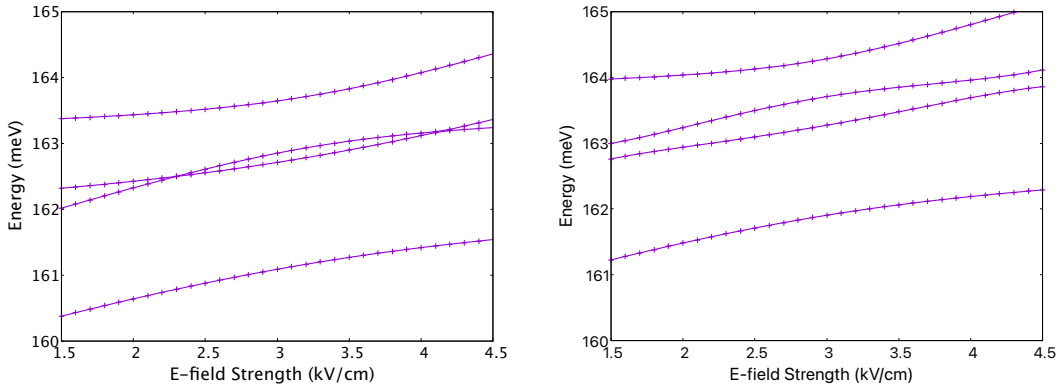

(a) partial 4% Bi aligned

(b) partial 4% Bi offset

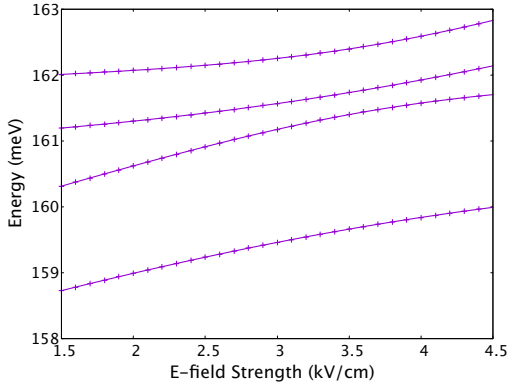

(c) partial 7% Bi aligned

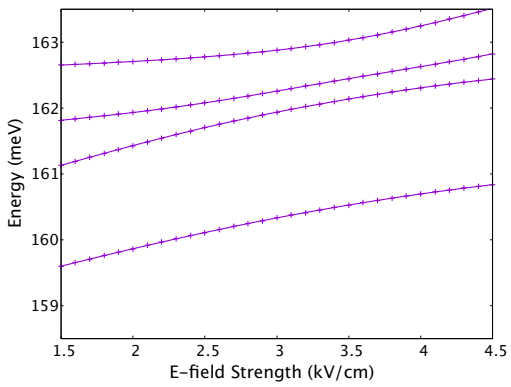

(d) partial 7% Bi offset

Figure 6.10: Energy levels of an InAs QDM with a partial $GaBi_xAs_{1-x}$ barrier under a 18 T magnetic field. Note scale on x-axis.

placed periodically in the barrier lattice had an overall slightly weaker effect than the randomly placed alloy, but fundamentally behaved the same. Finally, we had a clustered alloy, where, after an initial random pass of alloy placement, a second pass where the chance of placing a Bi atoms is increase by 10% for every next nearest neighbor of Bi. This simulates the atom migration during MBE growth, where Bi atoms tend to clump together. Running the TB calculation for clustered alloys resulted in very similar results to a random alloy at low concentrations. At higher concentrations, the clustered alloy seems to be able to induce more spin-mixing into the QDM with aligned dots. We do not have enough realizations of the clustered

alloy to determine if this is a direct consequence of the clustered placement of Bi or just an extreme case in the variation of the placement.

6.4 Effective model for spin-mixing

Previously, experimental results for QDMs without alloy were fit to the empirical model given by Doty in Ref. [16]. The same fit can be used on the energies calculated from a TB model. By defining pseudo-spin up and down for both dots, we would have four basis states $\{E_{B\Downarrow}, E_{B\Uparrow}, E_{T\Downarrow}, E_{B\Uparrow}\}$. As such, the system with applied magnetic field B and electric field F, both in the z-direction, would be described by a 4×4 Hamiltonian, $H = H_0 + H_{sm}$, with

$$H_{sm} = \begin{pmatrix} \mu_B g_B B & 0 & -t + \mu_B g_{12} B & -m \\ 0 & -\mu_B g_B B & m & -t - \mu_B g_{12} B \\ -t + \mu_B g_{12} B & m & -dF + \mu_B g_T B & 0 \\ -m & -t - \mu_B g_{12} B & 0 & -dF - \mu_B g_T B \end{pmatrix}, \quad (6.1)$$

where $g_{B/T}$ is the hole state g-factor of the bottom/top dot state, g_{12} is the asymmetric change in g-factor due to spin-dependent resonant tunneling, t is the tunnel coupling strength, and m is the spin-mixing strength. μ_B is the Bohr magneton and d is the effective distance between the two dots. H_0 is just the zero-field off resonance energies of E_B and E_T,

$$H_0 = \begin{pmatrix} E_B & 0 & 0 & 0 \\ 0 & E_B & 0 & 0 \\ 0 & 0 & E_T & 0 \\ 0 & 0 & 0 & E_T \end{pmatrix}. \quad (6.2)$$

This model only includes the g-factor of the holes states along the z-direction, and is thus only valid for cases where magnetic field is also along the the z-direction.

While this Hamiltonian was good enough for previous experimental data, initial fits to alloyed systems gave inconsistent parameters. The two main issues were the low observable spin-splitting caused by alloy enhancement of the resonance g-factor change (g_{12}) and various procedural problems in writing a fitting program. The former resulted in the necessity of adding a diamagnetic term, which we will address in the next section, while the latter is documented in Appendix B.

6.4.1 Strong diamagnetic effects

One of the strongest effects of the alloyed barrier was a decrease in observed splitting. Not only does the alloy modify the intrinsic g-factor of the dots, it also has a the strong effect on the resonance behavior contributing to the g-factor tunability. The reduction in observed splitting results in a difficult fit for g_T, g_B, and g_{12}, as well as inconsistent values for the zero field energies $E_{T/B}$.

Table 6.1: At resonance, observed splitting strength versus diamagnetic shift obtained from a parabolic fit.

$E(B) = E_{T/B} \pm \mu_B g_{B/T} B - \chi B^2$	0%	4%	7%
First order splitting, bottom dot $\mu_B g_B$ (μeV T^{-1})	37	21	4.3
First order splitting, top dot $\mu_B g_T$ (μeV T^{-1})	51	51	49
Second order magnetic splitting χ (μeV T^{-2})	1.2	1.3	1.4

A simple parabolic fit of hole states energy at resonance to the magnetic field strength shows the observed splitting parameter decrease drastically with the addition of an alloyed barrier (Table 6.1). At 10 T, even the moderately alloyed case of 4% shows an effective first order splitting energy only twice that of the second order shift in energy. As the alloy progressively causes the first order and second order

contributions to the energy shift to be more similar, we have a more and more difficult time fitting g_T, g_B, and g_{12} to the 4×4 Hamiltonian Eq 6.1. This issue can be resolved by adding a diamagnetic shift as an overall energy correction:

$$H_{sm} = \begin{pmatrix} \mu_B g_B B - \chi_B B^2 & 0 & -t + \mu_B g_{12} B & -m \\ 0 & -\mu_B g_B B - \chi_B B^2 & m & -t - \mu_B g_{12} B \\ -t + \mu_B g_{12} B & m & -dF + \mu_B g_T B - \chi_T B^2 & 0 \\ -m & -t - \mu_B g_{12} B & 0 & -dF - \mu_B g_T B - \chi_T B^2 \end{pmatrix}, \tag{6.3}$$

where $\chi B/T$ are the diamagnetic correction to the bottom/top dot states, respectively.

While the diamagnetic corrections for the two dots can be fit as either the same parameter or two separate parameters without affecting the outcome of the other parameters of the fit much, we have chosen to fit the the diamagnetic corrections as two separate terms to reflect the slightly different symmetry of the bottom and top dot with regard to their wetting layers. Additionally, note that we are using the term "diamagnetic" as a catchall for any and all energy shifts second order in magnetic field, without accounting for whether they are truly diamagnetic or paramagnetic in nature. We chose to refer to the second order dependence on magnetic field as diamagnetic, as the valence energy decreases with respect to magnetic field strength.

The inclusion of the diamagnetic correction also resolves the issue with inconsistent fitted results for $E_{T/B}$. All the fitting parameters in Eq. 6.3, $E_{T/B}$, $g_{T/B}$, $\chi_{T/B}$, g_{12}, d, t, and m, have no intrinsic dependence on magnetic field strength, allowing us to keep some parameters constant after fitting to a zero-magnetic field

results (see Appendix B). This allows us to confirm that, despite the overall diamagnetic change in energy, the splitting energy ($\mu_B g_{T/B} B$) and resonance effect of $\mu_B g_{12} B$ are still linear with respect to magnetic field and fully capturable with a first order perturbation theory.

6.4.2 Increased coupling and decreased g-factors with alloyed barrier

After correcting for diamagnetic contributions and various fit adjustments (see Appendix B), we have a reliable method of obtaining dot g-factors, tunneling strength, spin-mixing strength, and other system parameters for QDMs with alloyed barriers. Firstly, in Figure 6.11, we observe the same three fold increase in tunneling strength for 7% random alloy barriers that we did in Chapter 5.

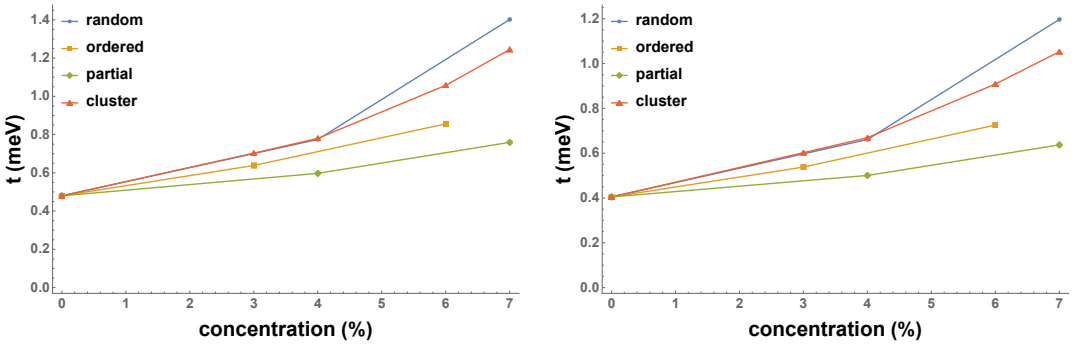

(a) Aligned dots (b) Offset dots

Figure 6.11: Fitted values for tunnel coupling, t.

We also see a steady increase in spin-mixing with alloy concentration (Figure 6.12). Curiously, for the aligned dots, we see no spin-mixing for the 3% ordered alloy and a spin-mixing comparable to the offset dot for 6 % and 7% clustered alloy. The lack of dot misalignment in the clustered configuration made the system more sensitive to unbalanced alloy distributions that may occur in clustered alloys. For the 3%

ordered alloy, no cylindrical symmetric breaking was present and the alloy properties could not provide much spin-mixing.

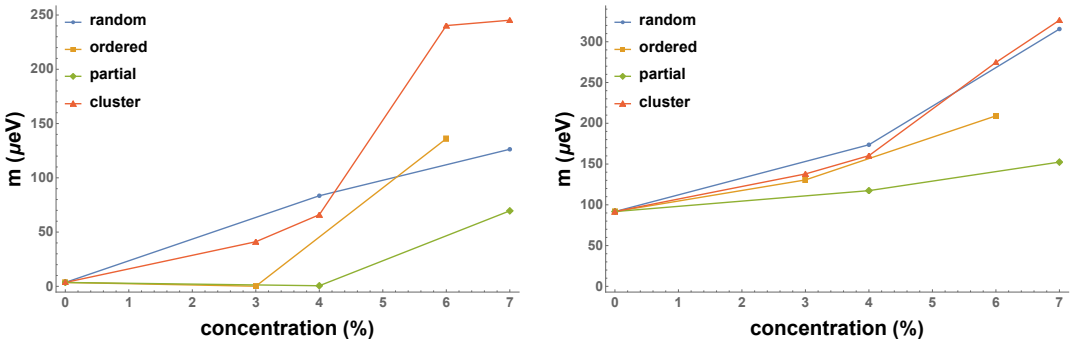

(a) Aligned dots (b) Offset dots

Figure 6.12: Fitted values for spin-mixing, m.

We are also able to quantify the increase in asymmetric tunneling, g_{12}, due to alloying. Figure 6.13 shows an increase in asymmetric tunneling with alloy concentration. The increase in g_{12} has the least variation between the random and clustered alloy distributions.

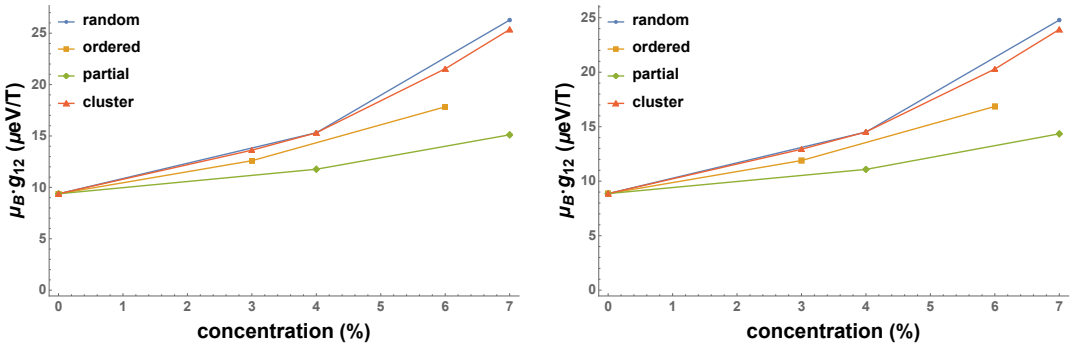

(a) Aligned dots (b) Offset dots

Figure 6.13: Fitted values for asymmetric tunneling, g_{12}.

As observed in earlier sections of the paper, there is also a steady decrease in the off resonance g-factors with increased alloy concentration. The fitted results are shown in Figure 6.14. The bottom dot starts off with a slightly higher g-factor than the top dot, but both dots show a similar amount of g-factor reduction as a result of introducing an alloyed barrier. This is in contrast to the overall energy shift, where a difference in strain experienced by the top and bottom dot when the barrier was fully alloyed caused a larger energy shift for the bottom dot.

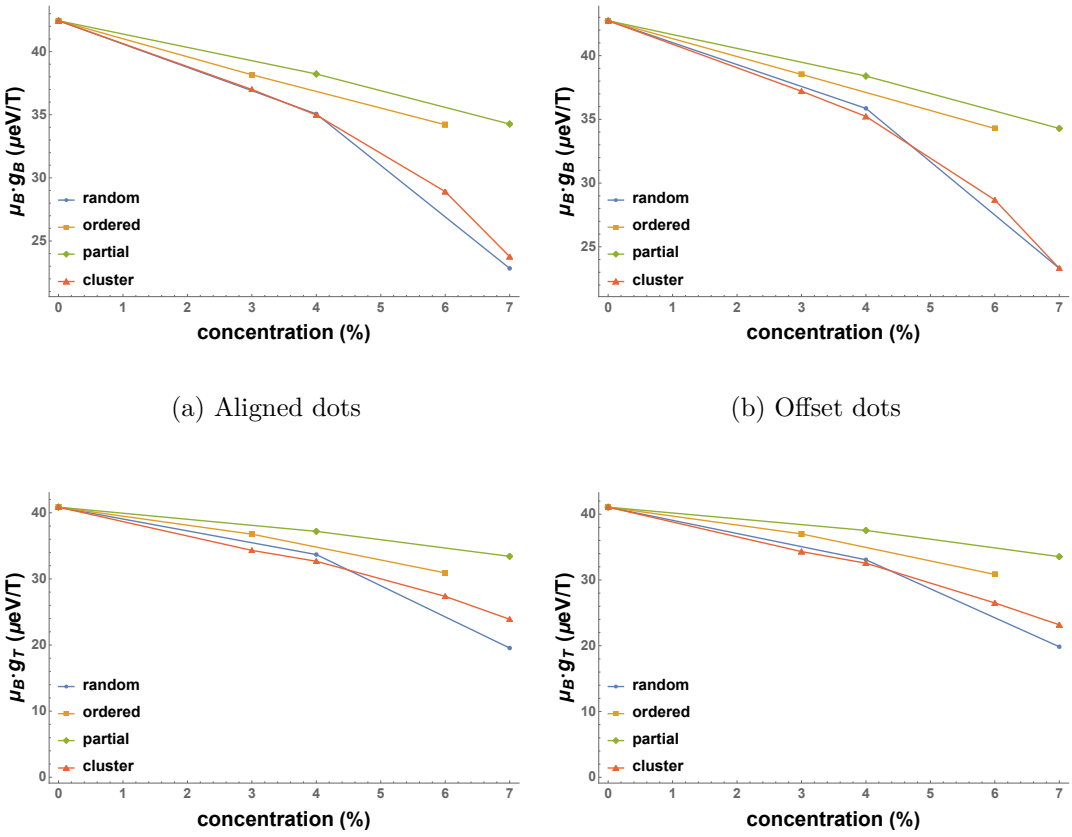

(a) Aligned dots

(b) Offset dots

(c) Aligned dots

(d) Offset dots

Figure 6.14: Fitted values for hole state g-factors, g_B and g_T. Note that the y-axis does not go to zero for g_B

While the 4-state phenomenological Hamiltonian gives us quantifiable parameters, it does not explain the underlying physics governing said parameters. In the

next section, we seek further analysis of the TB wavefunctions using a perturbative analysis of the magnetic field.

6.5 Perturbative analysis of alloy spin-orbit effects

One of the strongest effects we see when Bi is added to the inter-dot barrier is the reduction of spin splitting of the hole states. The application of the magnetic field in the TB model can be broken down into three contributing factors: the spin of the state ($\vec{S}$), the orbital state at each atomic site ($\vec{L}$), and the overall orbital motion of the wavefunction from the Peierls transformation. Under the full TB model, the magnetic field dependent terms are,

$$\delta_{nn'}\mu_B \left(2\vec{S}_{\alpha\alpha',n} + \vec{L}_{\alpha\alpha',n}\right) \cdot \vec{B}(\vec{R}_n) \tag{6.4}$$

and

$$\exp\left[-\frac{ie}{\hbar}\int_{\vec{R}_n}^{\vec{R}_{n'}} \vec{A}(\vec{s},t)\cdot d\vec{s}\right] t^0_{\alpha\alpha'}(\vec{R}_n - \vec{R}_{n'}). \tag{6.5}$$

To avoid performing the full TB diagonalization for each and every separate contribution, we employ a computationally cheaper method using perturbation theory. With the unperturbed Hamiltonian of

$$H^{B=0}_{\alpha\alpha',nn'} = \delta_{\alpha\alpha'}\delta_{nn'}\epsilon_{\alpha n} + \delta_{nn'}\Delta_{\alpha\alpha'} + t^0_{\alpha\alpha'}(\vec{R}_n - \vec{R}_{n'}), \tag{6.6}$$

we define a perturbation Hamiltonian of

$$
\begin{aligned}
&H^1_{\alpha'\alpha,nn'}(B) \\
&\approx \delta_{nn'}\mu_B \left(2\vec{S}_{\alpha\alpha',n} + \vec{L}_{\alpha\alpha',n}\right)\cdot \vec{B}(\vec{R}_n) \\
&\quad + \left[-\frac{ie}{\hbar}\int_{\vec{R}_n}^{\vec{R}_{n'}} \vec{A}(\vec{s})\cdot d\vec{s}\right] t^0_{\alpha\alpha'}(\vec{R}_n - \vec{R}_{n'}) \\
&= \delta_{nn'}\mu_B \left(2\vec{S}_{\alpha\alpha',n} + \vec{L}_{\alpha\alpha',n}\right)\cdot \vec{B}(\vec{R}_n) \\
&\quad - \frac{ie}{2\hbar}\left[\left(\vec{B}\times\left(\frac{\vec{R}_n + \vec{R}_{n'}}{2}\right)\right)\cdot\left(\vec{R}_n - \vec{R}_{n'}\right)\right] t^0_{\alpha\alpha'}(\vec{R}_n - \vec{R}_m) \\
&= \delta_{nn'}\mu_B \left(2\vec{S}_{\alpha\alpha',n} + \vec{L}_{\alpha\alpha',n}\right)\cdot \vec{B}(\vec{R}_n) \\
&\quad + \frac{ie}{2\hbar}(\vec{B}\cdot\vec{n}_{nn'})\ t^0_{\alpha\alpha'}(\vec{R}_n - \vec{R}_{n'})
\end{aligned}
\tag{6.7}
$$

with $\vec{n}_{nn'} = \left(\vec{R}_n \times \vec{R}_{n'}\right)$.

The implemented perturbation allows us to obtain the linear response to magnetic field from each of the three terms or any combination thereof. Computational resources are saved by only needing to run diagonalization of the full TB Hamiltonian once, without magnetic field. Degenerate first order perturbation is then used to split pairs of degenerate wavefunctions of the zero-magnetic field states. The perturbative results are useful for studying low magnetic field strengths without having to recalculate the full TB Hamiltonian at the new fields strengths or directions. More details on the computational methods used can be found in Section 2.2

Linear perturbation theory correctly gives the Zeeman splitting and the ordering of the states. We have found that the perturbative results accurately capture the splitting energy, compared to full TB calculations up to 18 T for all tested cases, and up to 24 T for most cases. Each of the thee contributions and the total splitting scales linearly with magnetic field strength. Thus, the strength of the magnetic field

is irrelevant for understanding the three contributing components. Additionally, for magnetic fields in the Faraday configuration (in the z-direction for our case), the total splitting energy is approximately the contribution from the Peierls term minus the sum of the spin and orbital terms. However, the first order perturbation only calculates the splitting of the degenerate spin states, and is inadequate in regards to overall energy shifts from higher order magnetic effects such as the diamagnetic shifts, nor is it able to describe the spin-mixing interaction with states of the opposing dot.

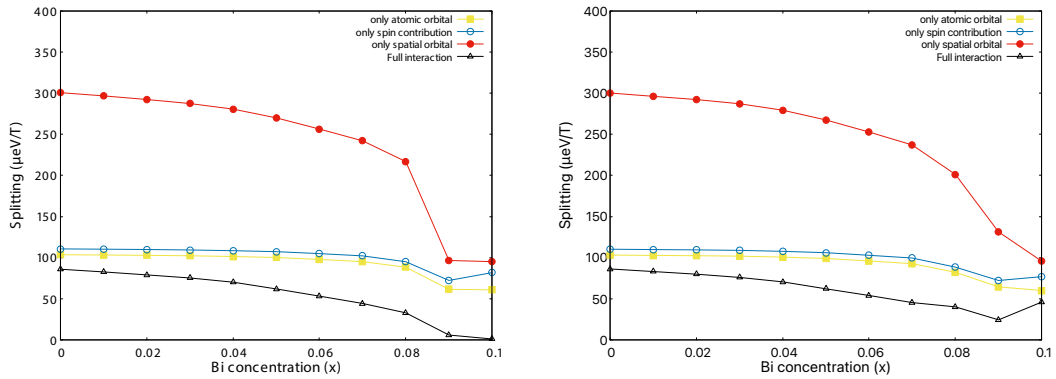

(a) Aligned dots (b) Offset dots

Figure 6.15: Average splitting of top and bottom dot states with total splitting and each of the three magnetic contributions. The splitting is obtained with a magnetic field of 1 T in the z-direction (Faraday configuration). Due to the perturbative model, the splitting can be written as a linear response to the magnetic field strength in terms of $\mu\text{eV T}^{-1}$.

Figure 6.15 shows the splitting energy at 1 T for a QDM with fully alloyed barrier, at zero electrical bias. The data point for each alloy concentration is the average splitting between the top and bottom dot states (ground and first excited states). As seen in the splitting energy calculated from the TB hole states, e.g. Figure 6.4 and Figure 6.8, the splitting of the bottom or top dot state decreases or increases by an equal and opposite amount as the states are brought into resonance. The average splitting of the top and bottom dot states thus gives us the splitting without concern of how close the states are to resonance, which changes with alloy concentration. With resonance effects removed, the splitting at zero electrical bias, shown in Figure 6.15, shows just

the alloy dependence and the relationship between the three contributions. We will discuss the resonance behavior of the three contributions in the next subsection.

The average splitting between the top and bottom dot states (ground and first excited states) are shown to account for the shift in resonance as a result of alloying. This removes the resonance change in g-factor, and just shows the alloy dependence. Prior to alloy concentrations of 8%, before the barrier states start mixing with with dot states energetically, we see each contribution add up linearly, up to a sign, indicating all three contributions are either aligned or anti-aligned with the magnetic field. After 8% alloy, the delocalization of dot states sees that the three contributions no longer interact with the magnetic field independently, with the excited state being deeper in the valence band receiving a larger effect.

In Figure 6.15, we see the decrease in the intrinsic hole state g-factor with increasing alloy concentration. All three contributions decrease at a proportionally equal rate. We also see that the total splitting is equal to the Peierls contribution minus the sum of the spin and atomic orbital contributions. When the magnetic field is in the z-direction, the Faraday configuration, the spin is either parallel or anti-parallel to the magnetic field. The atomic orbital angular momentum and the Peierls angular momentum are always in the z-direction, due to the flat disk shape geometry of the dot. The strong spin-orbit coupling of the system aligns the spin with the other two angular momenta. Only when the contributions are aligned do they share a perturbed basis, resulting in the total splitting to be equal to the Peierls contribution minus the sum of the spin and orbital contribution. In the case where the magnetic field is not in the Faraday configuration, the spin is not able to follow the magnetic field due to being "locked" to the other two orbital angular momenta. The misalignment results in a total splitting not characterized by the sum of the three contributions (Figure 6.16).

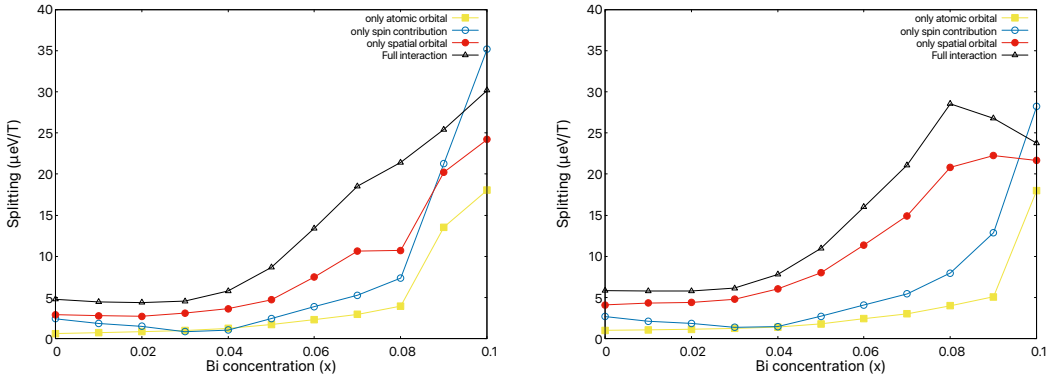

(a) Aligned dots

(b) Offset dots

Figure 6.16: Average splitting of top and bottom dot states with total splitting and each of the three magnetic contributions. The splitting is obtained with a magnetic field of 1 T in the x-direction (Voigt configuration). Due to the perturbative model, the splitting can be written as a linear response to the magnetic field strength in terms of $\mu\text{eV T}^{-1}$.

6.5.1 Alloy concentration and g-factor tuning

There are two reasons for the reduction in splitting strength for the hole state in the bottom dot with the inclusion of an alloyed barrier. First, there is the intrinsic reduction of the off-resonance g-factor of the states ($g_{T/B}$), where both strain and electronic scattering induced by the alloy are contributing factors. This g-factor reduction occurs at all electric field strengths, independent of whether the two dot are in energetic resonance. Secondly, there is the on resonance behavior, where spin-dependent tunneling (g_{12}) can either increase or reduce the effective splitting of the excited or ground state, respectively. As the alloy both widens and increases the strength of the resonance, the effective g-factor of the lower energy bottom dot state decreases drastically. The resonance increases the splitting of the higher energy top dot state, which competes with intrinsic loss of g-factor.

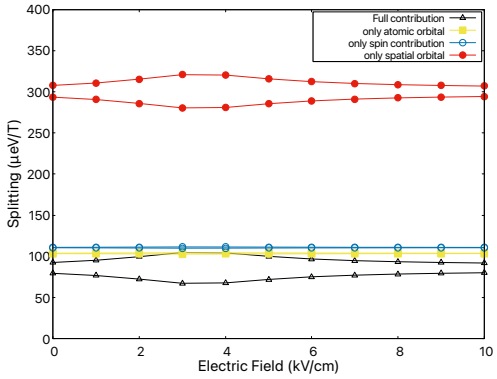

(a) 0% alloy, aligned dots

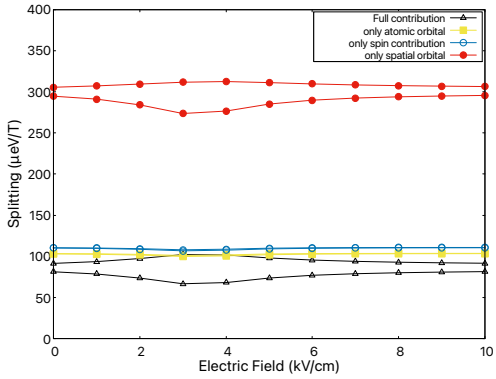

(b) 0% alloy, offset dots

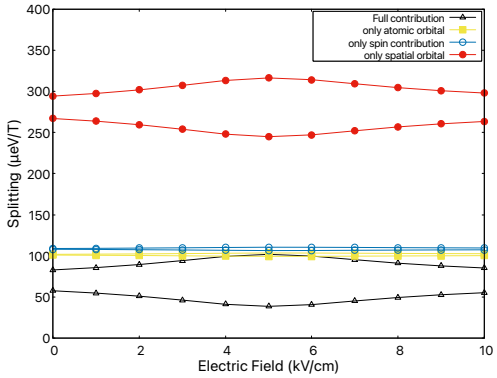

(c) 4% alloy, aligned dots

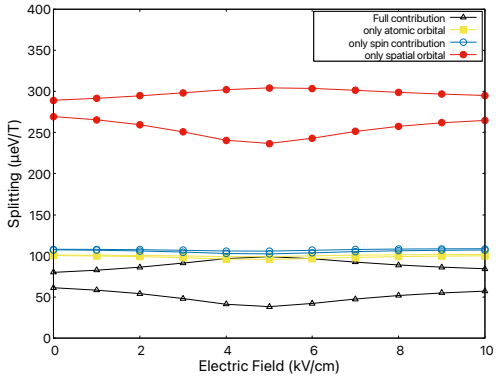

(d) 4% alloy, offset dots

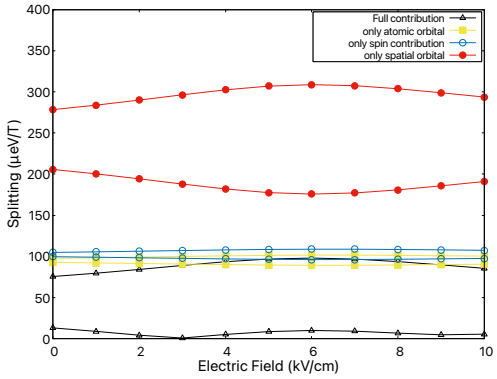

(e) 7% alloy, aligned dots

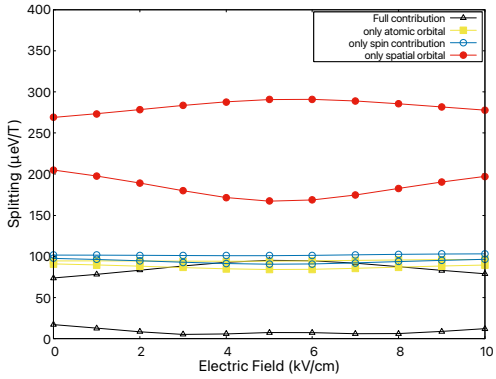

(f) 7% alloy, offset dots

Figure 6.17: Breakdown of splitting energy for each contribution of the perturbative Hamiltonian, for both aligned and offset dots at (a,b) 0%, (c,d) 4%, and (e,f) 7% alloy concentration. For offset dots, the true stacking axis of the dots is slightly off from the z-axis due to the offset. Thus, the offset QDMs dot not have azimuthal symmetry and are slightly misaligned with the magnetic field (applied perfectly along the z-direction), causing the slight asymmetry between the resonant structure of the bottom and top dots. The splitting is obtained with a magnetic field of 6 T in the z-direction. Due to the perturbative model, the splitting can be normalized and written as a linear response to the magnetic field strength in terms of $\mu\text{eV T}^{-1}$.

Figure 6.17 shows the three magnetic contributions to the splitting as the dots go through resonance. We see that the spin and atomic orbital contributions to the splitting remains unchanged as the electric field is scanned through resonance. The only term that contributes to the change in g-factor as the dots go through resonance is the Peierls term. Additionally, as we increase the alloy concentration, we have a stronger and wider resonance effect with the Peierls contribution, and, in turn, the total splitting strength. If we move away from resonance, we also see a clear drop in the intrinsic g-factor of the hole states. The combination of lower intrinsic g-factor and an enhanced resonance effect results in the Peierls contribution for 7% alloy to be less than the spin and atomic orbital contribution combined. As the sign of the sum of these three terms flip going into or out of resonance, the splitting energy crosses zero, unless, as is the case for offset dots, there is a anti-crossing. The same spin-mixing between inter-dot states of opposite spin, also contributes to a intra-dot spin-mixing between the two spin states of the same dot.

6.5.2 Peierls term, effective angular momentum, and spin

Given a constant magnetic field independent of $\vec{R}_n$, we can write an effective total spin, total atomic orbital angular momentum, and total angular momentum of the wavefunction from the Peierls term. The Hamiltonian of Eq. 6.7 summed over sites gives us

$$H^1(B) = \mu_B \left(2\vec{S}^{\text{tot}} + \vec{L}^{\text{tot}} - \vec{l}^{\text{eff}}\right) \cdot \vec{B}, \tag{6.8}$$

where $\vec{l}^{\text{eff}}$ is the effective spatial angular momentum of the hole states as calculated by the Peierls term. The choice of sign in front of $\vec{l}^{\text{eff}}$ is arbitrary. We have chosen a negative sign to represent $\vec{l}^{\text{eff}}$ being anti-aligned with $\vec{S}$ when the magnetic field is in the z direction. For unstrained dots, such as GaAs/AlAs or TB Hamiltonian with the

strain artificially removed, the confined states of a dot have an $\left|\vec{l}^{\text{eff}}\right|$ of 1, reflecting the characteristics of a heavy-hole. For single InAs dots in GaAs with identical geometry to the dots in this paper, the strain creates pocket potentials at the four corners of the dots, adding a nodal structure to the angular momentum and increasing $\left|\vec{l}^{\text{eff}}\right|$ to 3.

Figure 6.18 shows the calculated l_z^{eff} for our QDMs far off-resonance, where both the ground and excited state are confined to their respective dots, resulting in a similar $\vec{l}^{\text{eff}}$ for both. A key feature of flat disk shape dots is their strong confinement in the z-direction. This results in a strong preference for $\vec{l}^{\text{eff}}$ to be maximally aligned in the z-direction. Seen in Figure 6.18, if we rotate the magnetic field away from the z-direction, in this case towards the x-direction, $\vec{l}^{\text{eff}}$ does not follow the magnetic field. Furthermore, due to the spin-orbit interaction, the spin polarization is locked to the orbital motion of the wavefunction. Thus, the spin of the hole states also have a preference of being aligned in the z-direction and do not follow the magnetic field.

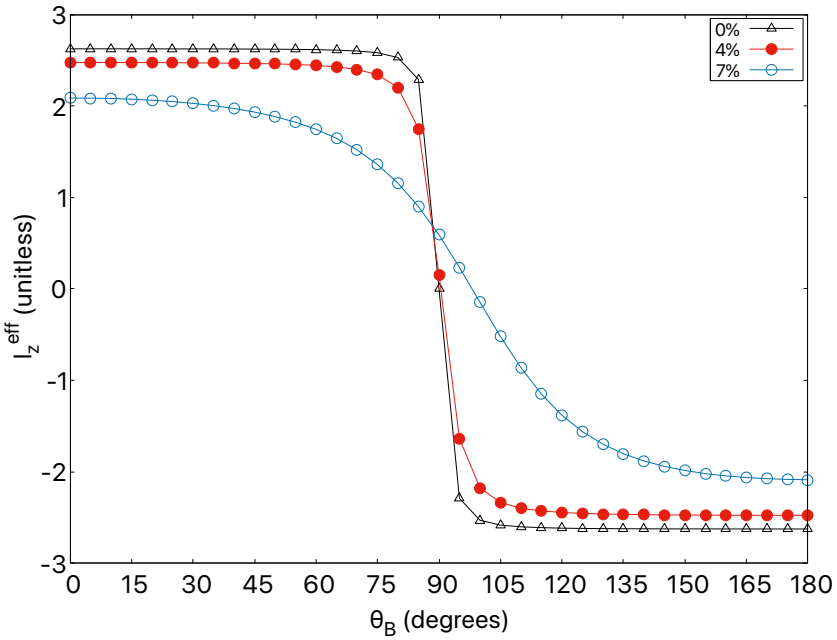

Figure 6.18: Off-resonance l_z^{eff} calculated with respect to the direction of the magnetic field. The natural, off-resonance, angular momentum from the Peierls contribution is similar for the ground and excited states. Off-resonance is defined as $-3\,\text{kV cm}^{-1}$, $-4.5\,\text{kV cm}^{-1}$, and $-16\,\text{kV cm}^{-1}$ for the 0%, 4%, and 7% alloy respectively.

In Figure 6.18, as alloy concentration is increased, l_{eff} decreases slightly, which contributes to the reduced intrinsic g-factor of the top and bottom dots found previously in Section 6.4. We also see that for higher alloy concentrations, the weaker confinement allow for $\vec{l}^{\text{eff}}$ to more freely follow the direction of the magnetic field. The same again is true for the spin, due to the spin-orbit interaction.

As the dots are brought to tunnel resonance, the ground state (lower energy hole state) forms a spatially symmetric wavefunction across the two dots, whereas the excited state (higher energy hole state) forms an anti-symmetric wavefunction. The ground state thus has a weaker confinement in the z direction, which "unlocks" the angular momentum from its z-alignment. The result is a weaker l_z^{eff} for all directions of magnetic field (Figure 6.19a). The anti-symmetric ground state, on the other hand, is now more confined and the l_z^{eff} increases as a result (Figure 6.19b).

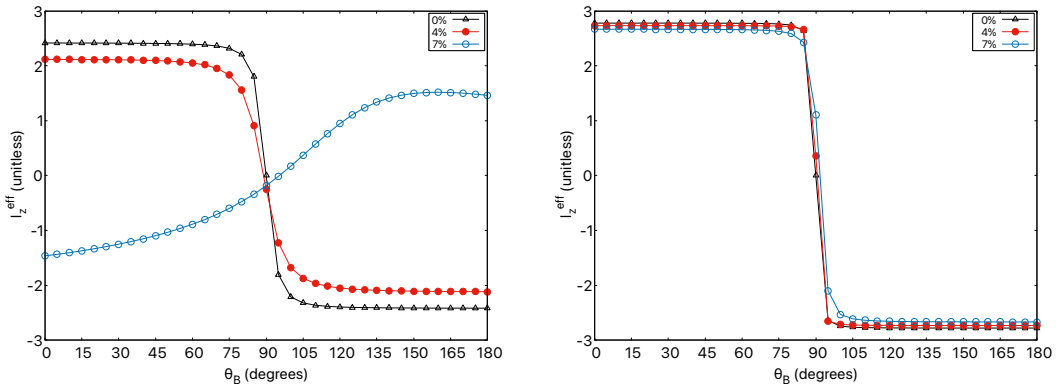

(a) Ground (symmetric) state (b) Excited (anit-symmetric) state

Figure 6.19: On-resonance l_z^{eff} calculated with respect to the direction of the magnetic field, for the a) ground and b) first excited hole states. On-resonance is defined as $3.4\,\text{kV}\,\text{cm}^{-1}$, $5.0\,\text{kV}\,\text{cm}^{-1}$, and $5.9\,\text{kV}\,\text{cm}^{-1}$ for the 0%, 4%, and 7% alloy case respectively.

Figure 6.19 also shows that, as the alloy concentration is increased, the resonance effect of "locking" and "unlocking" $\vec{l}^{\text{eff}}$ is also increased. The effect is drastic enough that, when the ground state of the 7% alloy case approaches resonance, l_z^{eff} is reduced to the point where alignment against the magnetic field becomes spin-dominant. With

the spin aligned with the magnetic field, $\vec{l}^{\text{eff}}$ is anti-aligned against the magnetic field, and thus picks up a negative sign, as seen in Figure 6.19a.

With a spin-orbit interaction, the resonance effects we see here for the l_{eff} is again observed for the spin. However, the overall change in spin polarization when in magnetic field is in the z-direction is minuscule compared to the change in $\vec{l}^{\text{eff}}$, thus there is not a noticeable change in splitting energy on the scale of Figure 6.17.

6.5.3 Spin-orbit effects and g-factor tuning

The spatial angular momentum and the spin are indirectly coupled by the spin-orbit interaction, and are thus respectively aligned or anti-aligned with the magnetic field. Without a spin-orbit interaction, the spin is no longer coupled to the angular momentum of the wavefunction nor the geometry of the dot. In which case, the spin is allowed to fully follow the direction of the magnetic field. The Peierls term also loses its resonance behavior. We can show such an effect by removing the spin-orbit interaction from the tight-binding Hamiltonian (scaling the physical SO parameter from 1 down to 0). The modified wavefunctions obtained from the TB Hamiltonian are then used as the basis states for calculating magnetic splitting with perturbation theory.

Figure 6.20 shows the total effective splitting as the SO interaction is turned off. As the SO interaction is turned off, the effective angular momentum of the wavefunction, l_{eff}, loses its alignment with the magnetic field, and thus the Peierls contribution to the splitting decreases. The spin, on the other hand, becomes less locked to the orbital geometry of the wavefunction and dots. The increased spin polarization increases the spin contribution to the splitting. At a given spin-orbit strength (around 30% of original strength), the combined spin and atomic orbital contributions equals that of the Peierls contribution. Below this transition point, the magnetic splitting

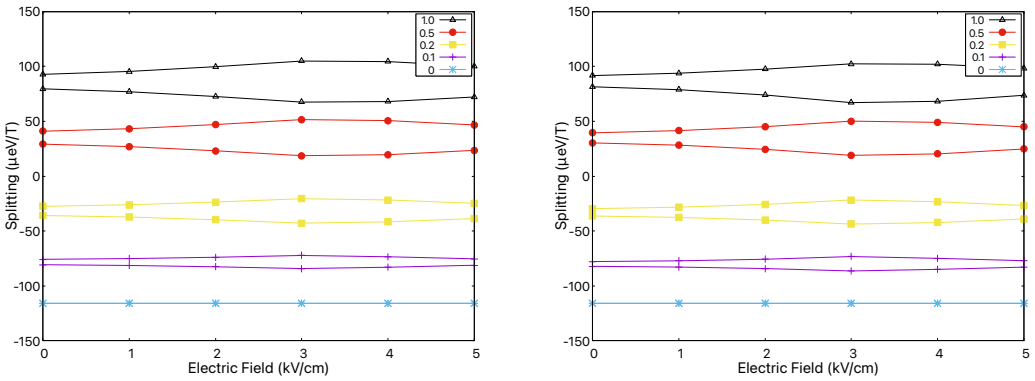

(a) Aligned dots

(b) Offset dots

Figure 6.20: Effective total splitting as spin-orbit interaction is turned off. The splitting is obtained with a magnetic field of 6 T in the z-directions. Due to the perturbative model, the splitting can be normalized and written as a linear response to the magnetic field strength in terms of $\mu\text{eV}\,\text{T}^{-1}$.

becomes spin dominant, and the ground state spin is parallel to the magnetic field (previously being anti-aligned). This switch in preferred spin alignment is represented by a negative value for the splitting energy.

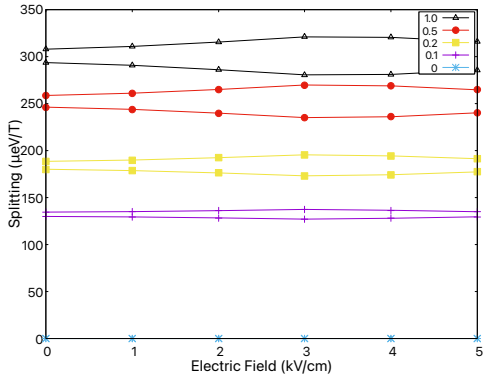

(a) Peierls contribution, aligned dots

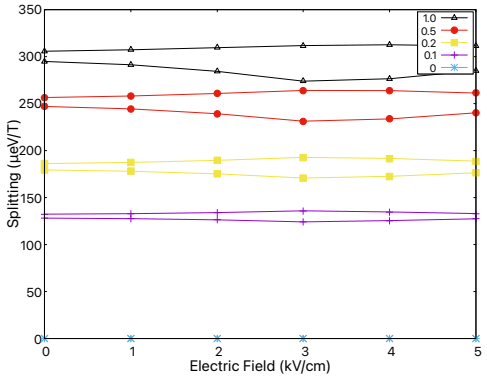

(b) Peierls contribution, offset dots

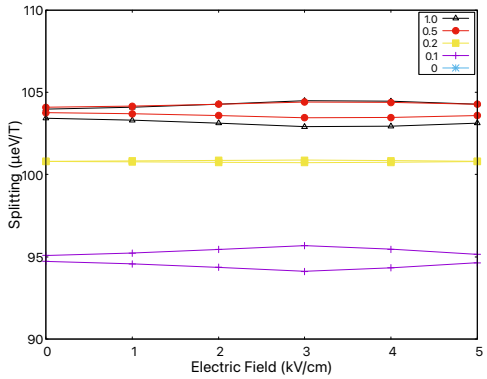

(c) Atomic orbital contribution, aligned dots

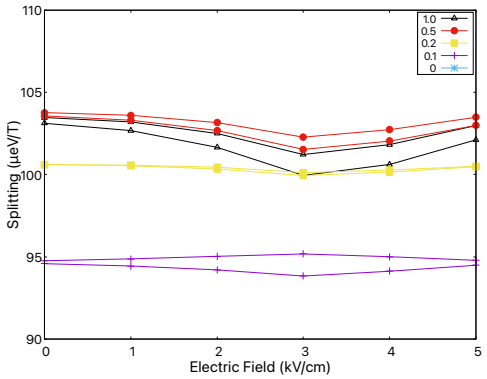

(d) Atomic orbital contribution, offset dots

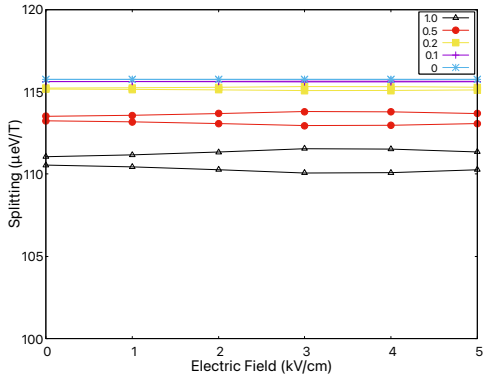

(e) Spin contribution, aligned dots

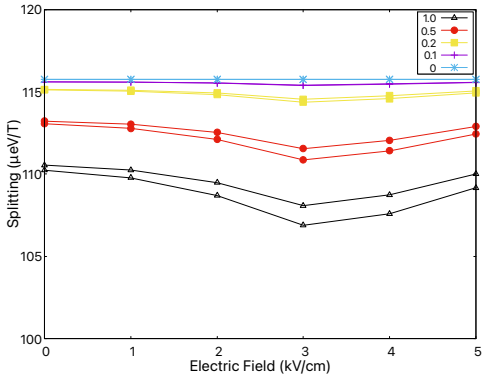

(f) Spin contribution, offset dots

Figure 6.21: Magnetic contributions to effective splitting as spin-orbit interaction is turned off. Note the different y-scale for the different contributions. The atomic orbital contribution is zero with zero spin-orbit coupling. The atomic orbital and spin contributions would have a relative sign to the Peierls contribution if preferred spin alignment was considered. The splitting is obtained with a magnetic field of 6 T in the z-directions. Due to the perturbative model, the splitting can be normalized and written as a linear response to the magnetic field strength in terms of $\mu\text{eV T}^{-1}$.

Figure 6.21a and Figure 6.21b show that the splitting from the Peierls term decreases as the spin-orbit interaction is turned off. The resonant effect of decreasing/increasing the splitting of the symmetric/anti-symmetric molecular state is also reduced as spin-orbit effects are turned off. The offset dots have an asymmetry in resonance behavior due to spin-mixing, which is also reduced as the spin is allowed to freely rotate as the SO interaction decrease. The splitting from the atomic orbitals show the same behavior as the Peierls splitting (Figure 6.21c and Figure 6.21d), but at a much smaller scale.

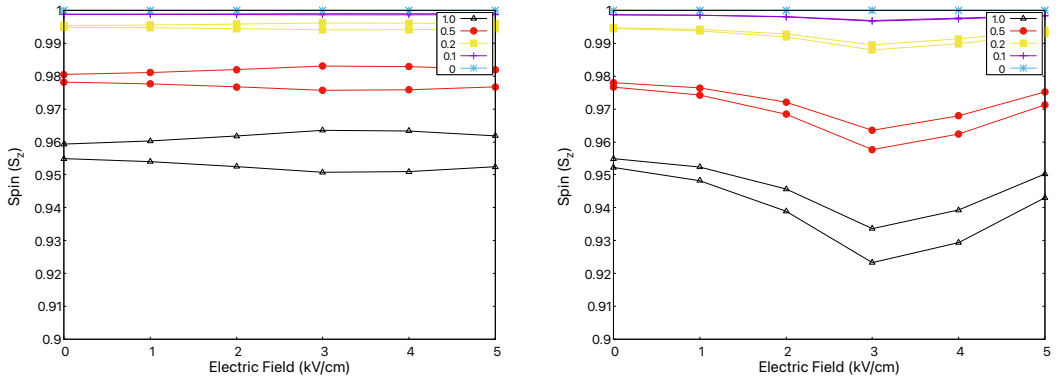

(a) Spin polarization, aligned dots

(b) Spin polarization, offset dots

Figure 6.22: Spin polarization of S_z as spin-orbit interaction is turned off.

As the SO interaction is turned off, the spin is able to freely rotate and is not constrained by the spatial geometry of the system. We see this both as the spin gains higher polarization (closer to 1) in the direction of the magnetic field (Figure 6.22), and as spin becomes the only contribution to magnetic splitting (Figure 6.21e and Figure 6.21f). If SO interaction is turned off completely, we see that the spin becomes fully polarized, even for the offset dots. Thus, without a spin-orbit interaction, we would not achieve spin-mixing in QDMs.

Chapter 7: Spin-texture and electric control of hole spin in single quantum dots

7.1 Textured spin and spin-locking

7.1.1 Spin-locking in strongly spin-orbit coupled materials

For a free particle, we expect the spin of the particle to follow the magnetic field. However, due to the strong spin-orbit interaction in III-V materials such as InAs, particularly for hole states, there is competition between alignment with the magnetic field, $\vec{B}$, and alignment with the spatial orbital motion of the wavefunction, $\vec{l}^{\text{eff}}$. For flat disk-shaped QDs that are much wider in the x and y-directions than in the z-direction, as are typically grown, hole states have much greater spatial angular momentum in the z-direction. Additionally, as we saw in the previous chapter, strain also greatly increases the spatial angular momentum of the wavefunction.

If the magnetic field is applied along the growth axis of the dot (the z-axis), as in the Faraday configuration, the magnetic field and $\vec{l}^{\text{eff}}$ are aligned. Locally, at the boundary of the dot, $\vec{l}^{\text{eff}}$ points perpendicular to the surface of the dot. This gives small amounts of spin at the sides of the dot where spin points away from the magnetic field. However, the overall characteristic of the hole spin is to be aligned with $\vec{l}^{\text{eff}}$ in the z-direction, and, in turn, anti-aligned with the magnetic field. Figure 7.1a shows this effect for "hemi-spherical" dots twice as wide as they are tall. For disk-shaped dots of height $4a$ and diameter $33.2a$, the effects of $\vec{l}^{\text{eff}}$ are even stronger.

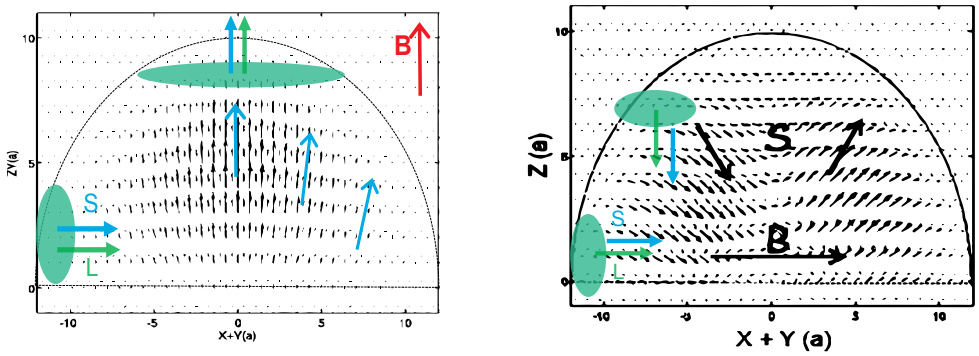

(a) Faraday (b) Voigt

Figure 7.1: Spin-texture, when the magnetic field is in the (a) Faraday or (b) Voigt configuration. Note the scale on the axes indicate the dots are more than twice as wide then they are tall.

As we rotate the magnetic field away from the z-direction, the spin stays mostly aligned with $\vec{l}^{\text{eff}}$. Figure 7.2 shows the z component of $\vec{l}^{\text{eff}}$ and $\vec{S}$ as the magnetic field is rotated along θ in the x-direction, for a disk-shaped dots of radii $12a$ and varying heights. We see that, for the flatter dots, $\vec{l}^{\text{eff}}$ and S_z have a reluctance to follow the magnetic field, with a sharp transition to entirely in x and y when the magnetic field reaches the xy-plane.

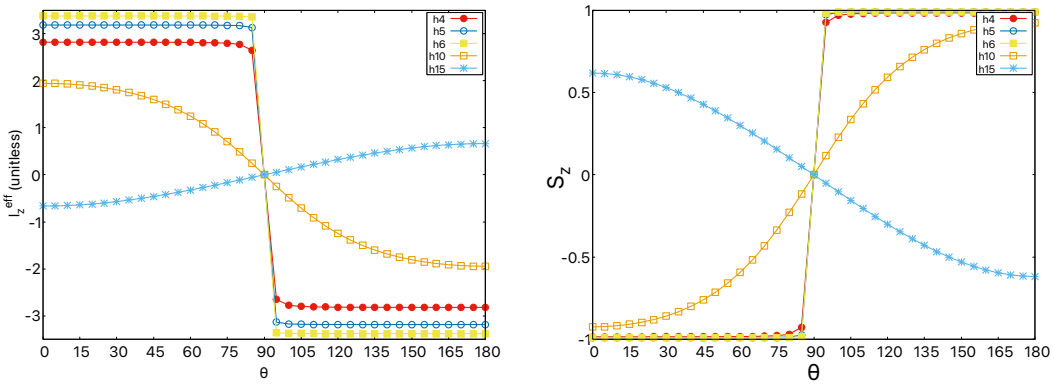

(a) Spatial angular momentum (b) Spin

Figure 7.2: z-component of (a) $\vec{l}^{\text{eff}}$ and (b) $\vec{S}$. Maximum spin is scaled to 1 for convenience. The magnetic field is rotated along θ in the x-direction, for a disk-shaped dot of radius $12a$ and varying height.

In the Voigt configuration (Figure 7.1b), where the magnetic field points in-plane of the width of the QD, the overall spin and spatial angular momentum of the hole state also points in-plane. However, locally, both are still influenced by the geometry of the dot. The flat shape of the dot causes the local spatial angular momentum to retain much of its polarization in the z-direction. The spin, due to the spin-orbit interaction, is also locally polarized in the z-direction. The result is a equal and opposite spatial distribution of the z-component of the spin between the two sides of the dot, where the overall spin in the z-direction cancels out to zero. The creation of the spin-texture thus satisfies the spin having to both align with the local spatial angular momentum and the overall symmetry requirement of a in-plane magnetic field.

7.1.2 Spatial distribution of hole spin

Figure 7.3 shows the direction of the spin at each atomic site, the spin-texture, for a magnetic field in the [110] direction. Here we see, that in addition to the equal and opposite spin in the z-direction created by the spin-texture, there is also a spatial distribution of spin in the x and y directions. Furthermore, the cylindrical dots, we find that two sides of the dot off-center from the axis of applied magnetic field (the $[\bar{1}10]$ and the $[1\bar{1}0]$ corners in the case of Figure 7.3), also have mirror symmetry and cancellation along the z-axis of the dot. The bottom half of the dot will have the spin distribution as shown in Figure 7.3, where as the the top half of the dot will have the spin at these two corners reversed (not shown).

Our goal for studying spin texture is to allow for electrical control of hole spin. By applying an in-plane electric field, we are able to bias the charge distribution towards one side or corner of the dot. The spin-texture created by the magnetic field is locked to the spatial geometry of the dots, and is not affected by the electric field. In biasing the charge density, we are able to move the hole state to acquire the

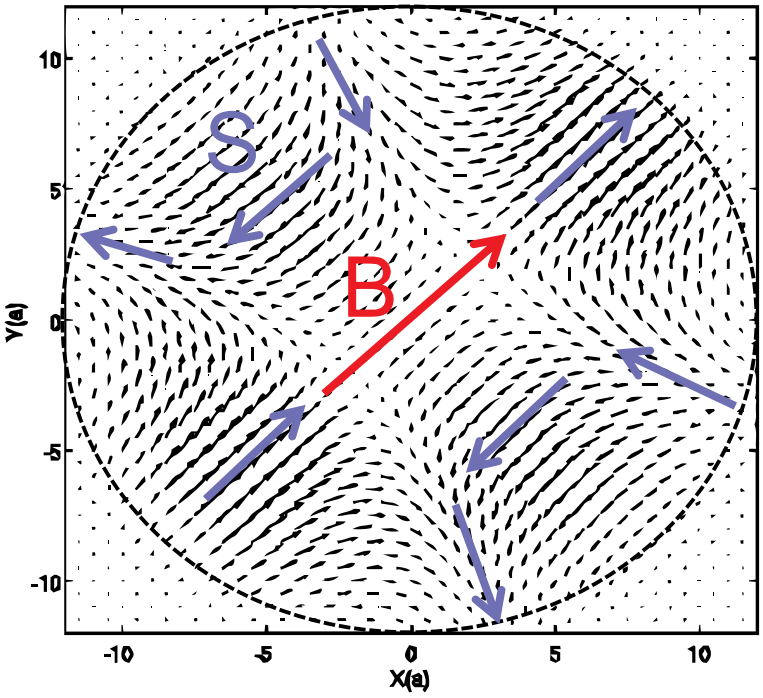

Figure 7.3: The $z = 0$ slice of the spin-texture in the xy-plane for the Voigt configuration.

spin polarization associated with different regions of the spin-texture. For example, applying an electric and magnetic field both in the [110] direction allows us to have spin polarized in the z-direction, despite both fields being in the xy-plane.

7.2 Electrical manipulation of spin under an in-plane magnetic field

We would like to use the properties of spin-texture, in conjunction with electric fields, as a novel protocol for manipulating hole spins. To do so properly, we should characterize the time evolution between spin states. However, direct exponentiation of large atomistic TB Hamiltonians is too computationally expensive. Such problems are often reduced to a g-tensor formalism,

$$H(\vec{B}) = H_0 + \mu_B \vec{S} \cdot \overleftrightarrow{g} \cdot \vec{B}, \tag{7.1}$$

where the g-tensor describes the response to a magnetic field, and semi-classical equations can be derived that describe the evolution of the state spin. $\vec{S}$, in a magnetic field. However, as we will see in the case of perpendicular electric and magnetic fields, the g-tensor model breaks down. For now, we analyze the static results of TB wavefunctions with different applied electric and magnetic fields to gain a better understanding of the underlying physics of spin-texture.

7.2.1 Parallel fields

Figure 7.4 shows the overall spin of the TB hole state, when the electric and magnetic field are both applied in the same direction, [110] in the case of Figure 7.4a and $\bar{1}10$ in the case of Figure 7.4b. The dot has a height of $4a$ including the wetting layer and a diameter of $33.2a$. The full TB calculation, with magnetic field included in the TB Hamiltonian, was performed to obtain the state from which the spin components are calculated. The S_z component at zero applied electric field is zero. The S_x and S_y components are small, but not zero, at zero electric field.

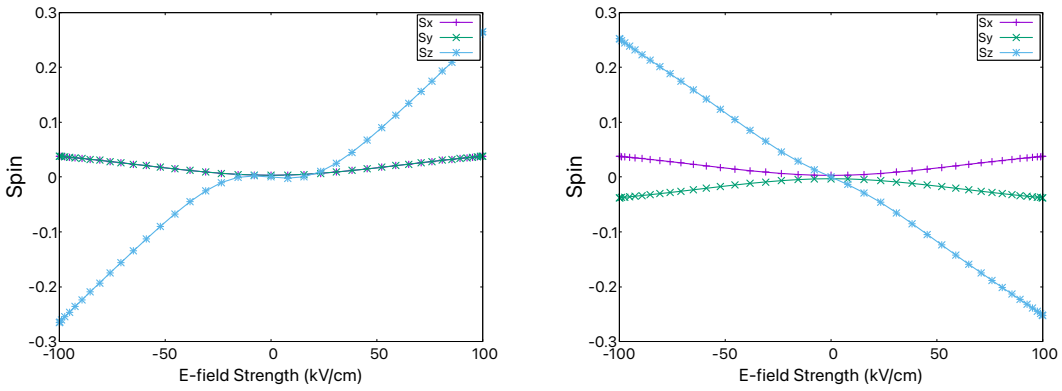

(a) $x + y$ (b) $-x + y$

Figure 7.4: Spin, under an electric field up to 100 kV cm^{-1} in (a) $x + y$ ([110]) (b) $-x + y$ ($\bar{1}10$). A magnetic field of 2 T is applied in the same direction of the electric field. Maximum spin is scaled to 1 for convenience.

The initial flat response in S_z is due to strain, causing the wavefunction to be more localized towards the edges of the dot. This effect is not present in unstrained dots such as AlAs in GaAs, or by artificially removing the strain during the construction of the TB Hamiltonian. The differing response for S_z when the fields are applied in [110] versus [$\bar{1}$10] is a result of the wetting layer breaking inversion symmetry. The S_x and S_y components are similar between the two cases, accounting for the direction of the magnetic field.

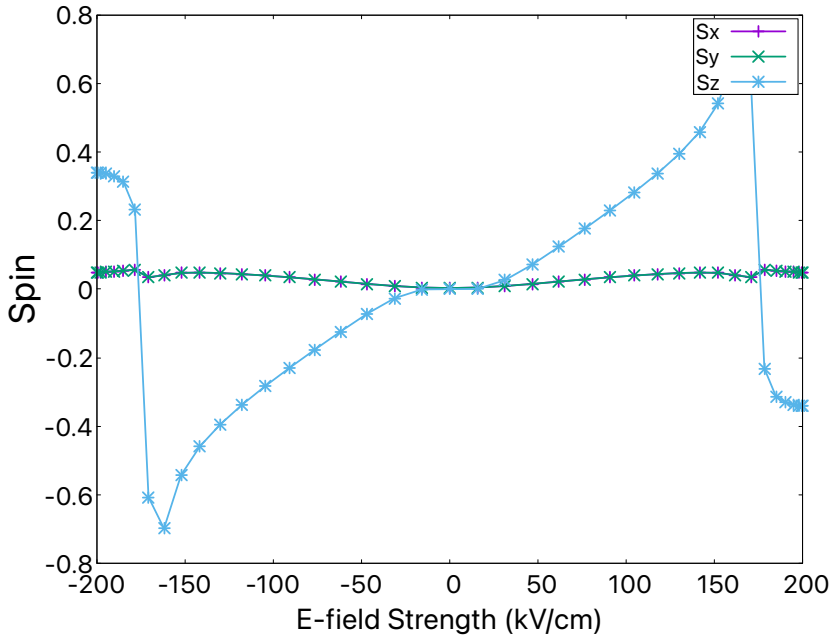

Figure 7.5: Spin, under an electric field up to 200 kV cm^{-1}. Both the electric field and the magnetic field of 2 T fields are in the [110] direction. Maximum spin is sclaed to 1 for convenience.

We were able to apply an electric field up to 161.8 kV cm^{-1} without the hole state leaking out of the dot. For the strained dots (Figure 7.5), the maximum spin-polarization in the z-direction was achieved with the hole density pushed up against the wall of the dot. For unstrained dots (not shown) the maximum polarization occurs before the state reaches the edge of the dot, at about 80 to 100 kV cm^{-1}, depending on the geometry of the dot. Curiously, Figure 7.5 seems to show spin in the

z-direction even after the wavefunction leaves the dot. We are not sure if this an interaction of the hole state with the edge of the dot from the outside or with the edge of the computational box. We have yet to study spin-texture outside the dots, in bulk material, or in 2D materials such as quantum wells.

7.2.2 Rotating electric field

A consequence of spin-texture is that we can flip the spin by applying an electric field in different directions. In the case where the electric and magnetic field are in the same direction, as shown previously, spin-flip in z can be achieved by reversing the direction of the electric field. The same spin-flip can be achieved by rotating the electric field. Figure 7.6 shows the spin polarization of the hole state, with different directions of electric field, while the magnetic field is held constant in the [110] direction.

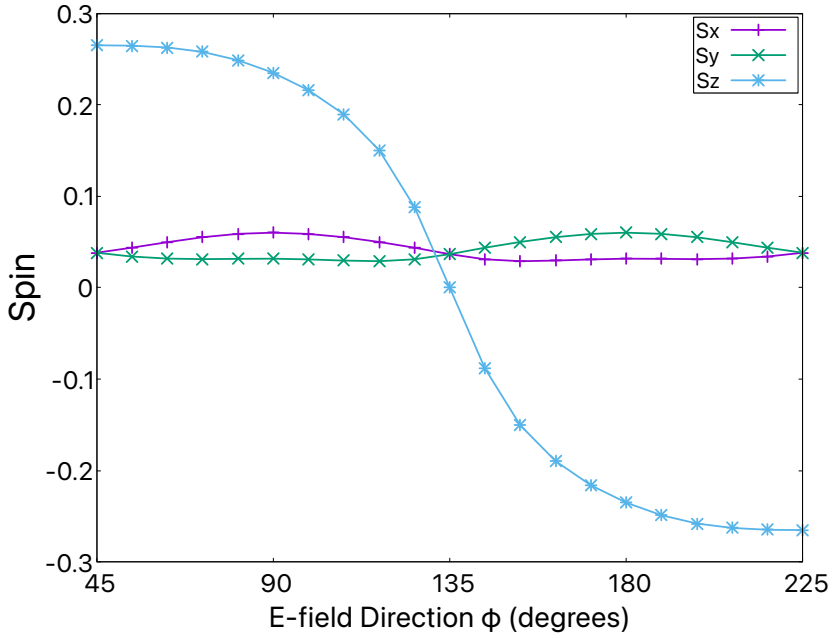

Figure 7.6: Spin, with a rotating electric field at $100\,\mathrm{kV\,cm^{-1}}$; 2 T magnetic field is static, pointing in the [110] direction. Maximum spin is scaled to 1 for convenience.

When the electric and magnetic fields are perfectly perpendicular, S_z is zero, as dictated by symmetry. There is always a positive amount of S_x and S_y, regardless

of the direction of the electric field. The direction for S_x and S_y, at the applied electric field of $100\,\mathrm{kV\,cm^{-1}}$, is anti-parallel to the magnetic field due to spin being the dominate response to magnetic field at this electrical bias. However, the spin may be parallel at smaller electric field strengths if other angular momenta, such as l^{eff}, is the dominate magnetic contribution.

7.2.3 Perpendicular fields

As alluded to earlier, applying in-plane electric fields perpendicular to the magnetic field is of special interest, as it can not be adequately described by the g-tensor model. Figure 7.7 shows the spin-components and the Zeeman splitting of a hole state with a magnetic field in the $[\bar{1}10]$ direction, and an electric field in the [110] direction.

First, we see a level crossing between an electric field strength of $58.8\,\mathrm{kV\,cm^{-1}}$ and $64.9\,\mathrm{kV\,cm^{-1}}$. There is a jump in the spin-components at this location. The Zeeman splitting energy is calculated as the energy difference between the two lowest energy hole states,and is thus always positive. Otherwise,we would see the Zeeman energy cross zero between $58.8\,\mathrm{kV\,cm^{-1}}$ and $64.9\,\mathrm{kV\,cm^{-1}}$. Above $65\,\mathrm{kV\,cm^{-1}}$, the spin of the lower energy hole state is anti-parallel to the direction of the magnetic field. Hole spins prefer to be anti-parallel to the magnetic field, but $\vec{l}^{\mathrm{eff}}$ causes the spins to prefer a parallel alignment. Anti-parallel alignment of the spin states with the magnetic field marks a region where spin effects are stronger than the spatial orbital angular momentum.

Under the g-tensor model,

$$\Delta E = \mu_B \vec{S} \cdot \overleftrightarrow{g} \cdot \vec{B}. \tag{7.2}$$

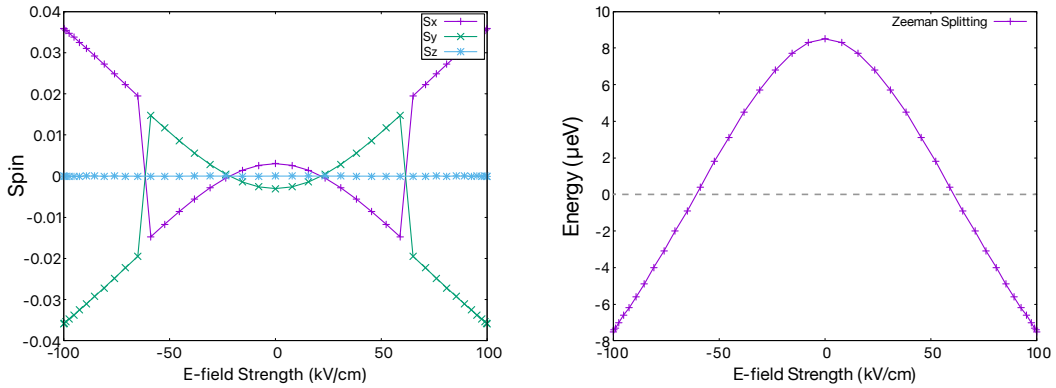

(a) Spin (b) Splitting

Figure 7.7: Spin and splitting, under an electric field up to $100\,\mathrm{kV\,cm^{-1}}$ in [110]; 2 T magnetic field static in $[\bar{1}10]$. Maximum spin is scaled to 1 for convenience.

We should be able to characterize zero splitting energy with a finite spin by setting $\overleftrightarrow{g}$ to be zero. However, between an electric field strength of $23.3\,\mathrm{kV\,cm^{-1}}$ and $30.9\,\mathrm{kV\,cm^{-1}}$, we have a finite splitting produced by no observable spin, unable to be produced with a g-tensor model. This is a result of, in addition to spin, having to consider other angular momenta present in the system.

7.3 Spin-orbit analysis of perpendicular fields

7.3.1 Component breakdown of spin and splitting energy

While unable to characterize the behavior of perpendicular fields with a g-tensor model, we are able to perform the analysis of magnetic contributions similar to the resonance effects on QDMs. This helps us understand what effects are attributed to spin-texture or to $\vec{l}^{\mathrm{eff}}$, and to show how both are attributed to spin-orbit interaction.

Calculations for Figure 7.8, Figure 7.9, and Figure 7.10 were performed with the full TB Hamiltonian, and not with a perturbative Hamiltonian. $\vec{l}^{\mathrm{eff}}$ can be interpreted as the first order approximation of the Peierls term. Due to the strong SO interaction of hole states (Figure 7.8), all three contributions show similar polarization strength

for each of the spin-components. Unlike the case for the QDMs, the magnetic field is now in the in-plane Voigt configuration, whereas it was previously in the Faraday configuration. The splitting strengths obtained are multiple orders of magnitude smaller. Since our program outputs energy to a resolution of 0.1 µeV, we start seeing stair-stepping and rounding errors for smaller values of splitting, such as for the splitting in Figure 7.8 when only atomic orbital contributions are considered.

For hole states, when only the spin contribution of the magnetic field is applied, we see the splitting energy crossover zero between $23.3\,\mathrm{kV\,cm^{-1}}$ and $30.9\,\mathrm{kV\,cm^{-1}}$, showing that the finite splitting when all three contributions are present is a result of angular momenta other than spin.

The level reordering present in the case where only the atomic orbitals are considered is unrelated to the one with all three contributions. The zero splitting at $58.8\,\mathrm{kV\,cm^{-1}}$ and $64.9\,\mathrm{kV\,cm^{-1}}$ is caused by the Peierls contribution counteracting the spin and atomic orbital contributions. As mentioned previously, $\vec{l}^{\mathrm{eff}}$ has the opposite preferred alignment with the magnetic field than that of the spin and atomic orbital terms. The splitting of the Peierls term thus carries a relative sign in comparison to the other two. The sum of the splitting of the three contributions is zero between $58.8\,\mathrm{kV\,cm^{-1}}$ and $64.9\,\mathrm{kV\,cm^{-1}}$. Above $65\,\mathrm{kV\,cm^{-1}}$, we see that the splitting from the spin contribution is the largest of the three, confirming the previous argument of spin being the most strongly coupled to the magnetic field based of the anti-alignment spin and magnetic field.

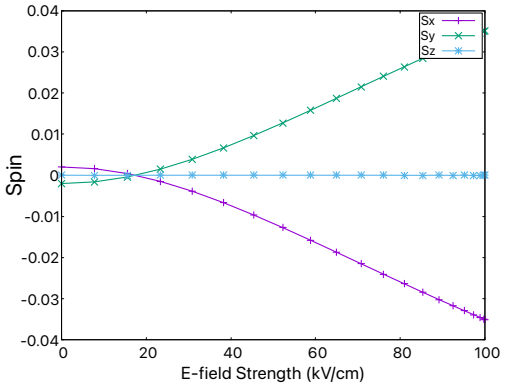

(a) Spin, Peirels only

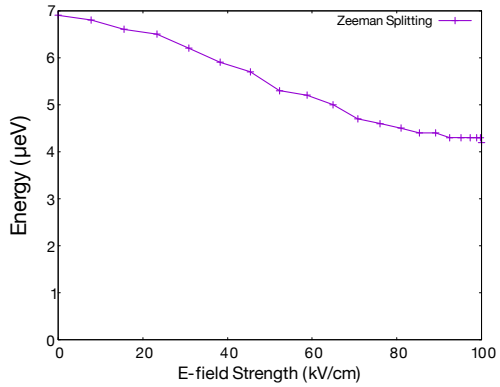

(b) Splitting, Peirels only

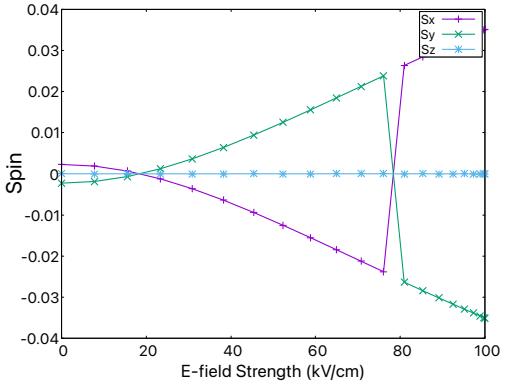

(c) Spin, atomic orbital only

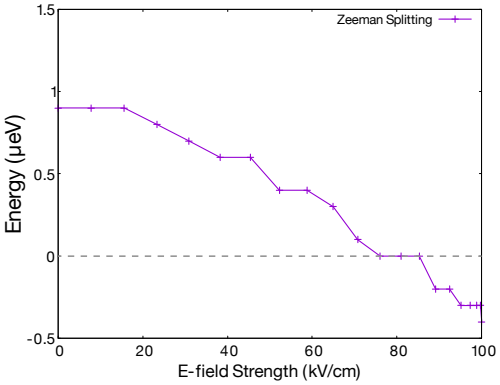

(d) Splitting, atomic orbital only

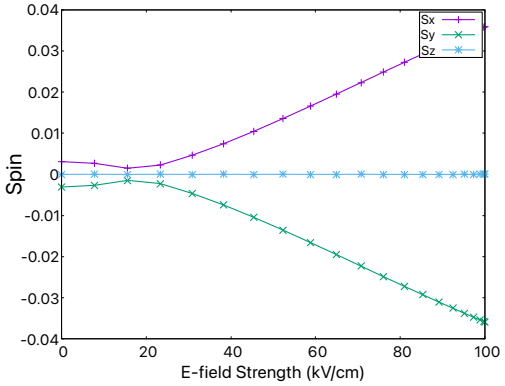

(e) Spin, spin only

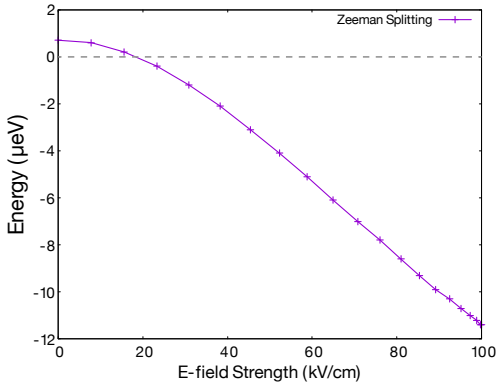

(f) Splitting, spin only

Figure 7.8: Breakdown of spin and Zeeman splitting energy for each contribution to the interaction with the magnetic field, for holes. The electric field is in the $x + y$ direction and the 2 T magnetic field is in the $-x + y$ direction. Maximum spin is scaled to 1 for convenience.

7.3.2 Weak spin-orbit coupling of electrons

Electrons (Figure 7.9) have weak SO coupling, not enough for spin texture, but enough for the Peierls contribution to align spins anti-parallel with the magnetic field, and the atomic orbital contribution to align spins parallel with magnetic field. Electron spin alone wants to be parallel with the magnetic field, and is always the strongest contribution to splitting energy between the three terms at 230.8 µeV. For all three cases, the spin is nearly at full polarization.

If preferred spin alignment with the magnetic field is taken into consideration, the splitting from the Peierls term has a relative sign with respect to the spin and atomic orbital contributions. This similar to the hole states, but with the preferred directions reversed. For both electrons and holes, the absolute value of the splitting energy from the Peierls contribution deceases slightly are the electrical bias is applied. Unlike holes, electrons do not have sufficient spin-orbit coupling to form spin-texture, and thus the the spin and atomic orbital contributions to the magnetic splitting remain constant.

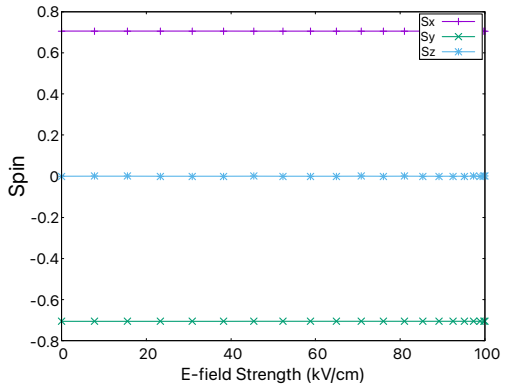

(a) Spin, Peirels only

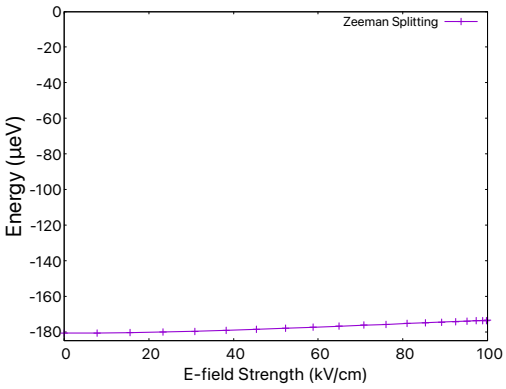

(b) Splitting, Peirels only

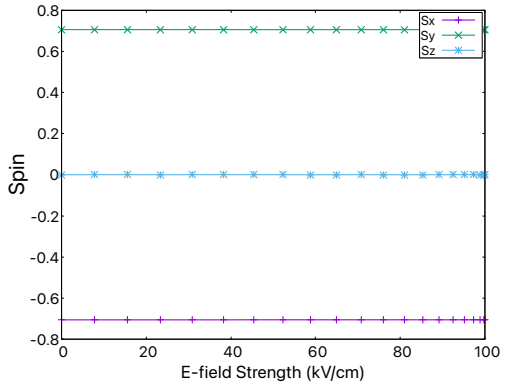

(c) Spin, atomic orbital only

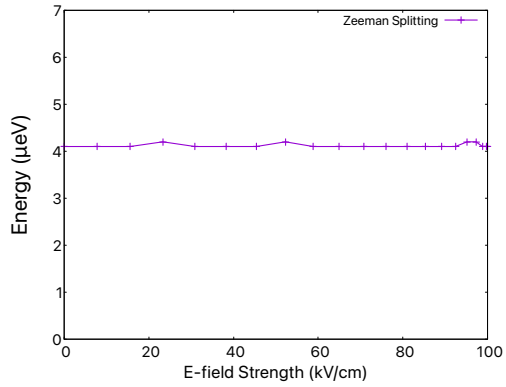

(d) Splitting, atomic orbital only

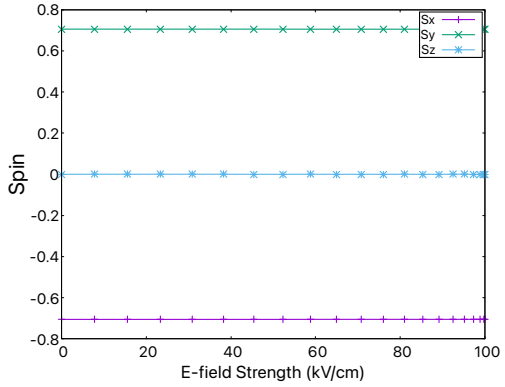

(e) Spin, spin only

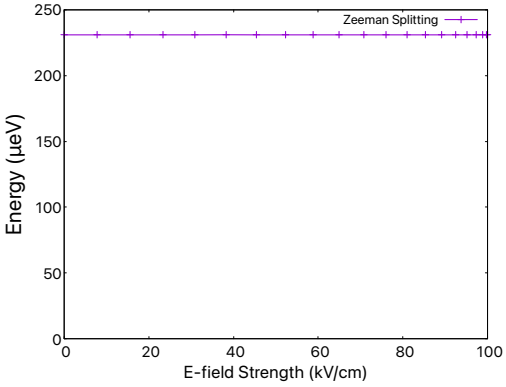

(f) Splitting, spin only

Figure 7.9: Breakdown of spin and Zeeman splitting energy for each contribution to the interaction with the magnetic field, for electrons. The electric field is in the $x+y$ direction and the 2 T magnetic field is in the $-x+y$ direction. Note the direction of alignment for the spin. Maximum spin is scaled to 1 for convenience. Numerical rounding effects are present in (d); the atomic orbital splitting and the spin splitting energies are otherwise constant.

7.3.3 Uncoupled spin and orbital

By removing the spin-orbit terms from the TB Hamiltonian entirely, both electrons and holes behave as free particles. Spin-texture is entirely removed. The Peierls term and the atomic orbitals no longer contribute to the splitting energy. Without a splitting to lift the degeneracy, the wavefunction is any linear combination of the two states of the spin-pair. S_x, S_y, and S_z are no longer valid quantum numbers, resulting in an uninformative plot for the spin (Figure 7.10a and Figure 7.10c.)

Figure 7.10 shows the results obtained for a hole state without spin-orbit interaction, but the results for electrons without spin-orbit interaction are identical, with the exception that the spin is parallel with magnetic field for the spin-only case. Both show a Zeeman splitting of 231.6 µeV.

We present such results as an incentive to study QDs in materials with strong spin-orbit coupling. Showing that spin-orbit coupling is necessary in generating the required spin-texture for electrical manipulation of the spin polarization.

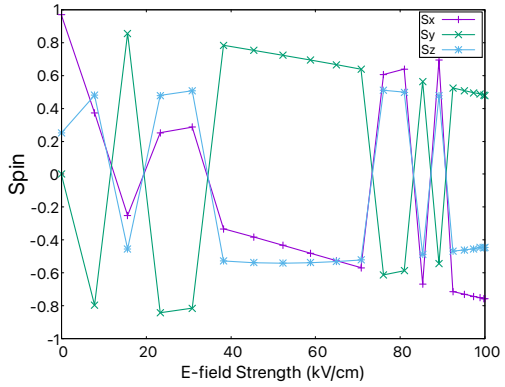

(a) Spin, Peierls only

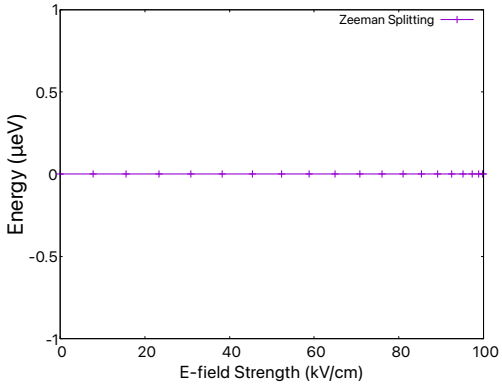

(b) Splitting, Peierls only

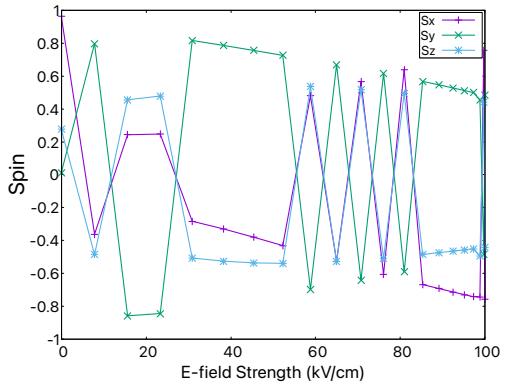

(c) Spin, atomic orbital only

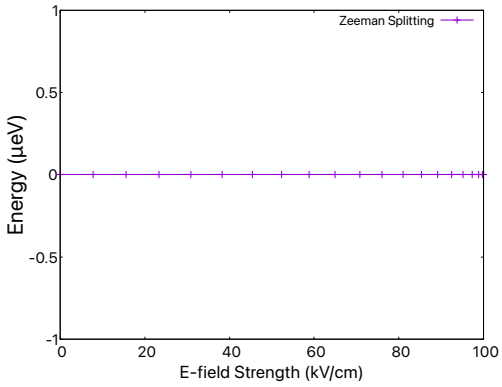

(d) Splitting, atomic orbital only

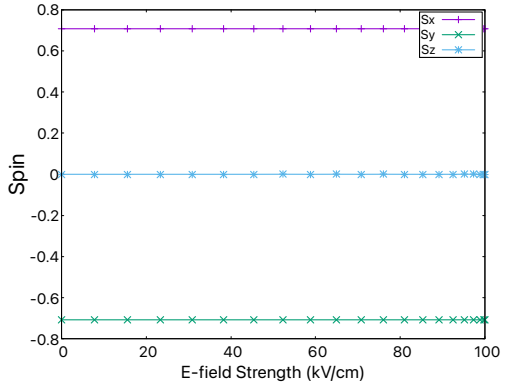

(e) Spin, spin only

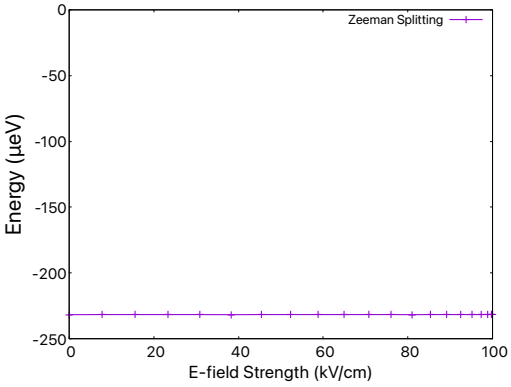

(f) Splitting, spin only

Figure 7.10: Breakdown of spin and Zeeman splitting energy for each contribution to the interaction with the magnetic field, for holes without spin-orbit interaction. The electric field is in the $x + y$ direction and the 2 T magnetic field is in the $-x + y$ direction. The results for spin are arbitrary when the state is degenerate. Maximum spin is scaled to 1 for convenience.

Chapter 8: Conclusion

Hole spins in self-assembled semiconductor quantum dots offer intriguing possibilities as potential qubit architectures. Hole spins in quantum dot molecules can be manipulated by indirect optical transitions to provide all-optical control of spin initialization, manipulation and readout. Initialization and manipulation requires hole states spin-mixed across the two dots of the QDM. In this thesis, we study how spin-mixing can be enhanced by engineering the GaAs inter-dot barrier to include dilute amounts of Bi. The alloyed GaBiAs barrier lowers the tunnel barrier for hole states, promoting dot-to-dot tunneling, and increases spin-orbit effects, contributing to spin-mixing in the system.

First, we investigated how to treat $GaBi_xAs_{1-x}$ alloys with an atomistic tight-binding model. Such an atomistic treatment was necessary to capture the band anti-crossing behavior of the GaBiAs valence band edge, and allowed for the modeling of alloy fluctuations and clustering effects. We also showed that a virtual crystal approximation for the alloy fails to describe the alloy adequately.

In an InAs QDM with a GaBiAs inter-dot barrier, we showed that the energies of electrons in the dots are not strongly dependent on the presence of Bi in the barrier nor to fluctuations in the alloy configuration. Hole state energies are not sensitive to the alloyed barrier at low alloy concentrations, aside from an increase in energy from the additional lattice strain imposed by the alloy. However, at higher concentrations, significant reductions in the hole state energies occur as the Bi concentration increases

in the barrier. This is due to both the loss of confinement as barrier height is reduced and the band repulsion as the barrier VBE approaches the dot hole states energies.

A three-fold increase in tunnel coupling strength is achieved when alloying the inter-dot region of a QDM with a $GaBi_{0.07}As_{0.93}$ alloy. At 7% alloy, the barrier energy is close to the dot energies while still allowing individual dot confinement of the hole states. The confinement of the hole states to the dot also protects the states from the configuration variances of a random alloy. The combined strain and orbital effects of the alloy increase the valence band edge of the GaBiAs barrier more than each individual effect in isolation. This carries over to the tunnel coupling strength between the two dots, as the dot hole states see a much lower tunnel barrier with the combined effects when compared to each individual effect. The result is a combined effect that is greater than the sum of the two individual effects. Additionally, we showed that the strain asymmetry in a fully alloyed barrier, caused by the Bi wrapping around the bottom dot, results in a larger zero-field energy difference between the top and bottom dots states. This increases the electric bias needed to bring the dots into resonance, but does not affect the tunneling behavior of the QDM. We also showed the alloy enhancement of tunnel coupling for various dot separations, as to find the optimal geometry for such devices. The $10a$ wetting layer to wetting layer distance presented in this paper provided a significant tunnel enhancement without entering the transition region where a bonding ground state switches with an anti-bonding ground state. The introduction of alloy significantly affects the heavy and light hole mixing governed by the spin-orbit effect, which is a key component of the bonding and anti-bonding reversal, and warrants further investigation.

An additional characteristic of spin-preserving tunnel coupling in QDMs is the asymmetric tunnel coupling strength dependent on the spin of the hole state, which governs the change in g-factor brought about when the dots are close to resonance.

However, the underlying physics of both the asymmetric tunnel coupling and the spin-mixing is driven by the spin-orbit effect, and both are greatly enhanced by the introduction of the alloyed barrier. Historically, diamagnetic effects were not considered of interest due to their relative weakness in comparison to Zeeman splitting. We have elected to include diamagnetic terms in our phenomenological Hamiltonian in order to better model the alloyed system. By adding diamagnetic corrections to the phenomenological 4×4 Hamiltonian, we were able to fit the energies of the TB wavefunction to obtain parameters for spin-mixing, tunnel coupling, g-factors, asymmetric tunneling, and the diamagnetic corrections. The 7% Bi barrier achieved a three-fold increase in the tunnel coupling and the spin-mixing strength. Additionally, the combined increase in resonance shift of the g-factor and the increased spin-mixing results in an observable intra-dot spin-mixing of hole states within the same dot. This opens the discussion for alternative methods of qubit manipulation, especially if the same parameter regime can be reached without introducing large amount of alloying.

Using a perturbative application of the magnetic field, we showed that all of the spin-dependent resonance behaviors in QDMs are dominated by the orbital angular momentum of the Peierls term. We further emphasis the relation between the spin-orbit coupling strength and the resonance behavior of QDMs, an aspect of QDMs that is hard to characterize experimentally. By scaling down or removing the spin-orbit interaction, we were able to decouple the Peierls term from the spin, removing the orbital contributions to the magnetic field splitting. With spin as the only contribution to the magnetic field splitting, all of the resonance effects of the QDM are removed. The same demonstration of the relationship between the spin-orbit effect and the resonance effects of the QDM can be performed for the spin-texture and spin-locking of in-plane magnetic fields. This thesis concluded with the use spin-texture created

by in-plane magnetic fields in conjunction with biasing the charge density with a in-plane electric field, to achieve an out-of-plane spin polarization in the z direction. In systems with sufficient spin-orbit strength, we propose the utilization of spin texture and electric fields as a novel method for rotating the spin in QDs.

In conclusion, we have successfully modeled InAs QDMs with $GaBi_xAs_{1-x}$ inter-dot barriers. We explored much of the underlying physics of the hole state resonance behaviors in QDMs. We have shown an sizable alloy enhancement to hole state spin-mixing, furthering the utility of QDMs as a viable qubit architecture. We have also shown a direct impact of spin-orbit coupling on the relationship between the spatial angular momentum of the wavefunction and hole spin, allowing for novel control of hole spins in strain grown QDs. In conclusion, we have laid the groundwork for further studies of alloyed materials in QDMs and for electrical control of hole spins in strong SO materials.

Appendix A: Alloy clustering and band anti-crossing in bulk GaBiAs

From February 2018 to April 2019, I mentored an undergraduate student, Jack Carlton, through the Department of Physics at the University of Maryland, College Park. We investigated the effects of Bi distribution in GaBiAs alloys. The work he performed under my supervision is compiled here.

Introduction for Appendix A

$GaBi_xAs_{1-x}$ is a semiconductor alloy that has yet to be fully explored. Bi-dilute $GaBi_xAs_{1-x}$ alloys are of particular interest for their potential applications in spintronics (quantum computing) and optoelectronics (photovoltaics). In spintronics, $GaBi_xAs_{1-x}$ is a proposed barrier for InAs QDs in a QDM system. In optoelectronics, $GaBi_xAs_{1-x}$ is useful in tunable semiconductor lasers and LEDs, as well as potentially for wavelength tailored photosensors. The key distinction for $GaBi_xAs_{1-x}$ semiconductor alloys is the ability to operate as semiconductor lasers in the infrared, as the energy band gap can be tuned to $\approx$1 eV.

Bi-dilute GaBiAs systems have been recently grown experimentally. Additionally, $GaBi_xAs_{1-x}$ semiconductors have shown natural clustering of Bi atoms in the grown lattice structures. This clustering has an effect on the semiconductor properties of $GaBi_xAs_{1-x}$ such as VBE and electron/hole wavefunctions. However, the behavior of $GaBi_xAs_{1-x}$ as a semiconductor of variable atom configuration with Bi clustering is

not well understood. As a result, we set out to explore these effects (configuration and concentration) on Bi-dilute $GaBi_xAs_{1-x}$ alloys.

Previous work has built a foundation for us to start. Kent and Zunger [29] explored the effects of atom configuration by studying small 64 atom lattices of N-dilute GaN_xP_{1-x} alloys, showing the effects of configuration on the conduction band edge (CBE) energy and the electron orbital wavefunction. Usman et al. [53] also explored the effects of atom configuration by editing lattices of 1000 to 8000 atoms of Bi-dilute $GaBi_xAs_{1-x}$. Both of these papers show clustering has a significant effect on the properties of the alloys. Thus, there is a need for a model that incorporates atomic configuration in determining the alloy properties of $GaBi_xAs_{1-x}$.

The goal of our research is to explore a statistical, spatial, atomistic model of $GaBi_xAs_{1-x}$ to view the effects of Bi clustering in lattices of 1000 to 8000 atom supercells. Our choice for this type of exploration is the atomistic sp^3s^* tight-binding model. The atomistic TB model allows us to construct a Hamiltonian (and solve for specific eigenstates) for any spatial atomistic configuration of a $GaBi_xAs_{1-x}$ lattice.

In this project, we define a cluster score to quantify the amount of clustering in a given alloyed lattice. We find a direct correlation between the amount of clustering and increase in VBE. Looking at the probability of the TB wavefunction to be at Bi sites, we also find a correlation between the total probability of the wavefunction on Bi sites and the total cluster score of the lattice. However, the individual site probabilities and the cluster scores of each atomic site show a weaker relationship. A statistical model of how the Bi is spatially distributed in the lattice, and relating it the spatial properties of the TB wavefunctions, would be a useful tool, that has yet to be developed.

A.1 Methods

To understand the effects of semiconductor lattice geometry on properties of the system as a whole, first, we develop a geometric, atomistic, representation of the lattice. We begin by creating a lattice file that contains the spatial information and atom type of a 1000 atom (unpadded) or 8000 atom (padded) lattice shaped in a cube. The lattice files are then edited in order to create a statistical distribution of Bi atoms. In the unpadded case, the affected region is the whole lattice; in the padded case, the affected region is a 1000 atom cube centered inside an 8000 atom GaAs cube. Then, given the bond length of GaAs and GaBi, the valence force field method is used to relax the atom positions of the atoms.

Using the TB parameters for GaBi and GaAs, in conjunction with the relaxed lattice file, we then construct a Hamiltonian that considers nearest neighbor interactions of s, p and s^* orbitals. Using the Arnoldi Method Package (included in ARPACK), the Hamiltonian is then partially diagonalized to obtain the states nearest to an user-inputted energy. This allows us to search for energy states of electrons and holes nearest the energy band gap; in other words, we find the conduction band edge (CBE) and valence band edge (VBE) of the lattice. Thus we can observe the effects of Bi concentration and Bi clustering on the VBE and CBE of each lattice. We choose to focus primarily on the effects on the VBE of each lattice.

As previously described, there are multiple ways to view clustering; we present both a qualitative and and quantitative approach. For the qualitative view, we create three distributions types: random (minimal clustering), Gaussian (maximum clustering), and "clustered" (an 'in between" clustering). Each type is a distribution of a given number of Bi atoms replacing As atoms in a GaAs lattice. The random distribution has no weights, and is generated by a pseudo-random number generator.

The Gaussian distribution favors replacements closer to the origin using probabilities given by a radial Gaussian function centered around the origin. The "clustered" distribution favors replacements near pre-existing Bi sites generated by an initial smaller random "seed" distribution of Bi atoms. Examples of the distributions are given in Figure A.1. Using these distributions, we construct a qualitative model for the effects of statistical clustering on the VBE and CBE of each lattice, thereby determining their effect on the energy band gap.

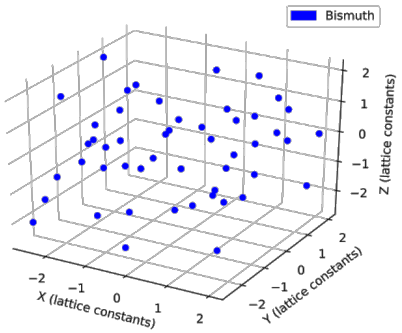

(a) Random

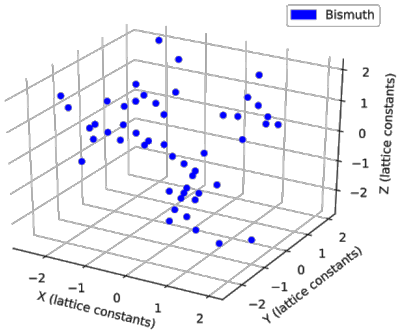

(b) Clustered

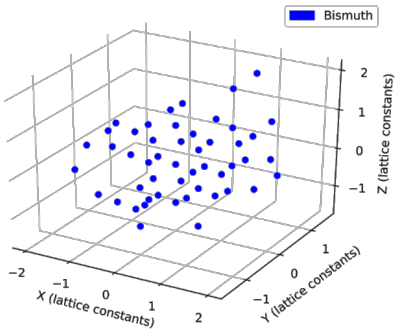

(c) Gaussian

Figure A.1: An example distribution of (a) random, (b) clustered, and (c) Gaussian GaBiAs alloys.

After the distributions are generated, they are characterized with a more quantitative description. For each atomic site i, we define a "site cluster score," δ_i:

$$\delta_i \equiv \sum_{j \in \mathrm{Bi}} |\boldsymbol{r}_i - \boldsymbol{r}_j|^{-1}, \tag{A.1}$$

characterizing how close the site i is to all Bi sites, j, in a lattice. For an overall lattice, we define a "cluster score," ρ, equal to the sum of all the site cluster scores of Bi atoms in the lattice,

$$\rho \equiv \sum_{i \in \mathrm{Bi}} \sum_{j \in \mathrm{Bi}} |\mathbf{r}_i - \mathbf{r}_j|^{-1}, \tag{A.2}$$

or

$$\rho = \sum_{i \in \mathrm{Bi}} \delta_i \tag{A.3}$$

where both i and j are atomic indices for all sites containing Bi. There are some limitations to this method of scoring, however. For example, there is not a one-to-one relationship between each lattice and ρ. Additionally, since the score is dependent on the number of Bi atoms, it does not accurately compare lattices of different Bi concentrations.

A.2 The effect of clustering on electron and hole state energies

For a qualitative comparison, we calculate energy states for the 1000 atom lattices with Bi concentrations $0 < x < 0.10$. For each distribution type, 10 different alloy configurations were developed. By comparing the average of these data sets (Figure A.2), we find as Bi clustering increases, the energy band gap decreases. This is effect apparent even at low concentrations (4%). The VBE broadens quicker in respect to x for more clustered distributions.

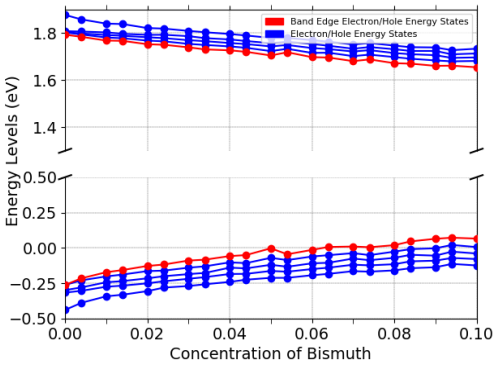

(a) Random

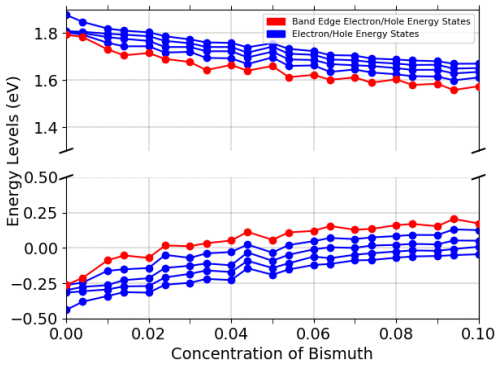

(b) Clustered

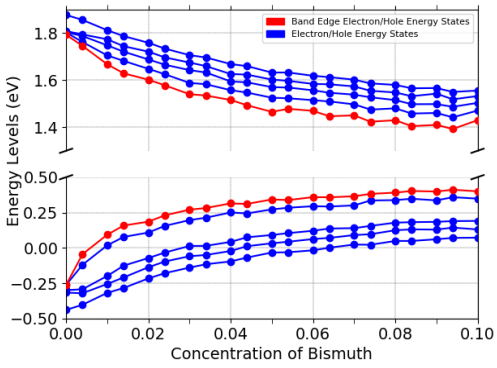

(c) Gaussian

Figure A.2: Average results of the CBE and VBE, up to a 10% alloy, of a (a) random, (b) clustered, and (c) Gaussian distribution of Bi. Concentration of Bi is labeled in terms of x, ranging from 0 to 1 for 0% to 100% alloy concentration.

From the energy state data, it is apparent that clustering has a notable effect on the VBE for nearly all concentrations of Bi. This shows the inaccuracy of other models used to predict the VBE, such as the virtual crystal approximation (VCA), which fails to consider the effects of clustering. Furthermore, when the VCA is used to produce a dataset of energy states for the 1000 atom lattices, the results do not agree with experiment, as they fail to capture the band anti-crossing (BAC) effects. Therefore, the VCA does not act as an accurate model for even "non-clustered" lattices.

We apply our quantitative method of comparison to a dataset of 346 lattices of $x = 0.07$. We plot highest valence state energy of each lattice configuration against

the calculated cluster score, ρ. Since each of our distribution types are statistically generated, it is unlikely any lattices generated will have the exact same distribution. As a result, lattices of the same "distribution type" can have different values for ρ. When plotting VBE energy vs ρ, the data shows more constructively the same conclusion as the qualitative comparisons – the VBE increases as the Bi clustering increases.

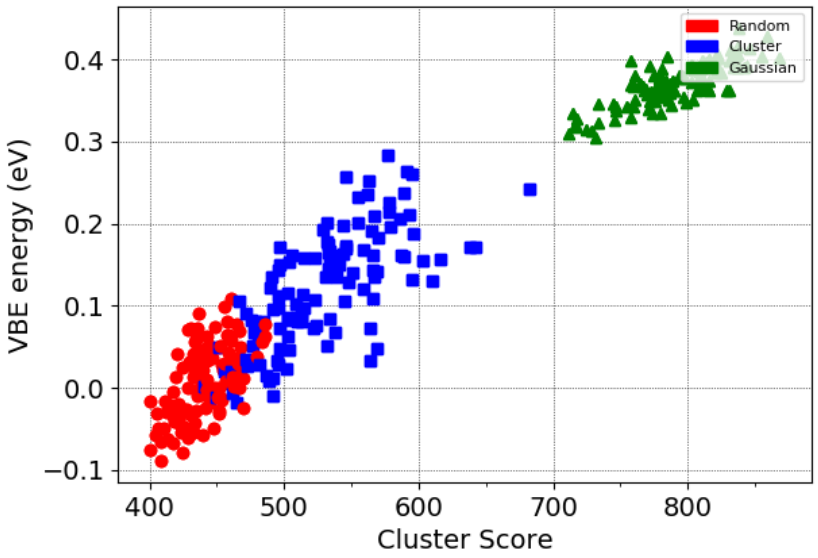

Figure A.3: Valence band energy versus alloy cluster score.

A.3 The effect of clustering on probability at Bi sites

A.3.1 Cluster score versus total probability at Bi sites

To further investigate the effects of Bi clustering, we compare the total spatial probability of hole states at Bi sites, β,

$$\beta \equiv \sum_{i \in \mathrm{Bi}} P_i = \sum_{i \in \mathrm{Bi}} \sum_{\alpha} a^*_{i,\alpha} a_{i,\alpha}, \tag{A.4}$$

where P_i is the wavefunction probability at site i, calculated from the sum of the probability amplitudes of the TB wavefunction, $a_{i,\alpha}$, for all TB orbitals, α, at site

i. Higher values of β imply more Bi influence, as a greater β is correlated with a greater VBE shift (Figure A.4). β is also systematically greater in our more clustered distributions. Therefore, we conclude that Bi clustering increases the total wavefunction probability at Bi sites.

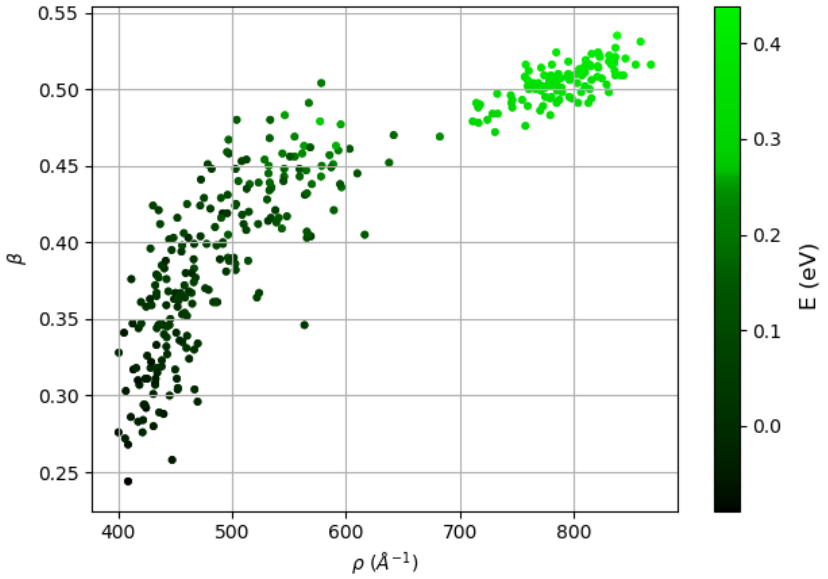

Figure A.4: Wavefunction probability at Bi sites versus cluster score. The color scale also shows the correlation of both β and ρ against VBE energy.

For further evidence, we take the 346 lattices of concentration $x = 0.07$ and use the VBE states to construct a plot of β vs. the cluster score ρ. We observe that larger values of β are correlated with larger values of ρ. In other words, alloy configurations with more bismuth clustering have a larger Bi influence than other configurations of the same Bi concentration. This result further supports that Bi clusters increase β.

A.3.2 Band anti-crossing versus total probability at Bi sites

All distribution types begin as pure GaAs (x = 0) lattices, therefore all share the same "starting point" for β. However, the difference types of alloy distribution

have a different rate of increase for β. We hypothesize that the "speed" of band broadening increases as lattices become more Bi-clustered. As the bands broaden, the Bi states underneath the GaAs VBE start to overlap, removing BAC effects of the alloy. In other words, the intersection between band anti-crossing and crossing region, playfully dubbed the "anti-crossing crossing crossing" (ACCC), should occur at smaller values of x for more clustered distributions.

To verify this theory, we use alloys generated iteratively; each lattice corresponding to the concentration, x, is built using a lattice of lower concentration, $x - 0.004$, as a seed. Iteratively generated alloys show the effect of small additions of Bi atoms without resorting to averaging over a large number of distributions at each concentration. Additionally, these lattices are padded with pure GaAs to form a 8000 atom lattice. This was done to reduce the effects of boundary conditions, which we found had little effect on the trend of our plots.

Figure A.5 shows 5 hole states closest to the gap, including the VBE state. In a traditional alloy, we expect the band edge state to have the most wavefunction probability at the Bi sites, with subsequent states having progressively less probability at the Bi sites. However, Bi-dilute GaBiAs has a BAC valence band, represented by a state with uncharacteristically high probability at the Bi sites (red in Figure A.5). As Bi concentration is increased, the alloy transitions into a traditional alloy. The point of the transition, the ACCC, occurs at lower alloy concentrations for distribution types that are more clustered.

A.4 The effect of clustering on spatial wavefunction behavior

In an effort to determine what causes the Bi clustering's global effects, we look on a local scale. We hypothesize that the wavefunction peaks will occur around more

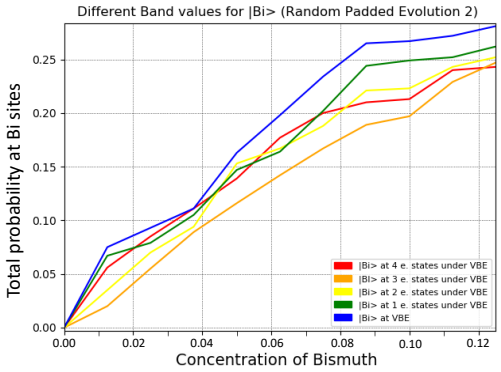

(a) Random

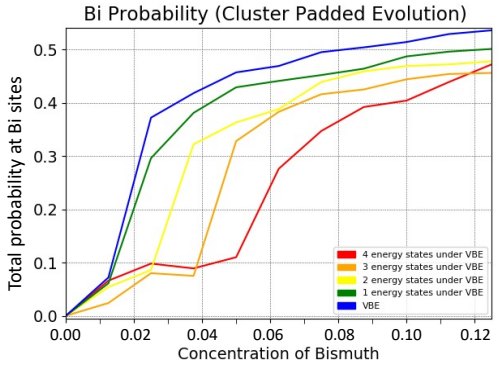

(b) Clustered

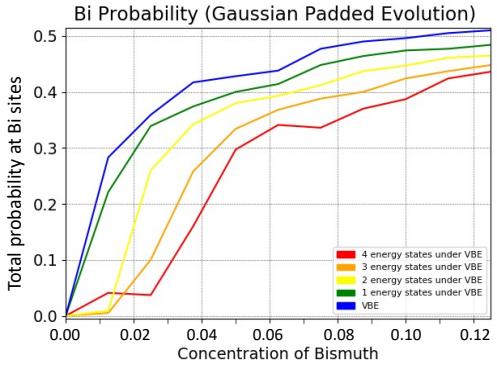

(c) Gaussian

Figure A.5: Portion of wavefunction at Bi sites for hole states closest to the gap, including the VBE state, plotted against alloy concentration, x, for (a) random, (b) clustered, and (c) Gaussian distributions of Bi. Note the difference on the y-scale

clustered Bi sites within the lattice. We observe the spatial probability for each atom site, P_i, by plotting the atoms on a 3D lattice with overall spatial wavefunction probability for a single hole state (not shown). From this, we are able to determine that wavefunction is highly localized at Bi sites. This is expected from our results concerning Bi probability (β) versus cluster score (ρ), where the Bi atoms, which represent only 7% of the anions, make up 24% of the wavefunction probability.

To directly observe the effect between clustering and probability, we use the site cluster score δ_i to represent the clustering information as one variable. We plotted the wavefunction probability per site, P_i, vs. the site cluster score, δ_i, as a final test.

We find that while there is certainly a correlation between δ_i and P_i, there seems to be a limit to the assumption where larger δ_i directly implies larger P_i. Sites that are more Bi-clustered do not necessarily imply larger wavefunction value at these sites.

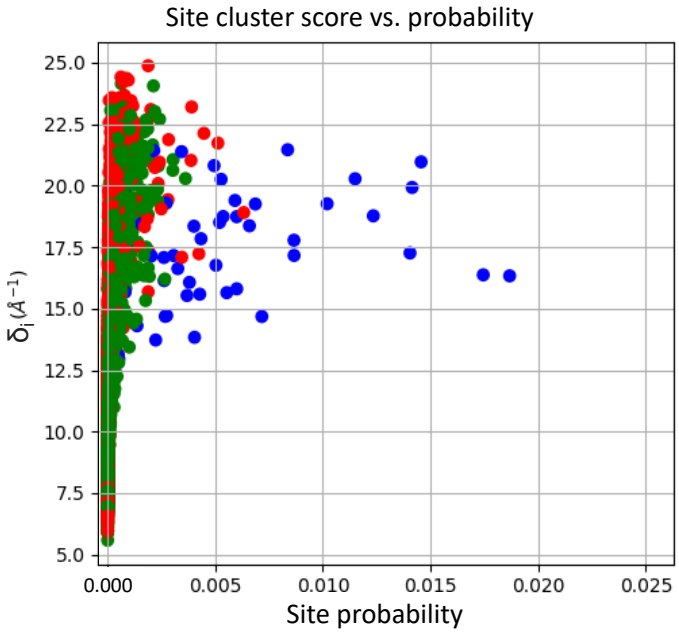

Figure A.6: Site cluster score versus probability. Red, Blue, and Green represent data from random, cluster, and Gaussian alloy distributions, respectively.

Conclusion for Appendix A

There is a need for a model to predict the behavior of Bi-dilute $GaBi_xAs_{1-x}$ alloys. Our methods show the VCA does not accurately predict hole energy states. We find that the VBE is largely dependent on alloy configuration, more specifically Bi clustering. By treating Bi clustering as a parameter we are able to support three separate hypothesis: (i) Lattices with greater Bi clustering yield higher energy VBE. (ii) Lattices with greater Bi clustering have higher total wavefunction probability on Bi sites. (iii) Lattices with greater Bi clustering have faster Bi band broadening, supporting the band anti-crossing model. While we have provided a lattice cluster score capable of describing the relation between the GaBiAs VBE the clustering

of Bi, more work needs to be done to characterize the spatial distribution of the wavefunction and the cluster score for each atomic site.

Appendix B: Full parameter set of effective Hamiltonian

Parameter fitting the TB energies to the 4×4 Hamiltonian is done in a two step process. The parameters for $E_{B/T}$ d, and t_0 are first fitted to a set of TB results calculated without a magnetic field, using the simple Hamiltonian

$$\begin{pmatrix} E_B & -t_0 \\ -t_0 & E_T + dF \end{pmatrix}. \tag{B.1}$$

If we were to reduce the 4×4 Hamiltonian at $B = 0$ to the 2×2 model, we would find $t_0^2 = t^2 + m^2$. Therefore to fit the remaining parameters, t is no longer a free parameter in the model, but calculated as $t = \mathrm{Sgn}(t_0)\sqrt{t_0^2 - m^2}$. t_0 and the other parameters obtained in the first step are not allowed to change between the fit of the $B = 0$ (2×2 Hamiltonian) model and the $B > 0$ (4×4 Hamiltonian) model.

By holding the parameters of the first step constant, we are able to fit individual magnetic field strengths without an overcomplete parameter set after the introduction of diamagnetic parameters. Since the parameters are set up to be independent of magnetic field strength, comparing fits for different magnetic field strengths allows us to confirm the validity of the parameters and assure that there are no hidden magnetic field dependencies unaccounted for in the model. One notable exception is the spin-mixing, m, for aligned dots with low alloy concentration. We believe the true value of m in these cases to be too small in comparison to the other parameters, resulting in a poor fit.

Table B.1: Fitted resonance parameters for **aligned** dots with a partially or fully alloyed barrier. t_0, E_B, E_T, and d_{eff} are not allowed to change after initial fit to the B =0 T TB results. t is a calculated value, based off the fit for t_0 and m. Magnetic field terms are scaled by the Bohr magneton to have units of μeV T^{-1} or μeV T^{-2}.

	t (meV)	m (μeV)	$\mu_B g_{12}$ (μeV T^{-1})	$\mu_B g_B$ (μeV T^{-1})	$\mu_B g_T$ (μeV T^{-1})	χ_B (μeV T^{-2})	χ_T (μeV T^{-2})
0% alloy							
B = 6T,12T,18T	−0.48	3.58±2.91	−9.38±0.03	42.44±0.05	40.85±0.05	1.32±0.00	1.35±0.00
B = 6T	−0.48	0.78±11.07	−9.64±0.02	43.68±0.04	42.06±0.04	1.24±0.01	1.52±0.01
B = 12T	−0.48	−0.05±0.59	−9.51±0.01	43.11±0.02	41.50±0.02	1.32±0.00	1.38±0.00
B = 18T	−0.48	3.19±1.78	−9.31±0.01	42.18±0.01	40.59±0.01	1.32±0.00	1.35±0.00
B = 24T	−0.48	−0.44±5.68	−9.03±0.00	40.91±0.01	39.35±0.01	1.31±0.00	1.32±0.00
partial 4% barrier							
B = 12T,18T	−0.60	0.56±19.13	−11.76±0.03	38.22±0.08	37.19±0.08	1.34±0.00	1.34±0.00
B = 12T	−0.60	19.31±1.50	−11.94±0.00	38.87±0.01	37.82±0.01	1.34±0.00	1.37±0.00
B = 18T	−0.60	−0.25±1.80	−11.68±0.01	37.95±0.02	36.92±0.02	1.34±0.00	1.34±0.00
partial 7% barrier							
B = 12T,18T	−0.76	69.58±4.36	−15.11±0.03	34.26±0.09	33.41±0.09	1.31±0.00	1.32±0.00
B = 12T	−0.76	68.41±1.92	−15.34±0.01	34.77±0.02	33.89±0.02	1.31±0.00	1.35±0.00
B = 18T	−0.76	52.04±1.11	−15.01±0.01	33.92±0.02	33.07±0.02	1.31±0.00	1.32±0.00
4% random alloy							
B = 6T,12T,18T	−0.77	83.47±3.64	−15.31±0.03	35.06±0.08	33.68±0.09	1.41±0.01	1.35±0.01
B = 6T	−0.78	66.70±3.50	−15.72±0.00	35.91±0.02	34.41±0.02	1.35±0.00	1.50±0.00
B = 12T	−0.77	81.23±1.17	−15.52±0.00	35.49±0.01	34.03±0.01	1.41±0.00	1.38±0.00
B = 18T	−0.78	62.81±0.99	−15.17±0.01	34.62±0.02	33.23±0.02	1.41±0.00	1.35±0.00
7% random alloy							
B = 6T,12T,18T	1.40	−126.21±15.67	26.28±0.05	22.83±0.08	19.55±0.08	1.46±0.00	1.30±0.00
B = 6T	1.41	−84.48±34.28	26.91±0.09	23.93±0.14	20.12±0.14	1.46±0.02	1.30±0.02
B = 12T	1.40	−104.33±23.98	26.59±0.07	23.38±0.11	19.82±0.11	1.47±0.01	1.31±0.01
B = 18T	1.40	−134.63±24.37	26.07±0.08	22.48±0.13	19.35±0.13	1.45±0.01	1.30±0.01

Table B.2: Fitted resonance parameters for **aligned** dots with fully alloyed barrier of ordered or clustered Bi distribution. t_0, E_B, E_T, and d_{eff} are not allowed to change after initial fit to the B =0 T TB results. t is a calculated value, based off the fit for t_0 and m. Magnetic field terms are scaled by the Bohr magneton to have units of μeV T^{-1} or μeV T^{-2}.

	t (meV)	m (μeV)	$\mu_B g_{12}$ (μeV T^{-1})	$\mu_B g_B$ (μeV T^{-1})	$\mu_B g_T$ (μeV T^{-1})	χ_B (μeV T^{-2})	χ_T (μeV T^{-2})
3% ordered alloy							
$B = 12$T,18T	−0.64	0.12±4.86	−12.59±0.02	38.16±0.03	36.76±0.03	1.37±0.00	1.31±0.00
$B = 12$T	−0.64	33.90±0.98	−12.78±0.00	38.81±0.01	37.41±0.01	1.38±0.00	1.32±0.00
$B = 18$T	−0.64	2.03±0.80	−12.51±0.01	37.89±0.01	36.50±0.01	1.37±0.00	1.31±0.00
6% ordered alloy							
$B = 12$T,18T	−0.86	136.09±4.16	−17.84±0.02	34.21±0.06	30.91±0.06	1.46±0.00	1.30±0.00
$B = 12$T	−0.86	139.04±3.27	−18.10±0.01	34.75±0.03	31.38±0.03	1.48±0.00	1.31±0.00
$B = 18$T	−0.86	124.42±2.58	−17.71±0.01	33.91±0.03	30.61±0.04	1.46±0.00	1.30±0.00
3% clustered alloy							
$B = 12$T,18T	−0.70	41.09±2.66	−13.62±0.03	37.00±0.05	34.31±0.05	1.37±0.00	1.31±0.00
$B = 12$T	−0.70	45.62±1.31	−13.83±0.00	37.57±0.01	34.83±0.01	1.38±0.00	1.32±0.00
$B = 18$T	−0.70	27.46±0.79	−13.53±0.01	36.69±0.01	34.00±0.01	1.37±0.00	1.30±0.00
4% clustered alloy							
$B = 12$T,18T	−0.78	65.97±4.76	−15.31±0.03	34.98±0.05	32.67±0.05	1.39±0.00	1.33±0.00
$B = 12$T	−0.78	58.43±2.15	−15.55±0.01	35.53±0.01	33.14±0.01	1.40±0.00	1.34±0.00
$B = 18$T	−0.78	49.52±1.36	−15.21±0.01	34.68±0.01	32.36±0.01	1.38±0.00	1.33±0.00
6% clustered							
$B = 12$T,18T	1.06	240.28±7.48	21.54±0.03	28.91±0.07	27.36±0.08	1.43±0.00	1.32±0.00
$B = 12$T	1.06	221.56±7.38	21.83±0.02	29.38±0.05	27.68±0.06	1.45±0.00	1.34±0.00
$B = 18$T	1.06	234.68±5.76	21.39±0.02	28.66±0.06	27.11±0.06	1.43±0.00	1.32±0.00
7% clustered							
$B = 12$T,18T	1.24	−245.21±8.94	25.36±0.05	23.76±0.13	23.89±0.15	1.42±0.01	1.38±0.01
$B = 12$T	1.25	−233.12±8.49	25.76±0.04	24.47±0.11	24.07±0.13	1.44±0.01	1.40±0.01
$B = 18$T	1.24	−247.58±10.63	25.18±0.06	23.47±0.15	23.78±0.18	1.42±0.01	1.38±0.01

Table B.3: Fitted resonance parameters for dots **offset** by $2a$ in the x direction, with a partially or fully alloyed barrier. t_0, E_B, E_T, and d_{eff} are not allowed to change after initial fit to the $B = 0$ T TB results. t is a calculated value, based off the fit for t_0 and m. Magnetic field terms are scaled by the Bohr magneton to have units of μeV T^{-1} or μeV T^{-2}.

	t (meV)	m (μeV)	$\mu_B g_{12}$ (μeV T^{-1})	$\mu_B g_B$ (μeV T^{-1})	$\mu_B g_T$ (μeV T^{-1})	χ_B (μeV T^{-2})	χ_T (μeV T^{-2})
0% alloy							
B = 6T,12T,18T	−0.40	91.71±0.71	−8.86±0.03	42.74±0.04	41.07±0.04	1.31±0.00	1.35±0.00
B = 6T	−0.41	89.97±1.00	−9.18±0.02	43.94±0.04	42.24±0.04	1.22±0.01	1.52±0.01
B = 12T	−0.40	93.38±0.16	−9.04±0.01	43.43±0.02	41.74±0.02	1.31±0.00	1.38±0.00
B = 18T	−0.40	93.41±0.37	−8.78±0.01	42.48±0.02	40.82±0.06	1.31±0.00	1.34±0.00
B = 24T	−0.40	98.91±0.31	−8.46±0.00	41.18±0.01	39.55±0.01	1.30±0.00	1.32±0.00
partial 4% barrier							
B = 12T,18T	−0.50	117.38±0.62	−11.08±0.02	38.39±0.04	37.53±0.04	1.33±0.00	1.33±0.00
B = 12T	−0.50	120.53±0.20	−11.33±0.01	39.12±0.02	38.25±0.02	1.33±0.00	1.36±0.00
B = 18T	−0.50	120.06±0.25	−11.01±0.01	38.22±0.02	37.37±0.02	1.33±0.00	1.33±0.00
partial 7% barrier							
B = 12T,18	−0.64	152.40±1.14	−14.35±0.03	34.29±0.08	33.55±0.08	1.31±0.00	1.31±0.00
B = 12T	−0.64	154.83±0.41	−14.63±0.01	34.83±0.01	34.09±0.01	1.31±0.00	1.34±0.00
B = 18T	−0.64	151.37±0.11	−14.23±0.00	33.97±0.01	33.22±0.01	1.31±0.00	1.31±0.00
4% random alloy							
B = 6T,12T,18T	−0.66	173.65±1.23	−14.51±0.03	35.86±0.08	33.07±0.08	1.41±0.01	1.34±0.01
B = 6T	−0.66	171.18±1.06	−15.01±0.01	36.83±0.02	33.88±0.02	1.34±0.00	1.49±0.00
B = 12T	−0.66	174.05±0.21	−14.76±0.00	36.35±0.01	33.43±0.01	1.41±0.00	1.36±0.00
B = 18T	−0.66	171.52±0.08	−14.34±0.00	35.44±0.01	32.59±0.01	1.41±0.00	1.33±0.00
7% random alloy							
B = 6T,12T,18T	1.20	−315.59±7.64	24.79±0.05	23.31±0.08	19.85±0.09	1.47±0.00	1.26±0.00
B = 6T	1.20	−296.65±15.18	25.63±0.08	24.45±0.14	20.54±0.17	1.49±0.02	1.23±0.02
B = 12T	1.20	−306.50±10.18	25.21±0.06	23.87±0.10	20.20±0.12	1.48±0.01	1.27±0.01
B = 18T	1.20	−318.36±9.97	24.52±0.06	22.97±0.10	19.58±0.12	1.47±0.00	1.26±0.00

Table B.4: Fitted resonance parameters dots **offset** by $2a$ in the x direction, with fully alloyed barrier of ordered or clustered Bi distribution. t_0, E_B, E_T, and d_{eff} are not allowed to change after initial fit to the B =0 T TB results. t is a calculated value, based off the fit for t_0 and m. Magnetic field terms are scaled by the Bohr magneton to have units of μeV T^{-1} or μeV T^{-2}.

	t (meV)	m (μeV)	$\mu_B g_{12}$ (μeV T^{-1})	$\mu_B g_B$ (μeV T^{-1})	$\mu_B g_T$ (μeV T^{-1})	χ_B (μeV T^{-2})	χ_T (μeV T^{-2})
3% ordered alloy							
B = 12T,18T	−0.54	130.53±0.67	−11.89±0.02	38.53±0.03	37.00±0.03	1.36±0.00	1.31±0.00
B = 12T	−0.54	135.02±0.07	−12.14±0.00	39.15±0.00	37.62±0.00	1.37±0.00	1.32±0.00
B = 18T	−0.54	132.88±0.05	−11.80±0.00	38.25±0.00	36.73±0.00	1.36±0.00	1.31±0.00
6% ordered alloy							
B = 12T,18T	−0.73	209.08±1.67	−16.86±0.02	34.28±0.05	30.84±0.05	1.44±0.00	1.30±0.00
B = 12T	−0.72	213.45±0.82	−17.19±0.01	34.88±0.02	31.37±0.02	1.45±0.00	1.31±0.00
B = 18T	−0.73	205.84±0.52	−16.71±0.01	33.98±0.02	30.55±0.02	1.44±0.00	1.30±0.00
3% clustered alloy							
B = 12T,18T	−0.60	137.01±0.79	−13.03±0.03	37.50±0.04	34.61±0.04	1.38±0.00	1.31±0.00
B = 12T	−0.62	140.91±0.17	−13.29±0.00	38.10±0.01	35.16±0.01	1.39±0.00	1.32±0.00
B = 18T	−0.60	137.86±0.08	−12.93±0.00	37.21±0.00	34.32±0.01	1.37±0.00	1.30±0.00
4% clustered alloy							
B = 12T,18T	−0.67	161.70±1.24	−14.64±0.03	35.52±0.05	32.84±0.05	1.40±0.00	1.32±0.00
B = 12T	−0.67	163.76±0.33	−14.93±0.00	36.11±0.01	33.37±0.01	1.41±463 071.00	1.33±0.00
B = 18T	−0.67	160.29±0.15	−14.52±0.00	35.23±0.01	32.55±0.01	1.40±0.00	1.32±0.00
6% clustered							
B = 12T,18T	−0.91	279.85±4.25	−20.48±0.03	28.96±0.07	26.79±0.07	1.46±0.00	1.29±0.00
B = 12T	−0.91	280.21±2.42	−20.88±0.01	29.52±0.03	27.28±0.03	1.47±0.00	1.30±0.00
B = 18T	−0.91	274.64±1.77	−20.29±0.01	28.68±0.03	26.51±0.03	1.45±0.00	1.29±0.00
7% clustered							
B = 12T,18T	1.05	−324.59±11.20	24.19±0.10	23.56±0.21	23.34±0.25	1.47±0.01	1.32±0.01
B = 12T	1.06	−316.15±27.52	24.77±0.23	24.17±0.48	23.58±0.60	1.50±0.04	1.34±0.04
B = 18T	1.05	−326.40±4.06	23.92±0.04	23.31±0.08	23.19±0.09	1.46±0.00	1.31±0.00

Bibliography

[1] K. Alberi, J. Wu, W. Walukiewicz, K. M. Yu, O. D. Dubon, S. P. Watkins, C. X. Wang, X. Liu, Y.-J. Cho, and J. Furdyna, "Valence-band anticrossing in mismatched III-V semiconductor alloys," *Phys. Rev. B*, vol. 75, p. 045203, Jan. 2007.

[2] N. Ares, V. N. Golovach, G. Katsaros, M. Stoffel, F. Fournel, L. I. Glazman, O. G. Schmidt, and S. De Franceschi, "Nature of Tunable Hole g Factors in Quantum Dots," *Phys. Rev. Lett.*, vol. 110, p. 046602, Jan. 2013.

[3] M. Atatüre, D. Englund, N. Vamivakas, S.-Y. Lee, and J. Wrachtrup, "Material platforms for spin-based photonic quantum technologies," *Nat Rev Mater*, vol. 3, pp. 38–51, May 2018.

[4] D. D. Awschalom, L. C. Bassett, A. S. Dzurak, E. L. Hu, and J. R. Petta, "Quantum Spintronics: Engineering and Manipulating Atom-Like Spins in Semiconductors," *Science*, vol. 339, pp. 1174–1179, Mar. 2013.

[5] L. C. Bannow, S. C. Badescu, J. Hader, J. V. Moloney, and S. W. Koch, "Valence band splitting in bulk dilute bismides," *Appl. Phys. Lett.*, vol. 111, p. 182103, Oct. 2017.

[6] L. C. Bannow, O. Rubel, S. C. Badescu, P. Rosenow, J. Hader, J. V. Moloney, R. Tonner, and S. W. Koch, "Configuration dependence of band-gap narrowing and localization in dilute $GaAs_{1-x}Bi_x$ alloys," *Phys. Rev. B*, vol. 93, p. 205202, May 2016.

[7] Z. Batool, K. Hild, T. J. C. Hosea, X. Lu, T. Tiedje, and S. J. Sweeney, "The electronic band structure of GaBiAs/GaAs layers: Influence of strain and band anti-crossing," *J. Appl. Phys.*, vol. 111, p. 113108, June 2012.

[8] M. Bayer, P. Hawrylak, K. Hinzer, S. Fafard, M. Korkusinski, Z. R. Wasilewski, O. Stern, and A. Forchel, "Coupling and Entangling of Quantum States in Quantum Dot Molecules," *Science*, vol. 291, pp. 451–453, Jan. 2001.

[9] N. H. Bonadeo, J. Erland, D. Gammon, D. Park, D. S. Katzer, and D. G. Steel, "Coherent Optical Control of the Quantum State of a Single Quantum Dot," *Science*, vol. 282, pp. 1473–1476, Nov. 1998.

[10] A. S. Bracker, M. Scheibner, M. F. Doty, E. A. Stinaff, I. V. Ponomarev, J. C. Kim, L. J. Whitman, T. L. Reinecke, and D. Gammon, "Engineering electron and hole tunneling with asymmetric InAs quantum dot molecules," *Appl. Phys. Lett.*, vol. 89, p. 233110, Dec. 2006.

[11] J. I. Climente, M. Korkusinski, G. Goldoni, and P. Hawrylak, "Theory of valence-band holes as Luttinger spinors in vertically coupled quantum dots," *Phys. Rev. B*, vol. 78, p. 115323, Sept. 2008.

[12] A. Crippa, R. Maurand, L. Bourdet, D. Kotekar-Patil, A. Amisse, X. Jehl, M. Sanquer, R. Laviéville, H. Bohuslavskyi, L. Hutin, S. Barraud, M. Vinet, Y.-M. Niquet, and S. De Franceschi, "Electrical Spin Driving by g-Matrix Modulation in Spin-Orbit Qubits," *Phys. Rev. Lett.*, vol. 120, p. 137702, Mar. 2018.

[13] K. De Greve, P. L. McMahon, D. Press, T. D. Ladd, D. Bisping, C. Schneider, M. Kamp, L. Worschech, S. Höfling, A. Forchel, and Y. Yamamoto, "Ultrafast coherent control and suppressed nuclear feedback of a single quantum dot hole qubit," *Nature Phys*, vol. 7, pp. 872–878, Nov. 2011.

[14] A. Delteil, Z. Sun, W.-b. Gao, E. Togan, S. Faelt, and A. Imamoğlu, "Generation of heralded entanglement between distant hole spins," *Nature Phys*, vol. 12, pp. 218–223, Mar. 2016.

[15] H.-X. Deng, J. Li, S.-S. Li, H. Peng, J.-B. Xia, L.-W. Wang, and S.-H. Wei, "Band crossing in isovalent semiconductor alloys with large size mismatch: First-principles calculations of the electronic structure of Bi and N incorporated GaAs," *Phys. Rev. B*, vol. 82, p. 193204, Nov. 2010.

[16] M. F. Doty, J. I. Climente, A. Greilich, M. Yakes, A. S. Bracker, and D. Gammon, "Hole-spin mixing in InAs quantum dot molecules," *Phys. Rev. B*, vol. 81, p. 035308, Jan. 2010.

[17] M. F. Doty, J. I. Climente, M. Korkusinski, M. Scheibner, A. S. Bracker, P. Hawrylak, and D. Gammon, "Antibonding Ground States in InAs Quantum-Dot Molecules," *Phys. Rev. Lett.*, vol. 102, p. 047401, Jan. 2009.

[18] M. F. Doty, M. Scheibner, A. S. Bracker, I. V. Ponomarev, T. L. Reinecke, and D. Gammon, "Optical spectra of doubly charged quantum dot molecules in electric and magnetic fields," *Phys. Rev. B*, vol. 78, p. 115316, Sept. 2008.

[19] M. F. Doty, M. Scheibner, I. V. Ponomarev, E. A. Stinaff, A. S. Bracker, V. L. Korenev, T. L. Reinecke, and D. Gammon, "Electrically Tunable g Factors in Quantum Dot Molecular Spin States," *Phys. Rev. Lett.*, vol. 97, p. 197202, Nov. 2006.

[20] B. Eble, C. Testelin, P. Desfonds, F. Bernardot, A. Balocchi, T. Amand, A. Miard, A. Lemaître, X. Marie, and M. Chamarro, "Hole–Nuclear Spin Interaction in Quantum Dots," *Phys. Rev. Lett.*, vol. 102, p. 146601, Apr. 2009.

[21] S. E. Economou, J. I. Climente, A. Badolato, A. S. Bracker, D. Gammon, and M. F. Doty, "Scalable qubit architecture based on holes in quantum dot molecules," *Phys. Rev. B*, vol. 86, p. 085319, Aug. 2012.

[22] B. Fluegel, S. Francoeur, A. Mascarenhas, S. Tixier, E. C. Young, and T. Tiedje, "Giant Spin-Orbit Bowing in $GaAs_{1-x}Bi_x$," *Phys. Rev. Lett.*, vol. 97, p. 067205, Aug. 2006.

[23] W. B. Gao, P. Fallahi, E. Togan, A. Delteil, Y. S. Chin, J. Miguel-Sanchez, and A. Imamoğlu, "Quantum teleportation from a propagating photon to a solid-state spin qubit," *Nat Commun*, vol. 4, p. 2744, Nov. 2013.

[24] G. Gillard, I. M. Griffiths, G. Ragunathan, A. Ulhaq, C. McEwan, E. Clarke, and E. A. Chekhovich, "Fundamental limits of electron and nuclear spin qubit lifetimes in an isolated self-assembled quantum dot," *npj Quantum Inf*, vol. 7, pp. 1–8, Feb. 2021.

[25] M. Graf and P. Vogl, "Electromagnetic fields and dielectric response in empirical tight-binding theory," *Phys. Rev. B*, vol. 51, pp. 4940–4949, Feb. 1995.

[26] W. A. Harrison, "Bond-Orbital Model and the Properties of Tetrahedrally Coordinated Solids," *Phys. Rev. B*, vol. 8, pp. 4487–4498, Nov. 1973.

[27] A. Janotti, S.-H. Wei, and S. B. Zhang, "Theoretical study of the effects of isovalent coalloying of Bi and N in GaAs," *Phys. Rev. B*, vol. 65, p. 115203, Feb. 2002.

[28] C. Jennings, X. Ma, T. Wickramasinghe, M. Doty, M. Scheibner, E. Stinaff, and M. Ware, "Self-Assembled InAs/GaAs Coupled Quantum Dots for Photonic Quantum Technologies," *Adv. Quantum Technol.*, vol. 3, no. 2, p. 1900085, 2020.

[29] P. R. C. Kent and A. Zunger, "Theory of electronic structure evolution in GaAsN and GaPN alloys," *Phys. Rev. B*, vol. 64, p. 115208, Aug. 2001.

[30] A. V. Khaetskii, D. Loss, and L. Glazman, "Electron Spin Decoherence in Quantum Dots due to Interaction with Nuclei," *Phys. Rev. Lett.*, vol. 88, p. 186802, Apr. 2002.

[31] A. V. Khaetskii and Y. V. Nazarov, "Spin relaxation in semiconductor quantum dots," *Phys. Rev. B*, vol. 61, pp. 12639–12642, May 2000.

[32] C. Kloeffel, M. Trif, and D. Loss, "Strong spin-orbit interaction and helical hole states in Ge/Si nanowires," *Phys. Rev. B*, vol. 84, p. 195314, Nov. 2011.

[33] H. J. Krenner, M. Sabathil, E. C. Clark, A. Kress, D. Schuh, M. Bichler, G. Abstreiter, and J. J. Finley, "Direct Observation of Controlled Coupling in an Individual Quantum Dot Molecule," *Phys. Rev. Lett.*, vol. 94, p. 057402, Feb. 2005.

[34] T. D. Ladd, F. Jelezko, R. Laflamme, Y. Nakamura, C. Monroe, and J. L. O'Brien, "Quantum computers," *Nature*, vol. 464, p. 45, Mar. 2010.

[35] P. Laukkanen, M. P. J. Punkkinen, A. Lahti, J. Puustinen, M. Tuominen, J. Hilska, J. Mäkelä, J. Dahl, M. Yasir, M. Kuzmin, J. R. Osiecki, K. Schulte, M. Guina, and K. Kokko, "Local variation in Bi crystal sites of epitaxial GaAsBi studied by photoelectron spectroscopy and first-principles calculations," *Applied Surface Science*, vol. 396, pp. 688–694, Feb. 2017.

[36] A. Lin, M. F. Doty, and G. W. Bryant, "Incorporation of Random Alloy $GaBi_xAs_{1-x}$ Barriers in InAs Quantum Dot Molecules: Energy Levels and Confined Hole States," *Phys. Rev. B*, vol. 99, p. 075308, Feb. 2019.

[37] A. Lindsay and E. P. O'Reilly, "Theory of enhanced bandgap non-parabolicity in GaN_xAs_{1-x} and related alloys," *Solid State Communications*, vol. 112, pp. 443–447, Oct. 1999.

[38] W. Liu, S. Sanwlani, R. Hazbun, J. Kolodzey, A. S. Bracker, D. Gammon, and M. F. Doty, "In situ tunable g factor for a single electron confined inside an InAs quantum dot molecule," *Phys. Rev. B*, vol. 84, p. 121304(R), Sept. 2011.

[39] X. Ma, G. W. Bryant, and M. F. Doty, "Hole spins in an InAs/GaAs quantum dot molecule subject to lateral electric fields," *Phys. Rev. B*, vol. 93, p. 245402, June 2016.

[40] I. A. Merkulov, Al. L. Efros, and M. Rosen, "Electron spin relaxation by nuclei in semiconductor quantum dots," *Phys. Rev. B*, vol. 65, p. 205309, Apr. 2002.

[41] J. J. L. Morton, D. R. McCamey, M. A. Eriksson, and S. A. Lyon, "Embracing the quantum limit in silicon computing," *Nature*, vol. 479, p. 345, Nov. 2011.

[42] G. Ortner, M. Bayer, Y. Lyanda-Geller, T. L. Reinecke, A. Kress, J. P. Reithmaier, and A. Forchel, "Control of Vertically Coupled InGaAs/GaAs Quantum Dots with Electric Fields," *Phys. Rev. Lett.*, vol. 94, p. 157401, Apr. 2005.

[43] S. T. Pantelides and W. A. Harrison, "Structure of the valence bands of zinc-blende-type semiconductors," *Phys. Rev. B*, vol. 11, pp. 3006–3021, Apr. 1975.

[44] J. Planelles, F. Rajadell, and J. I. Climente, "Symmetry-induced hole-spin mixing in quantum dot molecules," *Phys. Rev. B*, vol. 92, p. 041302(R), July 2015.

[45] C. Pryor, J. Kim, L. W. Wang, A. J. Williamson, and A. Zunger, "Comparison of two methods for describing the strain profiles in quantum dots," *J. Appl. Phys.*, vol. 83, p. 2548, June 1998.

[46] F. Rajadell, J. I. Climente, and J. Planelles, "Large hole spin anticrossings in InAs/GaAs double quantum dots," *Appl. Phys. Lett.*, vol. 103, p. 132105, Sept. 2013.

[47] M. Scheibner, A. S. Bracker, D. Kim, and D. Gammon, "Essential concepts in the optical properties of quantum dot molecules," *Solid State Communications*, vol. 149, pp. 1427–1435, Sept. 2009.

[48] N. Somaschi, V. Giesz, L. De Santis, J. C. Loredo, M. P. Almeida, G. Hornecker, S. L. Portalupi, T. Grange, C. Antón, J. Demory, C. Gómez, I. Sagnes, N. D. Lanzillotti-Kimura, A. Lemaítre, A. Auffeves, A. G. White, L. Lanco, and P. Senellart, "Near-optimal single-photon sources in the solid state," *Nature Photon*, vol. 10, pp. 340–345, May 2016.

[49] E. A. Stinaff, M. Scheibner, A. S. Bracker, I. V. Ponomarev, V. L. Korenev, M. E. Ware, M. F. Doty, T. L. Reinecke, and D. Gammon, "Optical Signatures of Coupled Quantum Dots," *Science*, vol. 311, pp. 636–639, Feb. 2006.

[50] R. Stockill, C. Le Gall, C. Matthiesen, L. Huthmacher, E. Clarke, M. Hugues, and M. Atatüre, "Quantum dot spin coherence governed by a strained nuclear environment," *Nat Commun*, vol. 7, p. 12745, Sept. 2016.

[51] R. Stockill, M. J. Stanley, L. Huthmacher, E. Clarke, M. Hugues, A. J. Miller, C. Matthiesen, C. Le Gall, and M. Atatüre, "Phase-Tuned Entangled State Generation between Distant Spin Qubits," *Phys. Rev. Lett.*, vol. 119, p. 010503, July 2017.

[52] C. Testelin, F. Bernardot, B. Eble, and M. Chamarro, "Hole-spin dephasing time associated with hyperfine interaction in quantum dots," *Phys. Rev. B*, vol. 79, p. 195440, May 2009.

[53] M. Usman, C. A. Broderick, Z. Batool, K. Hild, T. J. C. Hosea, S. J. Sweeney, and E. P. O'Reilly, "Impact of alloy disorder on the band structure of compressively strained $GaBi_xAs_{1-x}$," *Phys. Rev. B*, vol. 87, p. 115104, Mar. 2013.

[54] M. Usman, C. A. Broderick, A. Lindsay, and E. P. O'Reilly, "Tight-binding analysis of the electronic structure of dilute bismide alloys of GaP and GaAs," *Phys. Rev. B*, vol. 84, p. 245202, Dec. 2011.

[55] A. Vezvaee, E. Takou, P. Hilaire, M. F. Doty, and S. E. Economou, "Avoiding leakage and errors caused by unwanted transitions in Lambda systems," *PRX Quantum*, vol. 4, p. 030312, July 2023.

[56] P. Vogl, H. P. Hjalmarson, and J. D. Dow, "A Semi-empirical tight-binding theory of the electronic structure of semiconductors†," *Journal of Physics and Chemistry of Solids*, vol. 44, pp. 365–378, Jan. 1983.

[57] Z. R. Wasilewski, S. Fafard, and J. P. McCaffrey, "Size and shape engineering of vertically stacked self-assembled quantum dots," *Journal of Crystal Growth*, vol. 201–202, pp. 1131–1135, May 1999.

[58] H. Watzinger, J. Kukučka, L. Vukušić, F. Gao, T. Wang, F. Schäffler, J.-J. Zhang, and G. Katsaros, "A germanium hole spin qubit," *Nat Commun*, vol. 9, p. 3902, Sept. 2018.

[59] J. Yoshida, T. Kita, O. Wada, and K. Oe, "Temperature Dependence of $GaAs_{1-x}Bi_x$ Band Gap Studied by Photoreflectance Spectroscopy," *Jpn. J. Appl. Phys.*, vol. 42, p. 371, Feb. 2003.

[60] Y. Zhang, A. Mascarenhas, and L.-W. Wang, "Similar and dissimilar aspects of III-V semiconductors containing Bi versus N," *Phys. Rev. B*, vol. 71, p. 155201, Apr. 2005.